In silico analysis of the influence of root hydraulic anatomy on maize (*Zea mays*) water uptake



New tools and models

Adrien Heymans

January 2022

Thesis presented for the fulfilling of my PhD degree in Agronomical Sciences and Biological Engineering

Earth and Life Institute
Université catholique de Louvain

Thesis examining board

Supervisor:	Prof. Guillaume Lobet
President of the jury:	Prof. Pierre Bertin
Members of the jury:	Prof. Valentin Couvreur
	Prof. Xavier Draye
	Prof. Mathieu Javaux
	Prof. Andrew McElrone
	Prof. Ruairidh Sawers
	Prof. Andrea Schnepf

Credits

The first two years of this thesis were funded by *Fonds de Recherche Spécial* from the Université Catholique de Louvain. The second two years were funded by the *Incentive Grant for Scientific Research* from the Fonds National de la Recherche Scientifique. Adrien Heymans is grateful to those organizations for their confidence and financial support.

The computational resources have been provided by the *Consortium des Équipements de Calcul Intensif* (CÉCI), funded by the *Fonds de la Recherche Scientifique* de Belgique (F.R.S.-FNRS) under Grant No. 2.5020.11 and by the Walloon Region.

ACKNOWLEDGEMENTS

Un tout tout grand Merci à toi, Guillaume, qui lors notre première réunion avait proposé qu'on marche ensemble pour discuter plutôt que de rester assis. On en aura fait du chemin depuis ! J'apprécie particulièrement ta sincérité, tes conseils et ton imagination qui ont guidé mes pas dans le monde de la recherche. A peine arrivé au labo, tu me confies un code produisant de beaux motifs géométriques. La consigne était simple : "ce serait bien si on pouvait en faire quelque chose de sympa". Et me voila a faire du dessin sur ordinateur et à créer des racines au bon vouloir de cette imagination. Merci d'avoir été là pour cadrer une certaine partie de mes idées, bien que souvent c'était pour agrandir le canva. Merci d'être si amical, c'est très enrichissant de pouvoir partager sans peur ses idées, ses résultats et ses déconvenues. J'en aurais énormément appris et grandi grâce à toi, merci.

A Xavier, l'éternelle semeur de passion, merci ! Sur les bancs on entendait ton amour pour le mystère de la science, le plaisir de comprendre le monde qui nous entoure, de se poser des questions à tout bout de champ. Tu restera toujours pour moi, la personne qui prononce une simple phrase, et que même si on la comprend sur le moment même, ce n'est que bien plus tard qu'elle fait vraiment écho. Mathieux, ta vitesse de réflexion m'impressionne toujours. C'est toujours une opportunité en or que de pouvoir débattre et de confronter ses idées avec quelqu'un de si perspicace et ancré dans le réel.

The first model that I had the pleasure to work with during the thesis was CRootBox. Then later on, I had the pleasure to meet Andrea and the large community of researcher which improved the model in a way that sat the model CPlantBox as one of the key foundations of my thesis.

Andrew and Italo, thank you for the nice exchanges on grapevine roots. I had an amazing blast at twisting the GRANAR code to make it look like grapevine roots, and including these little intercellular spaces. I really wish I could have been visiting you. This is also true for you, Ruairidh and Chloee. Our numerous meetings online were very inspiring and fruitful. From each of them I was unable to sit due to the over-existing information that was shared.

Valentin, c'est incroyable de travailler avec toi, et ce à tous les points de vue. Dès les premiers jours, tu as fait naître tellement de projets. Notamment à l'ACELI avec le compost, mais ton savoir sur les plus infimes détails du prélèvement de l'eau m'a permis d'aller si loin! Chaque fois que j'avais une question technique, besoin d'une référence, ou de résoudre des équations de flux, Valentin "Sauveur" était là ! Mille fois merci.

Quand je pense à qu'est-ce qu'un collègue en or, je pense à vous chers collègues de ECAV/PEPA. Les soirées jeux, les petits verres, le Kombucha, ainsi que toutes les tartes qu'on a vu passé qui ont bien agrémenté ces quatre années. Clément, le bureau est étrangement vide sans toi. C'était génial que de partager autant d'abréviations en commun et de rêver modéliser des comportements complexes de système racinaire. A toutes la Bananeraie, merci de m'avoir laisser faire mes siestes sans faire trop de bruit. C'était génial de partager ces années avec vous, du premier code R, au aléa du Bac aero. Thomas, merci énormement pour tout les coups de main, les bon moments pendant les récoltes, ou encore lors de notre séjour à Dijon.

Aux Amis, merci d'avoir eu la patience d'écouter mes histoires de racine, d'avoir même relu certaines parties du manuscrit, ou d'avoir accompagné mes expériences dans les serres quand j'avais besoin d'un coup de main le weekend. Merci Volo pour m'avoir guidé sur les Cluster de l'UCLouvain quand j'étais perdu sur linux. Merci Benja, sans qui la St-Furcy ne serait qu'une eau de source. Merci Greg, Thomas et Yat dont les yeux s'iluminent à la moindre notion de jeux de société.

Mille merci à mes racines, ma famille, qui m'ont donné goût et nourri mon envie d'en savoir plus, d'avoir permis à mes rêves de grandir et de devenir qui je suis. Papy et papa votre enthousiasme vis à vis de la science et de tout ce qui émerveille ont profondément fait écho chez moi. Bonne-mamy et maman, vos jardins et potagers sont des terreaux incroyables pour faire grandir de bonne mains "vertes". Mamy, si y a autant d'équation et de trigonométrie dans cette thèse, c'est en partie de toi que je le dois. A mes soeurs, beau-frère, et belle-famille, merci d'embellir ma vie.

Mes remerciements les plus chaleureux vont pour toi, Amélie. Merci de marcher ensemble le long de cette grande aventure qu'est la vie, de rendre ce voyage si agréable, d'en épicer chaque moment, et d'être si incroyablement toi. Cette thèse, je la dois en grande partie à toi. Tu as eu la clairvoyance de me donner le petit coup de pouce pour que j'aille frapper à la porte de chez Guillaume et saisir ma

chance de faire une thèse. Merci d'avoir créé tant de moment propice à l'épanouissement de nos projets en tout genre et d'y mettre le grain de poivre. Et a toi, qui arrive bientot, je te réserve déjà une grande place dans mon coeur.

A vous tous, merci !

Adrien
Louvain-la-Neuve
18 Janvier 2022.

SHORT CONTENTS

Introduction and objectives **1**

Root anatomy and function **35**

Water Flow in root systems **113**

Discussion and Conclusion **177**

TABLE OF CONTENTS

Introduction and objectives

Introduction **5**

Objectives **9**

Specific objectives 9

Limitations 15

1 Context **17**

1.1 Water flow in the soil-plant-air continuum 17
1.1.1 Water limitation 18
1.1.2 Root system hydraulic architecture 19
1.1.3 Xylem embolism and stomata regulation 20

1.2 Complex root system hydraulics architecture . . . 21
1.2.1 Macroscopic root water uptake models 22
1.2.2 Macro-hydraulic properties 22
1.2.3 Micro-hydraulic properties 24
1.2.4 Subcellular hydraulic properties 26
1.2.5 Offset between k_r and K_x along the root 28

1.3 Non-unique site-specific eco-ideotypes 28
1.3.1 Virtual phenotyping 31

1.4 Conclusive remarks on the thematic background . . 31
1.4.1 *Zea mays* 32

Root anatomy and function

2 Maize root anatomy **39**

2.1 Introduction 40

2.2 Material and methods 41
2.2.1 Description of the GRANAR model 41
2.2.2 Description of the GRANAR package 43
2.2.3 Description of the MECHA-GRANAR connection 44
2.2.4 Description of the experimental data 44
2.2.5 Methods to get the parameters 45
2.2.6 Description of MECHA hydraulic parameters . . 46
2.2.7 Statistical analysis 47

2.3 Results 48
2.3.1 Overview of GRANAR 48
2.3.2 Generation of diverse anatomies 50
2.3.3 GRANAR-MECHA estimation of k_r 51
2.3.4 Anatomical trait influence on k_r 53

2.4 Discussion 59

2.5 Conclusion 64

3 Hydraulic atlases of maize roots 67

3.1 Introduction 68

3.2 Material and methods 70
3.2.1 Plant materials and growth condition 70
3.2.2 Processing root cross-sections 71
3.2.3 Root typology 71
3.2.4 Root image analysis 71
3.2.5 Description of MECHA hydraulic parameters . . 74
3.2.6 Root hydraulic conductivities benchmark 75
3.2.7 Statistical analysis 76

3.3 Results 76
3.3.1 Changes in anatomical traits 76
3.3.2 Atlas of anatomies and maturation stages . . . 79
3.3.3 Building an atlas of root hydraulic conductivities 81

3.4 Discussion 81

3.5 Conclusion 87

3.6 Appendix 88

4 Root hydraulic anatomy **91**

4.1 Introduction 92

4.2 Material and methods 95
4.2.1 Meta-analysis on root traits diversity 96
4.2.2 Ranges of root traits variation 96
4.2.3 Estimation of the k_r 98
4.2.4 Training the meta-models 98
4.2.5 Global sensitivity analysis 99
4.2.6 Statistical analysis 100

4.3 Results 100
4.3.1 Meta-analysis of root anatomical data-sets . . . 100
4.3.2 Machine learning to obtain k_r 102
4.3.3 Hydraulic anatomy influence 102

4.4 Discussion 105

4.5 Conclusion 108

4.6 Appendix 109

WATER FLOW IN ROOT SYSTEMS

5 Root water uptake dynamics *in silico* **117**

5.1 Introduction 118

5.2 Material and methods 120
5.2.1 Simulation design 120
5.2.2 Root system hydraulic architecture 122
5.2.3 Environmental feedback 124
5.2.4 Statistical analysis 127

5.3 Results 128
5.3.1 Influence of the hydraulic anatomy 130
5.3.2 Soil feedback on water uptake 132
5.3.3 Root water uptake efficiency 134

5.4 Discussion 137

5.4.1 Root anatomy influences on RWU 138
5.4.2 Hydraulic properties influence on RWU 139
5.4.3 Timing effect 140
5.4.4 Drainage and water storage capacity 141
5.4.5 Engineering root traits 141

5.5 Conclusion 142

5.6 Appendix 144
5.6.1 Root water uptake rate 144
5.6.2 Shoot water demand 145
5.6.3 Soil hydraulic properties in root vicinity 146

6 Root water uptake of *in silico* landraces 151

6.1 Introduction 152

6.2 Materials and methods 154
6.2.1 Plant materials 154
6.2.2 Virtual pedo-climatic environments 156
6.2.3 Experimental design 158
6.2.4 Statistical analysis 158

6.3 Results 158
6.3.1 Soil feedback 160
6.3.2 Root water uptake efficiency 162
6.3.3 Potential RWU efficiency 165
6.3.4 Hydraulic properties 166

6.4 Discussion 168
6.4.1 Growth rates advantages 169
6.4.2 Transpiration vs. Carbon cost 169
6.4.3 Water uptake efficiency 171
6.4.4 Transpiration vs. water depletion 171
6.4.5 Anatomical traits influence 172

6.5 Conclusion 173

6.6 Appendix 174

Discussion and Conclusion

7 Discussion and outlooks **181**

7.1 The root hydraulic anatomy 181
7.1.1 Biological insights 181
7.1.2 Technological improvements 182
7.1.3 Perspectives 182

7.2 The root hydraulic atlases 186
7.2.1 Biological insights 186
7.2.2 Technological improvements 186
7.2.3 Perspective 186

7.3 *In silico* maize root water uptake dynamics 188
7.3.1 Biological insights 188
7.3.2 Technological improvements 189
7.3.3 Perspectives 189

7.4 Structural limitation 191
7.4.1 On model uncertainties 191
7.4.2 On computing time 192

8 Conclusions **193**

General bibliography **195**

LIST OF FIGURES

0.1 General objectives 10

1.1 Water flow in plants. 19
1.2 Offset between k_r and K_x along the root 29
1.3 Apoplastic barriers along roots 29
1.4 Representation of maize root system architecture . . 33
1.5 Maize root anatomy 34

2.1 Methodology to generate the vascular elements . . . 43
2.2 Hydrophobic barriers and k_r along maize roots . . . 47
2.3 GRANAR vs. cross-section images 49
2.4 GRANAR vs. CellSeT based methods 50
2.5 *in silico* vs. experimental anatomies 52
2.6 Visualization k_r vs. anatomical traits 54
2.7 Comparison between k_r values. 55
2.8 Aerenchyma proportion influence on k_r. 57
2.9 Cortex influence on k_r. 58
2.10 Stele influence on k_r. 59
2.11 Xylem influence on k_r. 60

3.1 Anatomical traits along the root axis 78
3.2 Meta-xylem area vs. stele area 79
3.3 Representation of maize root anatomy 80
3.4 Basal root cross-section images along the axis. . . . 82
3.5 Root maturation stages 83
3.6 Hydraulic conductivity atlas 84
3.7 Visual protocol for anatomical traits 88

4.1 Allometry between root anatomical traits 101
4.2 Variance decomposition 104
4.3 Partitioning between apo- & symplastic fluxes 107
4.4 Variance decomposition: Kr 110
4.5 Morris screening 111
4.6 Allometry across anatomical traits 112

5.1 Hydraulic Viper 123

5.2 Age dependent hydraulic functions 125
5.3 Root system architecture of B73 129
5.4 Root water uptake rate 129
5.5 Main effects on cumulative water uptake 131
5.6 Soil water map 133
5.7 retention curve 133
5.8 K_{srs} / K_{rs} 134
5.9 Water uptake of the "adapted" 137
5.10 Standard uptake density 140
5.11 Hydraulic anatomy influence on the water uptake rate 144
5.12 Weather in Palermo 145

6.1 Origins of the MAGIC landraces 155
6.2 Root cross-sections of landraces 156
6.3 RSA of the MAGIC landraces 159
6.4 Transpiration rates of landraces 161
6.5 Soil water profiles 162
6.6 K_{srs} / K_{rs} 163
6.7 Dynamic water uptake efficiency 165
6.8 Water uptake performance and efficiency 166
6.9 Potential efficiency 168
6.10 Soil PCA 175

7.1 Grapevine root anatomy 184
7.2 Water fluxes in vine roots 184
7.3 Suberin deposition influence on the kr reduction . . 187

LIST OF TABLES

2.1 List of parameters for GRANAR 42
2.2 Methods from RootScan to GRANAR parameters . 45
2.3 ANOVA results for the anatomical effect on k_r . . . 53
2.4 One-by-one anatomical trait effect on k_r 55

3.1 List of the acquired anatomical traits 72
3.2 Anatomical traits vs. apex distance and root typology 77

4.1 Range of variation for the input values 97
4.2 Allometry between anatomical traits 102
4.3 Machine learning models fitness 103

5.1 Variables for k_r and K_x 121
5.2 Adapted root traits for efficient RWU 136
5.3 Performance score of "adapted" phenotypes 136

6.1 Soil hydraulic 157
6.2 ANOVA results complete models 167
6.3 Range for hydraulic parameters 176

PART I

INTRODUCTION & OBJECTIVES

In this first part, we shortly introduce the theme, the objectives and the context of the thesis. The different objectives are formulated through research questions and methodological goals. As a follow-up, the different limitations and boundary conditions of the objectives are summarized. The last section in this first part offers the background concepts related to most of the raised topics in this thesis.



La Trahison des images (English : The Treachery of Images) —

Magritte

The map is not the territory, the word is not the thing it describes. Whenever the map is confused with the territory, a 'semantic disturbance' is set up in the organism. The disturbance continues until the limitation of the map is recognized.

Alfred Korzybski

INTRODUCTION

Root systems achieve important functions for the plant. One of these key functions is the absorption of water from their surroundings. This passive process is driven by the diffusion of vapor at the stomata openings and the cohesion-tension principle (Steudle, 2001). The loss of water at the stomata increases the tension over the water column which propagates through the plant and reaches the rhizosphere. The resulting transpiration allows the diffusion of carbon dioxide into the leaves and the synthesis of new carbohydrates by the plants.

In many locations, plants are frequently exposed to water limitation due to insufficient rainfall and available soil water, which then restricts crop yield. In the context of climate changes, drought episodes will have an increasing variability from year to year (Harrison et al., 2014). There will also be an increasing likelihood of experiencing water deficit at key phenological stages. In regions with low rainfall, water limitation is often described as the most limiting abiotic factor for crop production (Sinclair, 1994), and even more so when it impacts the development of yield establishing stages (Fuad-Hassan et al., 2008).

For any specific pedo-climatic conditions, the efficiency of a plant to grow and produce depends on a set of traits that are adapted to the facing environmental conditions (Tardieu et al., 2018). Within plant diversity, some phenotypic traits have already shown their usefulness when it comes to being efficient even under water limiting conditions or drought stress. For example, plant transpiration regulation mechanisms, leaf growth, rooting depth or temporal adaptation are traits that are selected by breeders when plant resistance to drought is willingly aimed.

However, large root traits selection has been avoiding the spotlight, even if they fulfil the major water uptake function. The major difficulties being the soil, which prevent the direct experimental observation and access to the roots. Although new methods (e.g. shovelomics) start to scratch the surface of this underground world, it gathers few yet important structural traits at the top of the root system (Trachsel et al., 2011). As traditional ways get bogged down to measure

root traits in large scale and at lower scale, modeling tools might help us understand the intricacy of the root water uptake function and provide insight for root traits base selection (Passot et al., 2019; Rellán-Álvarez et al., 2016).

The co-localization of roots and soil water is typically considered as determinants for water uptake (de Dorlodot et al., 2007; Manschadi et al., 2006). Nonetheless, root system architecture by itself does not simply define the water uptake pattern. Root systems form networks that have a typically low hydraulic conductance (Kramer, 1938; Steudle, 2000). And their hydraulics is crucial, because it determines the intrinsic capacity of the root to absorb and transport water. The full comprehension of the root ability to uptake water requires the fine knowledge of the root architecture and its hydraulics as a whole. Recent works aimed at better understanding the role of anatomy (Chimungu et al., 2014b; Rieger, and Litvin, 1999), cell hydraulic properties (Couvreur et al., 2018; Javot, and Maurel, 2002), or soil hydraulic properties (Carminati, and Javaux, 2020) over the root water uptake. Yet, there is still a lot to discover about the combined effect of root anatomy with the cellular hydraulic properties on the root system hydraulic conductance. Although, the development of new computational models at the cellular, and at the plant scale provide new investigation tools to unravel water flows in this below ground world. A full behavioral study linking the anatomy with the cell scaled hydraulic properties on an evolving root system has great research potential.

Note about the thesis structure

This thesis is a compilation of published and unpublished work. To improve the coherence of this manuscript, the different sections are modified versions of their original part. Some repetitions might still occur from one chapter to the other, I hope that it will not disturb too much the reading of the whole document.

Maize: a model plant

The selection of the maize plant (*Zea mays*) as the model plant to conduct this thesis was based on the following criteria:

- Maize has an important share on global crop production (*OECD-FAO Agricultural Outlook* 2022).
- Maize plants have been extensively studied and the scientific literature covers almost every aspect of the maize physiology, morphology, genetics, etc.
- Maize is severely sensitive to drought events during the flowering time (Fuad-Hassan et al., 2008; Herrero, and Johnson, 1981).
- Maize roots are thicker than those of most cereal crops which makes them easy to observe and quantify.
- Several research groups in the direct lab neighborhood were already working on maize when the project started.
- Maize plants quickly develop a large leaf area and display, therefore, an important transpiration.

OBJECTIVES

General objectives

Being able to estimate the impact of specific traits and their interaction on the plant absorption dynamics could provide good insights for future plant choice in a changing climatic world. In this brief context, the main question that has driven this thesis is:

> *Which sets of root hydraulic traits could theoretically increase the root water uptake of maize (Zea mays) in specific environments?*

Thus, phrased differently, the objective of the thesis is to **estimate the hydraulic behavior of different maize (*Zea mays*) plants in virtual environments, going from the organ scale to the plant scale, using modeling tools**. This would lead the way to explore the root traits diversity in specific pedo-climatic conditions.

In order to achieve this objective, new tools and models were required to (**I**) quantify the contribution of the different root anatomical traits on the root hydraulic conductivity, (**II**) estimate the hydraulic conductivities of different root types and map the hydraulic on root systems, and then (**III**) quantify the contribution of the different root anatomical and hydraulic traits on the evolution of the water uptake rate over a period of time depending on specified pedo-climatic condition.

The articulation between those different requirements is schematically represented in Figure 0.1 to respond to the main objective.

Specific objectives

Root anatomy and radial hydraulic conductivity

Root hydraulic conductivity is a limiting factor along the water pathways between the soil and the leaf. It is defined by subcellular hydraulic properties and anatomical traits. However, little is known about the effect of the different anatomical traits and subcellular hydraulic properties on the radial hydraulic conductivity. The main

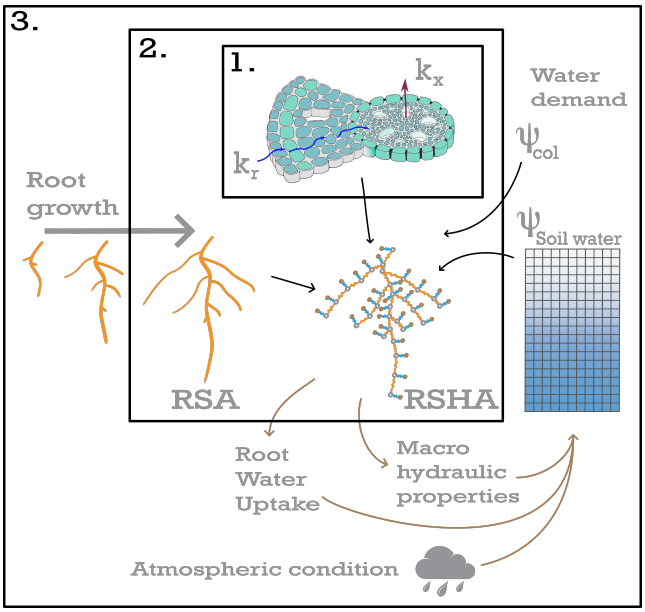


Figure 0.1: The different viewpoints over the general objective and their entanglement in their general context. (1.) The anatomy with the root hydraulic conductivities; (2.) The root system hydraulic architecture with the inclusion of 1; and (3.) The evolution of a root system hydraulic architecture in a specified pedo-climatic environment.

reason is that quantifying the root radial hydraulic conductivity remains challenging. It is experimentally time consuming to measure and not always possible depending on the experimental setup.

Related research objectives

At the organ scale, the first specific objective is therefore to better understand the functional importance and diversity of root hydraulic anatomies[1] in maize plants (*Zea mays*).

[1]**Hydraulic anatomy**: At the root cross-section scale, the hydraulic anatomy corresponds to the combination of the subcellular hydraulic properties and the cells structural network and geometry.

Related methodological objectives

Due to the restrictive ways to measure root radial hydraulic conductivity experimentally, modeling tools can help us get a glimpse of the effect of different root traits over the root hydraulic conductivity. The Model of Explicit Cross-section Hydraulic Anatomy (MECHA) (Couvreur et al., 2018) allows the estimation of the radial hydraulic conductivity of any root root cross section if the cellular network of this root is available. However, there are no computational models that allow to generate such root cross section networks. The first requirement of the thesis was to build a structural model of root anatomy to generate root cross-sections in order to estimate their radial hydraulic conductivity with the model MECHA. This structural model will be able to generate rapidly root cross-section networks that enable us to change their anatomical traits at will. In addition, the input parameter will be easy to extract from root cross section images or pre-existing root anatomical data sets.

Secondly, from a representation of an average root cross section, changing one root anatomical trait at the time will increase our understanding about the effect of each anatomical trait individually over the radial hydraulic conductivity.

In addition, machine learning algorithms are often an opportunity when simulated data can be used to train and validate them (Lobet et al., 2017). Considering we simulate enough root cross sections and have enough estimations of their radial hydraulic conductivity within a known range of variation, it will then be possible to speed up even more the process of evaluating the root radial hydraulic conductivity. This will require a fine knowledge about the impact of each anatomical trait and subcellular hydraulic properties.

Chapter 2 | Chapter 4

Mapping the root hydraulic properties on a root system

Root system hydraulic architecture can be described as the combination of the root system structural architecture, as well as their related age dependent root hydraulic properties. Even though new and old techniques exist to characterize root hydraulic properties, they are very complicated to apply at the required scale. Therefore, analyzing the hydraulic architecture of a single plant relies on heavy technical

procedures. As a result, the effect of anatomical traits and the development time of hydrophobic barriers on the whole root system hydraulic architecture are often overlooked in root water uptake studies.

Related research objectives

At the root system scale, the second specific objective is to better understand the impact of the root anatomical traits, as well as the development of hydrophobic structure on the overall root system hydraulic architecture.

Related methodological objectives

There is a need for a new method which captures the changes of anatomical traits and hydrophobic structure between root types of a root system. Root cross-section images are relatively cheap in terms of time and expertise to obtain. Those images can provide anatomical traits data and developmental information about hydrophobic barriers and meta-xylem maturation to further study their impact on the overall root system conductance. By combining anatomical data and computational models, root cross-section images can be turned into detailed maps of root systems hydraulic properties.

CHAPTER 3

Root system and water uptake dynamics

When assessing the performance of a root system[2] in a pedo-climatic environment, the root system hydraulic properties are needed as they are particularly good indicators of the root water uptake efficiency[3]. Across the growing season, they will help define the ideal root water uptake strategies adapted to the local environment. However, if we want to understand the evolution of the impact of local root traits[4] over the plant performance dynamics, their quantification is often the main constraint. The global root system hydraulic behavior is directly

[2]**Root water uptake performance** is related to the total water taken up by the root system in comparison to the other root system in the same environment and at the same timing.

[3]**Root water uptake efficiency** is defined, in this thesis, as the cumulative root water uptake [cm^3] per unit of root volume [cm^3].

[4]**Local root traits** are the quantification of elements at the root cross-section scale or below (ex: the meta-xylem area [mm^2], the root cell membrane permeability due to aquaporins [$cm\,hPa^{-1}\,d^{-1}$], the average double cell wall thickness [μm], ...).

dependent on the overall root system architecture and the corresponding local hydraulic properties. While local hydraulic properties depend on the root anatomy and subcellular hydraulic properties, all these aspects are interconnected with the soil water availability and the root system architecture. All these interactions across the growing season will affect the plant water absorption dynamics.

Related research objectives

The third specific objective, sum up the different viewpoints previously addressed. On a multi-scale level, this objective aims at better understanding the role of anatomical traits, subcellular hydraulic properties, and the development rate of hydrophobic barriers and meta-xylem vessels over the global root system hydraulic behavior.

Seeking out which root traits and within which range could make a phenotype[5] capable of high cumulative water uptake. A related question is to quantify the cumulative root water uptake per unit of root system volume. This will scale the quantity of water taken up by the plant with a proxy of the amount of carbon invested in the root system.

An additional question will be to further investigate if maize landraces are locally adapted to their regional pedo-climatic environment. If so, does root system architecture and root anatomy explain the regional fitness of landraces in their native location?

Related methodological objectives

In order to simulate a growing root system with a set of specific local root traits in specific pedo-climatic conditions, we needed to build a modeling pipeline for this purpose. This pipeline will require the combination of computational models that are able to simulate the different parts of our system. This series of models will then allow us to observe the global root water uptake dynamics related to specific root trait combinations in any given soil with specific environmental conditions.

First, we focused the analysis on the local root traits, a selection was made on one environment, one root system architecture and three soil types. The selection of a high evaporative demand environment ensures that the root system will be the limiting factor, increasing

[5]**Phenotype** represents the state of the expressed traits of a genotype in a given environment.

the chance of revealing certain root traits with high impact on the root water uptake dynamics. The choice to work with three soil types might expose differences between sets of root traits that maximize the cumulative root water uptake. The underlying hypothesis is that high cumulative transpiration is in general positively with a high biomass production. To ensure that we highlighted the root anatomical trait combinations, we worked with only one root system architecture to reduce the architecture effect (which was not directly investigated here).

Once the modeling pipeline was built, a global sensitivity analysis will be performed to test the percentage of the variance explained by each local trait and the total effect with all interaction processes involved. With enough samples, an uncertainty analysis will also highlight a certain range for different root traits. This will result in high probability of narrowing phenotyping states which perform well and are efficient to take up water for the different soil types.

Secondly, we will study the performance of *in silico* landraces in their environments of origins. For that, we will need to be able to adjust the modeling pipeline and make sure that it works with various root system architectures and increase the range of possible soil hydraulic properties to match the one of the environments of origins.

Chapter 5 | Chapter 6

Limitations

To address the objectives of this thesis and develop the different tools required to answer our research questions, simplifying assumptions were needed. The most critical biological processes that were not included in the thesis are listed below, so the readers can have an unbiased interpretation of our results. These limitations will be discussed across the manuscript and more specifically in the Discussion Chapter 7.

On root representation

To study the root water uptake function at the root organ scale, the scope of the analysis was narrowed down to the root cross-section level. This choice comes from the fact that water fluxes through the roots are divided into two components when simulating root water uptake. There is the radial flux of water from the soil towards the vascular system, and secondly, the axial water transport, which is assumed to take place only within the xylem vessels.

The used models of water flow across root tissues (MECHA) assumes uniform cell properties per cell layer and possible variation of osmotic potential between cells. The current version of the model is dimensionally reduced with no temporal feedback on the cell activity nor true 3D representation of the root organs. Furthermore, the soil water is uniformly distributed around the root cross section and considered as free water directly available to the plant.

On the plant representation

In this study, plant phenotypes are assumed to depend on their hydraulic architecture which changes over time. They are also considered to have constant phenes states. This means that root traits are unchanged during the whole duration of the simulation. Therefore, plant plastic structural responses to environmental stimuli are not encompassed within the framework of the thesis.

Roots are considered as semipermeable membranes, as only certain molecules can pass through (here, only water). This captures the process of transverse water flow in the absence of osmotic potential. Processes such as the solute "diffusion-convection" are too complex at larger scales and may generate a non-linear response of water across the different compartments involved (Couvreur et al., 2018) and are not considered here.

The shoot part organs of the plant are simplified to the most functional point of view with almost no structural aspects. The "big-leaf" approach has the consequence that all plants share the same canopy properties, which include the stomatal density, the leaf area, and the stomatal closure regulation. Drought is also assumed to be non-lethal for the plants. Finally, plants did not have any hydraulic capacitance.

On the environment

In this thesis, the soil was approximated as a homogeneous media following the single porosity model of van Genuchten-Mualem (Šimůnek et al., 2008; Van Genuchten, 1980). The main axis on which water flow was estimated was the depth axis. This 1-D approach was balanced by the inclusion of a simplified soil zone within root influence into our model pipeline. This was part of a trade-off between computational speed and accuracy. However, all inflow and outflow of water happened vertically with no horizontal dispersal due to canopy coverage.

On the plant-environment interaction

Although, there was no feedback between the soil water availability and the root development, nor the root subcellular hydraulic properties, the hydraulic conductivity of the soil zone within roots influence was partly function of the root length density and the soil hydraulic properties.

Another biological process which was not included in this thesis is the mucilage secretion by plants in the rhizosphere. It is known that it changes the hydraulic properties in the zone (Kroener et al., 2018), but there is no simple model available, to our knowledge, to include this mechanism.

CONTEXT 1

1.1 Water flow in the soil-plant-air continuum

On the leaves surface, there are pluricellular structures called the "stomata" forming aperture in the epidermis. They allow plants to exchange gases with the atmosphere. The two guard cells of these stomata have to keep the aperture open, so the atmospheric carbon necessary for plants to produce new assimilates can enter (Gaastra, 1959). However, the plants also lose water through those openings, due to large differences in water potential between the atmosphere and the inner part of the leaves. This diffusion of vapor out of the stomata generates a water potential difference between the different parts of the plant, cascading down to the rhizosphere[1]. It is equivalent to a pulling force, dragging water from the soil into the roots and upward to the shoot part. This cohesion-tension principle has been known for years (Bohm, 1893; Steudle, 2001; Tyree, 1997) to be the driving mechanism of water transport in plants.

Thus, the difference of water potential drives the water movement within the whole plant. However, since the resistance between the soil water and the stomata is very high, the plant water potential can become so negative that it triggers cavitation events inside the vascular vessels, locally breaking the water column (Cochard, 2002). Consequently, the plant may suffer wilt or perish unless it closes its evaporating sites (Draye et al., 2010). More so, it is crucial for the plant to maintain high relative humidity in the cells close to the stomata to keep up the production of carbohydrates (Lawlor, and Cornic, 2002). The other functions provided by the transpiration are a reduced excessive heating of the leaves and the transport of nutrients from the soil through upper plant organs. Therefore, the trade-off between water diffusion and atmospheric carbon acquisition is key to a harmonious plant development.

[1] **Rhizosphere**: soil zone within roots influence. Hereafter, defined as the radius of the root extraction zone. Equal to the half-distance between roots

1.1.1 Water limitation

The water limitation due to insufficient rainfall coupled with high evaporating demand is frequently considered as the biggest constraint to plant growth (Passioura, 2006). To mitigate this problem, the spatial and temporal synchronization of root and soil water is typically considered as determinants for the root water uptake processes (de Dorlodot et al., 2007; Manschadi et al., 2006). However, root system architecture does not simply define the water uptake pattern. The ease with which water travels through the continuum is defined by the hydraulic conductivity of each system element along the water pathway (Tyree et al., 1994). The root hydraulic conductance provides the intrinsic capacity of the root to absorb and transport water. The uptake of water will occur at the places where the local hydraulic conductances are high and if these regions are well connected to the plant collar by conductive xylem vessels. In addition, when the soil water near the root becomes limiting, the rhizosphere hydraulic conductivity can decrease drastically and prevent the roots to take up more water (Carminati, and Javaux, 2020; Schröder et al., 2009). Therefore, the combined hydraulic conductance of the soil and the root system has a major role defining the global water uptake ability.

Analogy of Ohm's law

To express the water fluxes in a system with small capacitance, biologists have come to realize that it is dependent on the water potential difference multiplied by the hydraulic conductance of the studied system. At the whole soil-plant-air scale, the water flow rate in the plant is similar to the electrical analogy of Ohm's law. In this case, expressed as:

$$J = (\Psi_{soil} - \Psi_{air}) * K_{spa} \tag{1.1}$$

where J is the total water flow rate $[L^3T^{-1}]$, Ψ_{air} is the water potential of the atmosphere $[P]$, Ψ_{soil} the bulk soil water potential $[P]$ and K_{spa} is the hydraulic conductance of the soil-plant-air continuum $[L^3P^{-1}T^{-1}]$. The order of magnitude for the different water potential are detailed along the pathway in Figure 1.1.

In general, the whole soil-root system hydraulic conductance is low in comparison with the shoot-air system during the day when soil water is abundant (Steudle, 2000). The root system can represent approximately 50% of the overall plant hydraulic resistance (Martre et

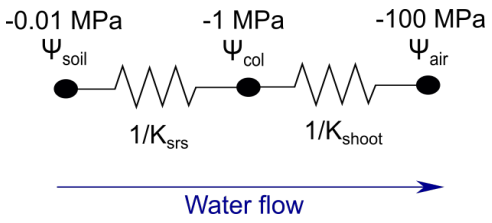


Figure 1.1: Order of magnitude for the water potential for three compartments along the water pathway (soil, collar, air).

al., 2001) (Figure 1.1). In addition, the soil hydraulic conductance can also decrease to a point where the soil water is considered disconnected from the root. This disconnection might minimizes water losses to the dry soil by hydraulic lift. However, the soil act as the water supply for the plant. Thus, the roots and the soil in its vicinity establish a critical link in the soil-plant-air continuum. When the soil-root system is considered to be the most limiting factor, it is possible to narrow down the equivalent conductance term (K_{spa}) to soil-root system one (K_{srs}).

Leaf water status

At the leaf organs, the stomatal conductance defines how easily water can exit the leaves and CO_2 can enter the leaves. For an isohydric plant such as maize (*Zea mays*), poplar (*Populus euramericana*), or grapevine (*Vitis vinifera*), when the stomata open, their conductance can reach values around 0.2 to 0.6 $molm^{-2}s^{-1}$. Then, the leaf water potential can drop from around -0.1 to -0.6 MPa to reach around -1.4 to -1.8 MPa after approximately two to five hours (Tardieu, 1993; Tardieu et al., 2017; Villalobos-González et al., 2019). In water deficit scenario, the stomatal conductance will tend to decrease and it is linked to an increase of the concentration of abscissic acid in the xylem sap (McAinsh et al., 1990).

1.1.2 Root system hydraulic architecture

Under the hood of the previous equation (Eq. 1.1.1), an incredibly complex hydraulic network stands. Indeed, the hydraulic properties of the roots and the soil are both highly heterogeneous, in space and time. The root segments have different anatomies, hydrophobic barriers and subcellular hydraulic properties that affect their radial hydraulic

conductivity (k_r) (Couvreur et al., 2018). The water content in the direct vicinity of the roots defines the local hydraulic conductivity of the soil which acts in series with the root radial hydraulic conductivity (Meunier et al., 2018a). Axially, the size, and number of functioning xylem elements, as well as the pit area and number per inter-vessel connections define the axial hydraulic conductance (Wason et al., 2021). Together, those radial and axial properties attached to each and every root segment creates a network of hydraulic pathways that connects every single roots to the shoot part. This whole network with its hydraulic properties can be summarized into the concept of **root system hydraulic architecture** (Doussan et al., 1998b; Landsberg, and Fowkes, 1978; Meunier et al., 2017a). Among all possible paths, the ones with the highest hydraulic conductance that connect the soil to the shoot define the absorption sites. Consequently, the preferential sites of root water uptake will also contribute to the heterogeneous soil water potential distribution, and this is true even in homogeneous soil water profile (Couvreur et al., 2012). To add up to the complexity, the soil zone impacted by the root water uptake, the rhizosphere, has no clear spatial boundary.

In soil, the water redistribution is a function of the hydraulic conductivity tensor, the spatial distribution of matric potentials, and the gravitational potential. In wet soil, plants can absorb water easily from the pores and capillary around its roots. At that stage, the pulling force required by the plant to take up the water is weak. However, as the water is removed from the soil, the pulling force needed to extract more water becomes greater due to a decrease of the soil hydraulic conductivity. This decrease of the hydraulic conductivity of the soil is a function of the water content, but also depends on the soil type and structure, capillary sizes, the tortuousity and surface-binding forces of the soil particles. The relationship between the soil water content and the matric potential is called the retention curve. In general, under wet soil conditions, the soil hydraulic conductivity is greater than the root radial hydraulic conductivity. However, the opposite occurs when the soil dries out, and the low soil hydraulic conductivity can quickly become the limiting factor in the system (Draye et al., 2010; Schröder et al., 2009).

1.1.3 Xylem embolism and stomata regulation

Previously, the xylem cavitation was briefly mentioned with the dramatic potential consequences on the water pathway within the plant. However, the xylem embolism phenomenon remains low in leaf veins,

even when plants experience water stress symptoms. The pit areas within inter-vessel connections can reduce the vulnerability of these sites. In addition, the xylem network organization can reduce the embolism spread beyond individual vessel air-seeding thresholds (Wason et al., 2021).

Furthermore, stomatal regulation contains cavitation to a minimum (Cochard, 2002). Depending on the plant and its sensitivity, the leaf water potential can be maintained constant (isohydricity) or not (anisohydricity). This regulation of the stomatal conductance is a passive process through the guard cell dehydration but can be overwritten with hormones signaling in an active response (Brodribb, and McAdam, 2017). However, the theory that transpiration is limited by the xylem vulnerability is challenged by the soil hydraulic conductivity loss that occurs when drought episodes happen (Carminati, and Javaux, 2020). Much is still to be unraveled, and more so as hydraulic properties are difficult to measure experimentally.

1.2 Complex root system hydraulics architecture

The complexity of the soil-plant continuum limited our quantitative understanding of the role of root system hydraulics. For the last two decades, computational models have been developed in that regard that can possibly bypass some experimental limitations and help us estimate root water uptake (Passot et al., 2018; Pierret et al., 2006). Today, state-of-the-art Functional-Structural Plant Models are able to numerically simulate water movement in the soil-plant-atmosphere continuum from the root uptake location to the shoot parts, such as: R-SWMS (Javaux et al., 2008), ROOTMAP (Dunbabin et al., 2013), or OpenSimRoot (Postma et al., 2017). The drawback is often the simulation time. As the window of interest is wide (both in space and time) and the asked resolution is high, the simulation time can increase greatly.

One of the potential new techniques to reduce the computational time is to use models that work with mixed dimensions, such as in Koch et al., 2021. They used geometric parameters as a metric to encompass the zone of influence of the roots in space. This reduced the mesh resolution near the roots and decrease the computational costs. This type of resolution offers, for the resolution of complex soil water flow in 3D space and non-linear equations, an increase in accuracy and in efficiency.

As our understanding of root water uptake increased, some concepts emerged to better describe the potential hydraulic dynamics of the plant. From complex root systems, we were able to reduce part of their hydraulic properties into some simpler variables, so-called macro-properties. These macro-properties reflect a mathematical need to quantify water uptake processes. More so, each macro-property reflects a dimension of the whole soil-plant water dynamics. The use of macro-properties are useful, simply to display a component of the root water uptake, or as upscale variables for models working on different scales (Couvreur et al., 2012). These models working with macro hydraulic properties linked to organ scaled models are potentially useful instruments for virtual breeding (Meunier et al., 2020). They allow researchers to investigate the performance of any desired combination of plant traits within any environmental condition, including contrasted pedo-climatic scenarios (Chapman, 2008).

1.2.1 Macroscopic root water uptake models

On the plant scale, the emergence of concepts such as hydraulic architecture makes the understanding of plant complex water uptake dynamics simpler. The macro-hydraulic properties have the advantage to implicitly take into account the whole root system hydraulic architecture and to be defined at the plant scale (Couvreur et al., 2012). As they are a full integration of the root system hydraulic architecture, they rely on an implicit understanding of organ scaled hydraulic properties. Here, the so-called micro-hydraulic properties are the radial hydraulic conductivity and the axial hydraulic conductance. Both are defined by the hydraulic anatomy of the roots (Couvreur et al., 2018).

To clarify the scope of macro- and micro-hydraulic properties, a list of the most used ones in this thesis is detailed below:

1.2.2 Macro-hydraulic properties

Root water uptake rate

When the points of interest are below ground, the concept behind the transpiration rates of a plant is shifted towards the soil. In such situation, the root water uptake rate corresponds to the amount of water which can be taken up by the root system and reach the plant's collar. In simulation, water dynamics are usually split into two concepts: the potential and the actual root water uptake rate: RW_{pot} vs. RW_{act}. Where the RW_{pot} is the maximum amount of water flux

allowed by the root system, and the RW_{act} is the actual water flux at the collar. To clarify the differences and nuances, for the root water uptake rate variables used in the manuscript, these terms are explained below through two equations. The equivalent root system hydraulic conductance K_{rs} refers to the ease with which water can be taken up by the whole root system $[L^3P^{-1}T^{-1}]$.
On the one hand, RW_{pot} is expressed as:

$$RW_{pot} = \Delta\Psi * K_{rs} \tag{1.2}$$

where $\Delta\Psi$ is the largest possible water potential difference between a wet and uniform soil water profile, and the plant collar. The hypothesis that we took is that, in this scenario, soil water is at -0.01 MPa and the leaf water potential is at -1.5 MPa. This corresponds to a well watered soil and high evaporative demand. The water potential within the plant collar was approximated as the leaf water potential. This would hold true if shoot hydraulic conductance was very high (which is often assumed to be the case for small plants).

Equivalent soil-root system hydraulic conductance

On the other hand the RW_{act} differs by the $\Delta\Psi$ which here corresponds to the actual water potential difference between the soil and the plant collar. In addition, while the K_{rs} is a variable that integrates the root system hydraulic architecture, it is decoupled from the soil hydraulic conductivity. As such, it is not able to take into account strong water potential gradients around the roots (which could arise in a situation of high evaporative demand). To counteract this limitation, K_{rs} can be changed to the equivalent soil-root system hydraulic conductance (K_{srs}), that integrates the soil matrix in the direct influence of the root system and its related hydraulic properties. This resulted into a new similar equation:

$$RW_{act} = (\Psi_{bulk\,soil} - \Psi_{col}) * K_{srs} \tag{1.3}$$

Where Ψ_{col} is the water potential at the collar, and $\Psi_{bulk\,soil}$ is the water potential of the bulk soil.

It should be noted that, although the K_{srs} integrates the hydraulic conductivity of the soil zone within the influence of roots as well as the root system, it does not show the ability of the root system to adapt its uptake distribution in response to an heterogeneous soil water potential distribution.

Standard Sink Fraction

The Standard Uptake Fraction (SUF) represents the relative distribution of root water uptake in a uniform soil water profile, based on the root system hydraulic architecture. In the whole soil domain, the SUF is extended and called the Standard Sink Fraction (SSF). Therefore, the SSF accounts for the normalized distribution of the sink term when the soil water potential is uniform.

The compensatory root water uptake conductance (K_{comp}) can be linked to the notion of the SUF (Couvreur et al., 2012). The K_{comp} $[L^3P^{-1}T^{-1}]$ provides a new compensatory conductance term which splits the relative distribution from the uniform soil water scenario to what happens in a heterogeneous soil water profile. The K_{comp} can be use in the following equation, which allows the estimation of the radial flux at the different root segments. In extreme case of compensatory water uptake, it brings an insight on the hydraulic lift phenomenon (i.e. water redistribution into the soil by the root system).

$$J_{r,i} = RW_{act} * SUF_i + K_{comp} * (\Psi_{sr,i} - \Psi_{s,eq}) * SUF_i \tag{1.4}$$

where $J_{r,i}$ is the water uptake of the root i-th segment $[L^3T^{-1}]$, SUF_i is the water fraction taken up by the i under uniform soil water profile, $\Psi_{sr,i}$ is the water potential at the root soil-root interface, and $\Psi_{s,eq}$ is the equivalent soil water potential felt by the plant.

Equivalent soil water potential

The equivalent soil water potential is defined as the weighted-mean water potential of all soil-root interfaces or alternatively expressed as:

$$\Psi_{s,eq} = \sum_{i=1}^{N} \Psi_{sr,i} * SUF_i \tag{1.5}$$

1.2.3 Micro-hydraulic properties

Radial hydraulic conductivity

Our understanding of radial water flow through the root cross sections follows the composite transport model of Steudle, and Peterson (1998). It is a combination of cell-to-cell and apoplastic water movement following a set of paths that offers the highest hydraulic conductance. The radial hydraulic conductivity is thought to be an important limiting factor to the water uptake. The hydraulic conductivity of the

root is primarily determined by the overall structure of the root cross section anatomy and the development stage of the organ. In parallel, anatomy and development stages are subjected to genetic and environmental background. The recent evidences of this laid in the diverse root anatomical traits found within species such as maize (Burton et al., 2013b; Tai et al., 2016) or cassava (Bomfim et al., 2011) and between species (McDonald et al., 2002) and biomes (Ma et al., 2018; Yamauchi et al., 2021).

The way these ranges of root traits influence the root radial hydraulic conductivity (k_r) is being actively researched. A series of anatomical traits have already been shown to impact k_r, such as the number of cell layers in the cortex (Chimungu et al., 2014b), the size of cortex cells (Lynch et al., 2014), the presence of aerenchyma (Cuneo et al., 2016; Schneider et al., 2017) or potentially the ratio between different root tissue areas (Yamauchi et al., 2021). On the hydraulic side, the k_r is influenced by the expression and localization of water channels (aquaporin) (Hachez et al., 2006; Javot, and Maurel, 2002), the formation of hydrophobic barriers (Enstone et al., 2002) or the conductivity of plasmodesmata (Couvreur et al., 2017).

Generally speaking, cell hydraulic properties are assumed to control the short- or medium-term response by the plant over the radial hydraulic conductivity, while the anatomical traits are assumed to be associated with the long-term response (Vetterlein, and Doussan, 2016). As such, root anatomy defines the baseline for the root radial and axial hydraulic properties.

MECHA

At the root cross-section level, Couvreur et al. (2018) developed a mathematical model that computes the flow of water across the root whole root cross section (MECHA). As it works at the scale of walls, membranes, and plasmodesmata of individual cells, it unlocks the possibility to analyse the influence of cell-scaled hydraulic properties on the k_r. For example, the use of the model pinpointed that root k_r might be very sensitive to the size and structure of plasmodesmata, despite their low hydraulic conductance. MECHA, and its two transverse spatial dimensions, allows accounting for cell placement, aerenchyma lacuna or the locations of xylem vessels that could disturb the water flow rates across the root. As a result, this model requires an accurate representation of the cell arrangement in the root cross section (a ".xml file" formatted according to CellSet standard of Pound et al.) in order to estimate the radial fluxes of water across it.

Different hydraulic scenarios can be estimated with the model, such as the ones with an endodermal Casparian Strip, or with a suberized endodermis, with passage cells, etc.

The digital segmentation of the root cross section is a limitation to the use of such a model, as it is time-consuming. Consequently, in combination with a root anatomy generator, MECHA could possibly open the way to systematically analyse the functional properties of a large number of root anatomical traits and cell-scaled hydraulic properties.

Axial hydraulic conductance

Most of the plant water transport over long distances takes place in the vascular network formed by the xylem vessels. These dead cellular structures in rows are similar to hydraulic pipes. Hence, the root axial hydraulic conductance ($K_x[L^4P^{-1}T^{-1}]$) is often calculated with the Hagen-Poiseuille law. Therefore, it is possible to obtain K_x with the sum of the individual contribution of each xylem element to the hydraulic conductance:

$$K_x = \sum_{i=1}^{N} \frac{\pi r_i^4}{8\eta} \tag{1.6}$$

where r is the radius of the i-th xylem vessel, and η the water dynamic viscosity ($\pm 1 m.Pa.s$)

The onset of cavitation in the xylem is also thought to have an impact on the root water uptake. The overall influence of the breakdown of some water pipe is that it increases the path length and the hydraulic resistance of a root segment. Unfortunately, the vulnerability curve, which describes the likelihood of xylem cavitation in terms of the percentage loss of hydraulic conductivity as a function of xylem water potential, are uncertain (Tyree, and Sperry, 1988). They are mostly described with probability function (Ogle et al., 2009).

1.2.4 Subcellular hydraulic properties

The hydraulic conductivity of a cell membrane can be divided into two components. First, the part where water flow through the phospholipid bilayer cell membrane accounting also for other compounds at the exception of the aquaporins. Second, the contribution of the aquaporins to the cell membrane permeability.

Contribution of aquaporins to the cell membrane hydraulic conductivity

Aquaporins are proteins from a very large family of intrinsic protein (MIP) which are specialized in water transport. The subgroup PIPs are the plasma membrane intrinsic proteins (Javot, and Maurel, 2002; Johnson et al., 1989). They can be regulated through different mechanisms. Hormonal molecules such as ABA, up-regulate aquaporin in Maize, but others, such as auxin and Citokinin, down-regulate it (Hose et al., 2000). These proteins will then respond to the intercellular pH and Ca^{2+} levels, phosphorylation, heteromerization, or reactive oxygen species(Maurel et al., 2008; Tyerman et al., 2002). In response to circadian rhythm, osmotic or water stress, these different regulation pathways allow the plants to change their cell membrane permeability rapidly. The regulation can also occur at a gene expression level. The most expressed aquaporins in maize roots are the PIP2,5 proteins. Radially, they are not uniformly distributed in the root cell layers, and Ding et al., 2020 showed that they are mostly present in the endodermis and the exodermis, which may be crucial points to regulate water movement (Javot, and Maurel, 2002).

Cell walls

Cell walls are composed of cellulose, hemi-cellulose, pectin and proteins which can change the hydraulic conductivity of these structure. There is a potentially wide variation of hydraulic conductivity for cell walls depending on the proportions and properties of the constituting elements.

Usually, in the cortex tissue, the water flow is considered as following mainly the apoplastic pathway. Therefore the hydraulic properties, which emerge of this complex medium, highly influence the water movement through the apoplast.

Plasmodesmata

Plasmodesmatal pores are junction between cells, as they offer a direct path between cell symplast, their individual hydraulic conductance are the main factor for the cell-to-cell water pathway. The hydraulic conductance of plasmodesmatal pores can be reduced by the deposition of molecules, such as callose. These depositions on the neck regions of the plasmodesma constrict the aperture, reducing the conductance of such structure (Radford et al., 1998). Plasmodesmatal permeability can also respond to change in cell turgor (Hernández-Hernández et

al., 2020; Oparka, and Prior, 1992), and osmotic treatments (Schulz, 1995).

1.2.5 Offset between the radial and axial hydraulic conductivities along the root

The global root water uptake dynamics along the root are often described with some level of compartmentalization. Along the roots, the modification of value in the ratio between the axial and the radial hydraulic conductivities are associated with different functions in terms of water uptake. Close to the tip of the root, usually there are high values of k_r and low K_x. In this young part of the root, the accumulation of hydrophobic molecules in the endodermis is often segregated to some radial cell walls (i.e. Casparian strip, Figure 1.3). In that case, apoplastic water flows are barely distributed, providing many paths of least resistance to reach the endodermis. Once inside the stele after crossing the endodermis cell layer, the only functioning xylem vessels counting are the small ones in the perimeter of the outer stele boundary (Cornelis, and Hazak, 2021; Steudle, and Peterson, 1998).

Further away from the root tip, as hydrophobic substances tend to accumulate in specialized tissue layers, the k_r decreases. Meanwhile, the meta-xylem living cells die and open-up as large water channels with several orders of magnitude higher axial hydraulic conductance (Figure 1.2). However, the xylem vessels network is not a simple succession of capillary tubes. Pit membranes at the interconnection of the different cells play an important role for the integrity of those structures (Wason et al., 2021) and can reduce the axial hydraulic conductance. In addition, the xylem vessels undergo a postmortem lignification (Pesquet et al., 2013) which adds up to this integrity. Thus, the younger part of the root is often considered as the root zone where most of the absorption happens while the older part is associated with the axial water transport. The offset between the maturation of hydrophobic barriers limiting the radial pathway and the maturation of the meta-xylem is therefore a major factor influencing the root water uptake capacity (Sanderson, 1983).

1.3 Non-unique site-specific eco-ideotypes

Beyond the hydraulic consideration and root placement in the 3D space, these roots must be produced at some point, and most of their

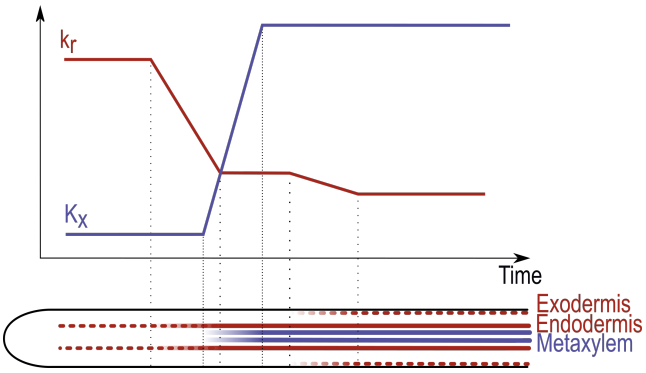


Figure 1.2: Offset between k_r and K_x along the root. Conceptual representation of the variation of radial (k_r) and axial (K_x) conductivities due to the maturation of hydrophobic structure (dashed red lines = Casparian strip; full red lines = complete suberization of the cell walls) and the maturation of the meta-xylem vessels (blue lines).

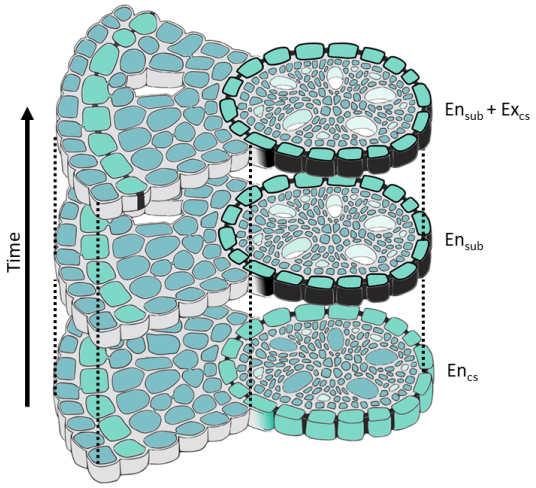


Figure 1.3: The three main root maturation stages encompassed in the thesis are represented on sliced root cross-section (schematic view). The cellular tissues of the endodermis and the exodermis are highlighted in lighter "green-blue" in contrast to other cell types. En_{cs} = Endodermal Casparian Strip; En_{sub} = suberin deposition in the cell walls of the endodermis; Ex_{cs} = Exodermal Casparian Strip.

cells which compose them have to be maintained alive, so the roots can keep fulfilling their functions. These production and maintenance costs are resources which cannot be allocated to anything else, such as for grain filling or for shoot biomass that are valued at the harvest. The root system and its exudates are perhaps the major carbon sink of the plant, as in some cases $> 50\%$ of all the photosynthates are consumed by the root system (Lambers et al., 2002). In addition, Kong et al. (2021) highlighted the pivotal role of the root radius, the cortex cell size, as well as the number cortex cell layers for the carbon consumption rate. For a single plant, the root system size is also proportional to the root system hydraulic conductance. Hence, an old root system has usually a higher hydraulic conductance than its younger self. Something to keep in mind here is that these anatomical structures and the root diameter also have an impact on the root ability to uptake water, as detailed above in subsection 1.2.3. It seems that there is some relation between the carbon cost of a root system and its ability to take up water. In pursuit of finding an efficient root system that confers drought stress tolerance and/or avoidance, several authors, such as Lynch (2013) for maize or Comas et al. (2013) for wheat, have proposed specific combinations of optimal phenotypes that should minimize water limitations and potentially optimize yield under scarce water conditions (Donald, 1968).

However, many root traits conferring drought tolerance present dual effects as a function of water availability and climatic demand: they can be positive in a wide range of drought scenarios and negative under different drying conditions (Leitner et al., 2014; Tardieu, 2012; Tardieu et al., 2017). Furthermore, in many cases, impacts of specific traits are studied alone and it is not always clear whereas it would actually lead to improvement in field conditions, where several stresses can occur at the same time.

Nevertheless, the development of new computational models at the cellular, and at the plant scale provide new investigation tools to investigate root water uptake dynamics on different levels. Even if they seem disconnected, the macro- and micro hydraulic properties are emergent properties from the models which link models together and form a structured modeling network across scales. Therefore, this association of models could be used to conduct performance study on combinations of root traits in contrasted pedo-climatic conditions.

1.3.1 Virtual phenotyping

For this specific task, Meunier et al. (2019) developed the Maize Root System Hydraulic Architecture soLver (MARSHAL). The advantages are that it allows the computation of the root system hydraulic conductance and other macro hydraulic properties in a matter of seconds for a predefined pedo-climatic condition. It also includes age-dependent radial and axial hydraulic conductivities and the fully explicit 3D-root system architecture. Therefore, this tool has the ability to show the root scale hydraulic traits which offers the desired functional root water uptake dynamics. However, the root system architecture and the soil water profile remain static in this case.

The missing parts to make a virtual assessment of plant hydraulic behavior in contrasted pedo-climatic condition are: (i) some soil feedback as the plant growth; (ii) the evolution of the transpiration demand, and (iii) an idea about quantification of the carbon cost. Thus, coupling MARSHAL with models which account for these elements could pave the road toward virtual phenotyping of any desired combination of root traits in any pedo-climatic condition. Hence, there is a need to go deeper into the root traits selection. As mentioned, root cellular arrangement and cell-scaled properties have a great impact on k_r, K_x, but also the metabolic cost. Soil water models which include the implicit macro hydraulic properties exist (e.g. Hydrus). A simplistic transpiration demands of a plant can be quantified from weather data through Penman-Monteith equations (Allen, and FAO, 1998). However, a systematic assessment of the functional implications of different anatomical traits has never been done for water uptake.

Indeed, the in vivo quantification of k_r is usually performed using a root pressure probe (Hose et al., 2000), which is experimentally restrictive and hard to perform on soil-growth roots. In addition, it is not amenable for large scale studies. This experimental restriction creates a knowledge gap in the quantitative assessment of individual components of the root cross section hydraulic architecture.

1.4 Conclusive remarks on the thematic background

While the mechanisms of water flow are being uncovered, the highly specialized network formed by the root system still holds many secrets. Because knowledge is fragmented, integrated frameworks including different scales are still needed to understand how plant root traits

diversity can help us find better water uptake strategies for our crops. This would help evaluate the potential impact of modification and improve the understanding of phenotyping data.

1.4.1 Zea mays

As maize is the studied species, a few specifications are still necessary to be clarified.

Maize susceptibility to water limitations

Maize is quite sensitive to drought, particularly during the reproductive phase, just before the flowering. In addition, the potential impact of climate change over this species are pessimistic, with a possible strong reduction of productivity (Jägermeyr et al., 2021). On the opposite, in specific climate, maize phenological development could accelerate and can have a positive effect on yield (Žydelis et al., 2021). In average, yield reduction varies between species due to water limitation. Yet, the yield reduction is about $\pm 40\%$ when the maize plant is confronted with soil water deficit at this crucial phenotypic stage (Daryanto et al., 2016). The reason behind this, is the delay of the anthesis-silk interval because of the reduced cell growth in silk apex (Fuad-Hassan et al., 2008; Herrero, and Johnson, 1981). The desynchronization of pollen shedding and silking of maize results in a low grain set (Struik, and Makonnen, 1992).

Maize roots system

The root system of maize can be divided into an embryonic and a post-embryonic root system. The embryonic root system consists of a tap root and a variable number of basal roots (also named seminal roots). The post embryonic root system is made up of shoot-born roots which emerge on the shoot nodes. If the node is below ground, they are called crown roots. On average there are six underground whorls, while above ground nodes are the production center of the brace roots. The mean diameter and number of shoot-born roots per whorls increase at higher nodes (Yang et al., 2019). All these major root types are called axial roots in opposition to the lateral roots. The lateral roots are often classed into two groups but Passot et al. (2018) revealed more nuanced classification based on the elongation rate and the diameter of the lateral roots.

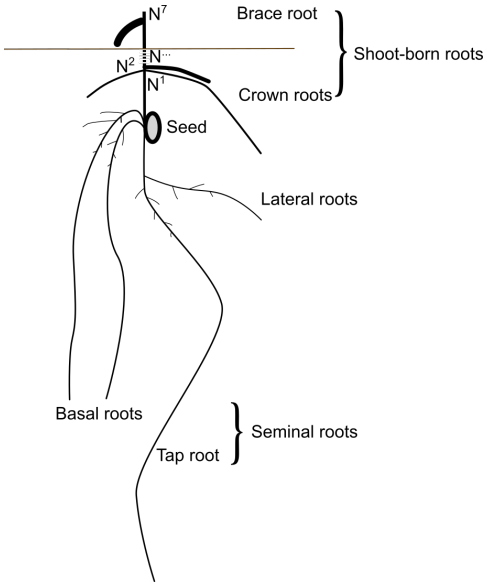


Figure 1.4: Representation of maize root system architecture. Each "N" stands for a distinct node along the shoot part.

Maize root anatomy

Anatomically speaking, the maize root cellular organization is similar to most monocotyledonous crops species. Radially, the cells are arranged by concentric cell layers for the most part. The central cylinder is constituted of stele cell tissues with the differentiated meta-xylem vessels spread at the perimeter of the cylinder (Figure 1.5). Usually, two to three protoxylem strands, which alternate with primary phloem, are arranged per meta-xylem vessel (Feldman, 1994). The pericycle forms the outermost layer of the central cylinder. The following tissue layer is the endodermis. Depending on the maturation stage of the root, this endodermis tissue layer has the particularity of having lignin and/or suberin deposition at its cell walls. These hydrophobic molecules create barriers which impedes more the apoplastic water movement. All these cell tissues constitute the whole stele. Beyond this point, several parenchymatous cortex cell layers build up the root radius, followed by the exodermis and the epidermis cell layer. The exodermis cell layer can also have similar cell wall deposition properties to the endodermis. It can form a secondary wall of defense

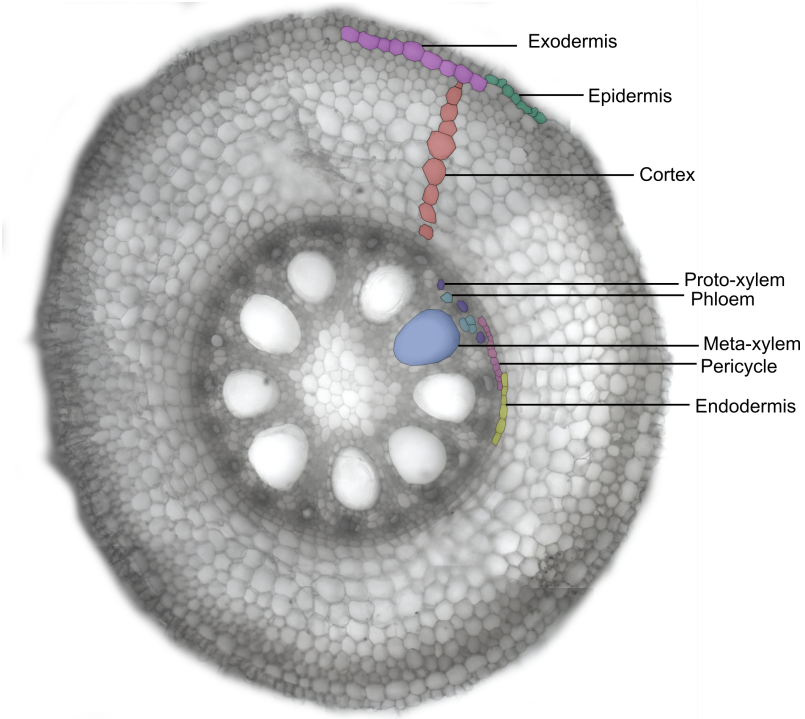


Figure 1.5: Shoot-born root of a maize cultivar B73 at 10 cm from the apex. Created using the free hand cross-section method.

against apoplastic radial water flow. In the cortex layer, by apothosis, cavities can replace living cells, merging and forming aerenchyma lacuna in rows. Cell walls remaining after the death of the cells are not always recycled, which forms septa between the different lacuna. The function of the aerenchyma is described as reducing the maintenance cost of the roots, bringing oxygen down for the cell respiration and potentially decreasing the k_r.

PART II

ROOT ANATOMY & FUNCTION

The second part of the thesis focus primarily on the root cross-section level. First, on a structural point of view, we will explore *how does the anatomy impact the root radial hydraulic conductivity?* This will be the foundation of the thesis, as it is the establishment of the technique to estimate the root radial hydraulic conductivity with modeling tools. This will require the representation of the root anatomy and the possible inclusion of subcellular hydraulic properties.
Secondly, this new method will be applied on a whole root system to propose a new way of generating hydraulic atlases of root system.
Thirdly, we will quantify the different effects of the anatomy and the subcellular hydraulic properties on the radial hydraulic conductivity using machine learning algorithm to fasten the estimation process.

I am among those who think that science has great beauty. A scientist in his laboratory is not only a technician: he is also a child placed before natural phenomena which impress him like a fairy tale. We should not allow it to be believed that all scientific progress can be reduced to mechanisms, machines, gearing, even though such machinery has its own beauty.

Marie Curie

GENERATION OF MAIZE ROOT CROSS-SECTION ANATOMY

2

This chapter is a modified version of a manuscript published as:

> Adrien Heymans, Valentin Couvreur, Therese LaRue, Ana Paez-Garcia, and Guillaume Lobet. GRANAR, a Computational Tool to Better Understand the Functional Importance of Monocotyledon Root Anatomy. Plant Physiology, 2020.

ABSTRACT

Root hydraulic conductivity is a limiting factor along the water pathways between the soil and the leaf, and root radial conductivity is itself defined by subcellular hydraulic properties and anatomical traits. However, quantifying the influence of anatomical traits on the radial conductivity remains challenging due to complex time-consuming experimental procedures. We present an open-source computational tool, the Generator of Root Anatomy in R (GRANAR), that can be used to rapidly generate digital versions of contrasted monocotyledon root anatomical networks. GRANAR uses a limited set of root anatomical parameters, easily acquired with existing image analysis tools. The generated anatomical network can then be used in combination with hydraulic models to estimate the corresponding hydraulic properties. We used GRANAR to reanalyze large maize (*Zea mays*) anatomical datasets from the literature. Our model was successful at creating virtual anatomies for each experimental observation. We also used GRANAR to generate anatomies not observed experimentally over wider ranges of anatomical parameters. The generated anatomies were then used to estimate the corresponding radial conductivities with the hydraulic model MECHA (model of explicit cross-section hydraulic architecture). Our simulations highlight the large importance of the width of the stele and the cortex. GRANAR is a computational tool that generates root anatomical networks from experimental data. It enables the quantification of the effect of individual anatomical traits on the root radial conductivity.

2.1 Introduction

Root water uptake is influenced by a multiscale combination of structural and hydraulic properties (Lobet et al., 2014; Passot et al., 2019). At the root system scale, the overall root architecture defines the potential uptake sites within the soil domain. Hydraulic properties of individual roots (radial and axial conductivities) further constrain these uptake sites, thus establishing a global hydraulic architecture of the plant (Meunier et al., 2017b). Changes in these local hydraulic properties, which have a global influence, are thought to be an important target in breeding programs for drought-resistant crops (Tardieu et al., 2018).

At a finer scale, on the organ level, radial and axial conductivities can also be defined by hydraulic and structural properties. On the hydraulic side, the radial conductivity (k_r) of a root segment is influenced by the expression and location of water channels (Hachez et al., 2006), the deposition of hydrophobic barriers (Enstone et al., 2002), and the conductivity of plasmodesmata (Couvreur et al., 2018). On the structural side, k_r is influenced by anatomical traits, such as the number of cell layers in the cortex (Chimungu et al., 2014b), the size of cortex cells (Lynch et al., 2014), or the presence of aerenchyma (Fan et al., 2007). Generally speaking, a plant controls its hydraulics in the short and medium-term (Hachez et al., 2012), and its structural features over longer developmental timelines (Vetterlein, and Doussan, 2016). As such, root anatomy defines the baseline for the root radial hydraulic properties.

Root anatomical traits are diverse within species, such as maize (*Zea mays*; (Burton et al., 2013a,b; Tai et al., 2016), rice (*Oryza sativa*; (Vejchasarn et al., 2016)) or cassava (*Manihot esculenta*; (Bomfim et al., 2011), between species (McDonald et al., 2002; Wahl, and Ryser, 2000), and in different biomes (Ma et al., 2018). However, to our knowledge, an assessment of the functional implication of anatomical traits in water uptake properties has never been done in a systematic way. Indeed, the *in vivo* quantification of radial and axial conductivities are usually performed with a root pressure probe (Hose et al., 2000; Schneider et al., 2017; Schreiber et al., 2005), which is experimentally restrictive, because it is hard to perform on soil-grown roots and is generally seen as a low-throughput procedure. This experimental restriction has hindered the investigation of the relation between root hydraulic properties and anatomical traits.

Recently the development of a modeling tool of transverse water

flow in roots from the subcellular scale, MECHA (model of explicit cross-section hydraulic architecture), opened the way to the systematic analysis of the influence of anatomical and subcellular hydraulic properties on k_r (Couvreur et al., 2018). A remaining limitation of the approach is that it requires explicit anatomical networks as input. Such networks can be obtained by digitizing cross-section images with semi-automated tools, such as CellSeT (Pound et al., 2012). However, that procedure is very time consuming for large datasets. Therefore, there is a need for a high-throughput method of acquisition of root anatomical networks (Passot et al., 2019).

Here, we present a new computational tool, the Generator of Root Anatomy in R (GRANAR), that can generate digital versions of monocotyledon root anatomical networks. GRANAR uses easily accessible anatomical traits as input. These tissue-scale parameters can be acquired from open-access image analysis software and root cross-section images. In combination with the model MECHA, GRANAR opens up new possibilities to systematically analyze the impact of root anatomy on hydraulic conductivity in a high-throughput fashion. GRANAR has been validated using published datasets of maize anatomical data and hydraulic measurements. GRANAR is an open-source project available at https://granar.github.io/.

2.2 Material and methods

2.2.1 Description of the GRANAR model

GRANAR was developed in R and is available as an R package.

To create a network anatomy of a root cross-section, the GRANAR model is based on the placement of the cell layers around the center of the root. The model first places the innermost cell layer (the stele), then progressively builds the root toward the outermost layer (the epidermis). Coordinates of the cell center for each tissue type are established as a function of the diameter of the cells that compose the tissue. The cell type diameter is defined by the *cell_diameter* parameter for each cell type. The parameter *n_layers* defines the number of cell layers for each tissue type independently (Table 2.1). The only exception is for the stele, where the number of cell layers is calculated by dividing the diameter of the stele (*layer_diameter*) by the stele cell diameter. To create a unique network for every run of GRANAR, a random factor (randomness) adds a slight variation to the coordinate of stele and cortex cell centers.

Table 2.1: List of parameters used by the model to generate root cross-sections.

Tissues	**Parameters**		
Stelar parenchyma	Cell diameter	Layer diameter	
Central cylinder pith	Cell diameter	Layer diameter	
Pericycle	Cell width	Number of layers	
Endodermis	Cell width	Number of layers	
Inner Cortex	Cell width	Number of layers	
Mid Cortex	Cell width	Number of layers	
Outer Cortex	Cell width	Number of layers	
Exodermis	Cell width	Number of layers	
Epidermis	Cell width	Number of layers	
Xylem	Cell diameter	Number of meta-xylem	ratio
Aerenchyma	Area proportion	Number of lacuna	
Root hair	Length	Number of root hair	

Specific vascular tissue patterns are created depending on whether the user chooses to simulate monocot or dicot anatomy. For monocots, the xylem vessels of a defined radius (max_size) are placed at the periphery of the stele. For dicots, the vascular blades are placed on defined radius from the center to the last layer of the stele. The size of the largest xylem element in the centrum is determined by the max_size parameter. The other xylem elements along the vascular blade have a decreasing size, which is proportional to the distance from the center until it reaches the minimum size of a stele cell diameter (Figure: 2.1).

Once all cell centers are placed, the model creates the cell boundaries (cell walls). A voronoi tessellation of the cell centrums, using the *"deldir"* package (Turner, 2019), creates the cell walls at mid-distance between every cell center previously set. The epidermis cells do not have any neighbor cells on the outer part. However, an outside layer similar to the epidermis is created for the sake of the voronoi tessellation, then removed once it is done. Once the tessellation is done, the area of the different cells is then computed by the *'polygon'* function of the *"sp"* package.

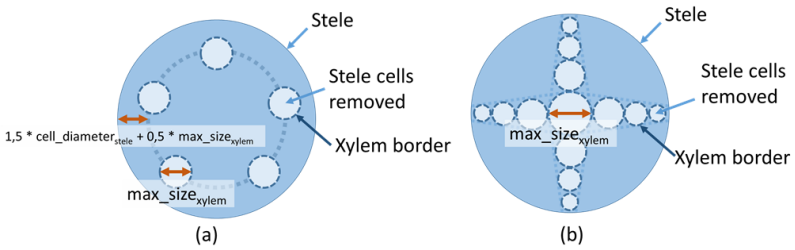


Figure 2.1: Overview of the methodology to create the vascular elements. A, Monocotyledon stele cross-section. B, Dicotyledon stele cross-section. In both (A) and (B), the stele cells inside the xylem border (dark blue) are removed to create xylem cells, indicated by light blue arrows. The different parameters used to build the root cross-section simulation are described in light blue shaded boxes and indicated by double-headed red arrows.

2.2.2 Description of the GRANAR package

The GRANAR model is available as an R package. The package contains the following functions:

- *read_param_xml* (path = "*parameter_file.xml*")

  Loads the parameter files that are under XML format and produces a data frame object with the information needed to generate a root cross-section with the function *create_anatomy*.

- *create_anatomy* (parameter = *parameters*,
  path = "*parameter_file.xml*")

  Generates a root cross-section with a data frame containing the needed parameter or calls the *read_param_xml* function to load a parameter file under XML format directly. The object returned by the function is a list containing four data frames:

  - A nodes data frame with the coordinates of all points of all the cells, their identity, and the information needed to create the cell polygons.
  - A walls data frame with the condensed information of all cell walls.
  - A cells data frame with the detailed information about the cells: area, distance from the center, and their angle in the cross-section.

  - An output data frame with details information for each tissue.

- *get_root_section* (path = "*cross_section.xml*")

  Imports the geometry information (the nodes data frame) about root cross-section from the file generated with GRANAR or CellSeT.

- *plot_anatomy* (sim = obj, col = *"type"*)

  Makes a figure which represents the given geometrical data. Accepted arguments for the col (color) parameter are '*type*', '*area*', '*dist*', '*id_cell*' and '*angle*'. Default = '*type*'.

- *write_anatomy_xml* (sim = obj, path = "*simulation.xml*")

  Saves the geometry information generated with GRANAR in an XML file (the same output format as CellSeT).

It can be installed very easily on R thanks to the *"devtools"* package (Wickham, and Chang, 2019) with the function: *install_github*("*granar/granar*"). The "*granar*" package relies on few dependencies. These dependencies are: the "*deldir*" package (Turner, 2019), the "*alphahull*" package (Rodriguez Casal, and Pateiro-Lopez, 2010), and the "*retistruct*" package (Sterratt et al., 2013). They should be installed (e.g. *install.packages*(*deldir*)) before loading the "*granar*" package.

2.2.3 Description of the MECHA-GRANAR connection

MECHA reads XML-formatted CellSeT data to load the geometry information it needs to compute the radial conductivity. GRANAR was built to generate outputs in the same format as CellSeT. Therefore, the coupling of those tools is easily made and examples can be found at this address: https://github.com/granar/granar_examples [10.5281/zenodo.3068671]. The coupling is done by file exchange.

2.2.4 Description of the experimental data used for the validation of maize (Zea mays) root anatomies

The Burton et al. (2013b) and Chimungu et al. (2014b) datasets were produced using RootScan software. RootScan produces a range of root anatomical traits, most of which are identical as the input parameter for GRANAR. Nonetheless, a few transformations were

needed to pass from RootScan output to GRANAR input. They are summarized below in Table 2.2. In addition, some anatomical traits were not calculated by RootScan. For instance, stele and pericycle cells were assumed to have a diameter of 0.011 mm. The stele cell diameter assumption was made by pooling known data (Couvreur et al., 2018; Gao et al., 2015; Steudle et al., 1993). The endodermis and the exodermis were also assumed to have the same diameter as cortex cells, and epidermis cells were assumed to have a third of the cortex cell diameter because RootScan does not distinguish differences between those cell types. Additionally, epidermis cells were not accounted for in the number of cortex layers in RootScan. In that regard only two cell layers were removed to the cortex layer count of RootScan data in the transformation procedure (Table 2.2). One last assumption was made concerning the number of xylem vessels. Thanks to (Moreno-Ortega, 2016) data, which show a linear regression between the stele diameter and the number of xylem vessels (Spearman correlation coefficient = 0.82, p value < 0.001), the number of xylem vessels was estimated based on the stele diameter.

2.2.5 Overview of the methodology to transform RootScan data into GRANAR parameters

Table 2.2: Function list used to transform RootScan data into GRANAR parameters.

GRANAR Input	**Transformation**	**RootScan Output**
Stele cell diameter (S_c)	$0.011\ mm$	-
Stele layer diameter (S_l)	$= 2\sqrt{\frac{TSA}{\pi}} - 2.S_c$	Stele area (TSA, mm^2)
Number of meta-xylem (nX)	$= 33\sqrt{\frac{TSA}{\pi}}$	Stele area (TSA, mm^2)
Meta-xylem diameter (MX_c)	$2\sqrt{\frac{MXA}{nX.\pi}} - S_c\,/\,2$	Meta-xylem area (MXA, mm^2)
Cortex cell width (C_c) Endodermis cell width (En_c) Exodermis cell width (Ex_c)	$= (\sqrt{\frac{RXA}{\pi}} - \sqrt{\frac{TSA}{\pi}})/CF$	Cross-section area (RXA) Number of cortex layer (CF)
Epidermis cell width (Ep_c)	$= C_c\,/\,3$	-
Aerenchyma proportion (P_a)	-	Aerenchyma proportion (PA)

The Burton et al. (2013b) dataset used in this study included the anatomical traits of 195 landraces emphasizing accessions from stressful soil environments. The data are available in their Supplemental Tables S1 and S2. The Chimungu et al. (2014b) dataset used in this study was imported from their Supplemental Tables S3 and S4, which were lists of genotype anatomical traits selected from the IBM (Intermated *B73 x Mo17*) population and from the Malawi maize breeding program.

The extraction of the anatomical traits from the Gao et al. (2015) dataset was conducted with ImageJ software. The anatomical traits gathered were exactly the same as the input parameters of GRANAR except for units. The anatomical traits data used in our study can be found in their Table 1. The aerenchyma traits of Gao et al. (2015) were found in their Figure 8. The Gao et al. (2015) dataset includes the anatomical traits of three root types of maize *cv. Zhengdan958* exposed to a low nitrogen treatment.

To create the three replicates of each data point, three runs of GRANAR were made and saved separately for each entry.

2.2.6 Description of MECHA hydraulic parameters

The simulation framework MECHA (Couvreur et al., 2018) estimates k_r from the root cross-section anatomy generated with GRANAR or CellSeT (Pound et al., 2012) and from the subcellular scale hydraulic properties of walls, membranes, and plasmodesmata. Cell wall hydraulic conductivity was set to $2.8 * 10^{-9} m^2 s^{-1} MPa^{-1}$, as measured by Zhu, and Steudle (1991) in maize. Lignified and suberized wall segments in the endodermis and exodermis (Figure 2.2) were considered hydrophobic and attributed null hydraulic conductivities. The protoplast permeability (L_{pc}, $7.7 * 10^{-7} ms^{-1} MPa^{-1}$) measured by Ehlert et al. (2009) was partitioned into its three components: the plasma membrane intrinsic hydraulic conductivity (k_m), the contribution of aquaporins to the plasma membrane hydraulic conductivity (k_{AQP}), and the conductance of plasmodesmata per unit membrane surface (K_{PD}). The latter parameter was estimated as $2.4 * 10^{-7} ms^{-1} MPa^{-1}$ (Couvreur et al., 2018), based on plasmodesmata frequency data from Ma, and Peterson (2001), and the plasmodesmata conductance estimated by Bret-Harte, and Silk (1994). By blocking aquaporins with an acid-load treatment, Ehlert et al. (2009) measured a k_{AQP} of $5.010^{-7} ms^{-1} MPa^{-1}$. The remaining value of k_m after subtraction of k_{AQP} and k_{PD} from L_{pc} was $0.3 * 10^{-7} ms^{-1} MPa^{-1}$. Each value

of k_m, k_{AQP}, k_{PD}, and L_{pc} was set uniform across tissue types. For details on the computation of k_r, see Couvreur et al. (2018).

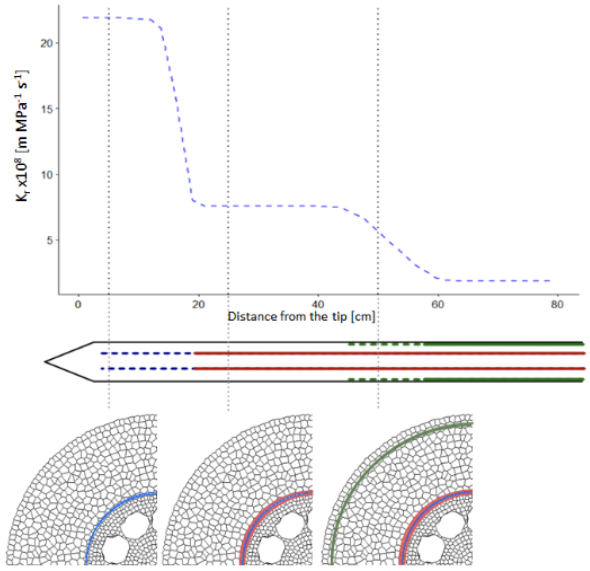


Figure 2.2: Estimated evolution of the k_r in main axes of the maize root system derived from Doussan et al. (1998a). Top, k_r as a function of distance from the maize root tips. Bottom, the illustrations depict our assumption of the evolution of main apoplastic barriers based on Enstone, and Peterson (2005). The different lines represent different levels of apoplastic barriers. 1: Endodermal Casparian strip (dashed blue); 2: Endodermal suberization (red); 3: Endodermis full suberization and exodermal Casparian strip (dashed green).

2.2.7 Statistical analysis

All statistical analyses were made using **R** (R Core Team, 2018). No distinction between the three datasets was made to compute the *R squared*, the Pearson coefficient of correlation, and the p values in the validation experiment. All ANOVAs were performed using the *"aov"* function from *'stat'* package. Correlation analysis was performed using the *"ggpairs"* function from *'GGally'* package.

2.3 Results

2.3.1 Overview of GRANAR

The GRANAR model generates cell networks of root cross-sections from a small set of root anatomical traits (Table 2.1). The root anatomical traits can typically be gathered by using software image analysis, such as ImageJ (Schneider et al., 2012), or with more automated software, such as RootScan (Burton et al., 2012), PHIV-RootCell (Lartaud et al., 2014) or RootAnalyzer (Chopin et al., 2015). Briefly, the anatomy generation process is based on the placing of cell layers around the center of the root. The position and size of each cell and cell layer is a function of the cell type radius and user-defined randomness. As a result of this randomness, each simulation produces a slightly different anatomy, even with the same input parameter set. The thickness of a specific tissue is therefore a function of its cell's size and its number of layers. Specific vascular tissue patterns are created depending on whether the user chooses to simulate a monocot or a dicot anatomy (Figure 2.3). The vascular pattern of dicotyledon is illustrative with the current version of the GRANAR model. Independent of the species, in Figure 2.3, GRANAR was able to reproduce cross-section anatomies with high similitude (relative error: 3.4%, R^2: 0.9997) over the total area of the cross-section between the experimentally obtained cross-section and the one obtained with GRANAR.

Once the root anatomy was created, the cell network can be saved in a file in eXtended Markup Language (XML). The file in XML can serve as the geometry input for the MECHA model. As such, both tools can be linked, and the GRANAR-MECHA model can be used to estimate hydraulic properties (e.g. k_r) of any type of root anatomy. The format of the XML created by GRANAR is identical to the ones created by CellSeT which also generates a fully digitized root anatomical network. Using the same format for both tools makes them modular and facilitates the inter-comparison of their outputs (Figure 2.4).

The time (both computational and labor time) required to access the level of network detail with CellSeT in Figure 2.4 is around 10 h in cross-sections with thousands of cells, such as maize (image blending and correction [$30min$] + automated segmentation [$3s$] + iterative corrections of the segmentation and labeling [$\pm 10h$]). In comparison, generating a complete network anatomy only takes 10 min (root anatomical traits [7 *min* RootScan/image or 10 *min* ImageJ/image]

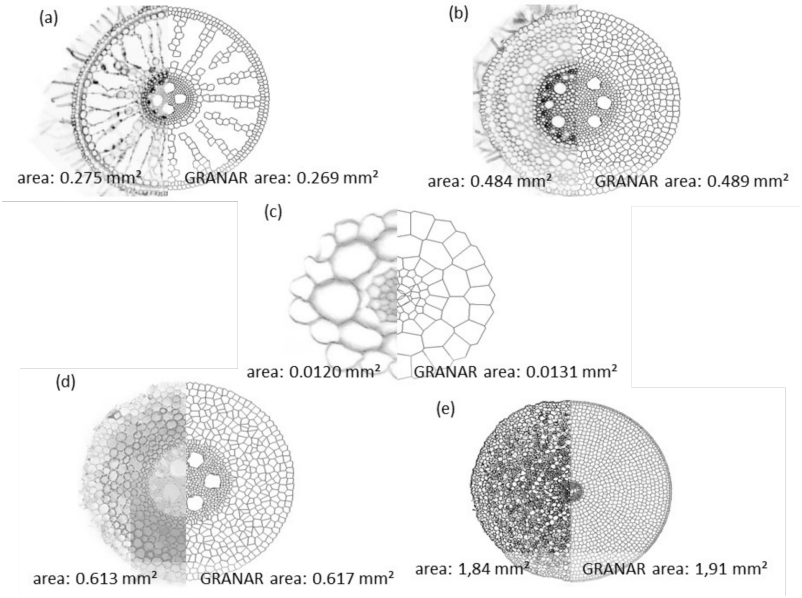


Figure 2.3: Visual comparison between root cross-section images of different plants and their simulation with GRANAR. A, Rice adventitious root grown hydroponically and collected 10 cm above the root tip. B, Wheat (*Triticum aestivum*) 'Savannah' mature adventitious root grown in soil and collected 5 cm from stem. C, Arabidopsis primary root grown on an agar plate collected 5 cm from the root tip. Initial image cross-section comes from figure 4 in (Atkinson et al., 2017). D, Maize (*B73 line*) crown root grown aeroponically and collected 5 cm from the root tip. Initial image cross-section comes from Hachez et al. (2006). E, Mature *Ranunculus* root (Reynolds, 2014). The area information below each image corresponds to the total area of the cross-sections. The model parameters used for the simulations were gathered with ImageJ and are available at https://github.com/granar/granar_examples.

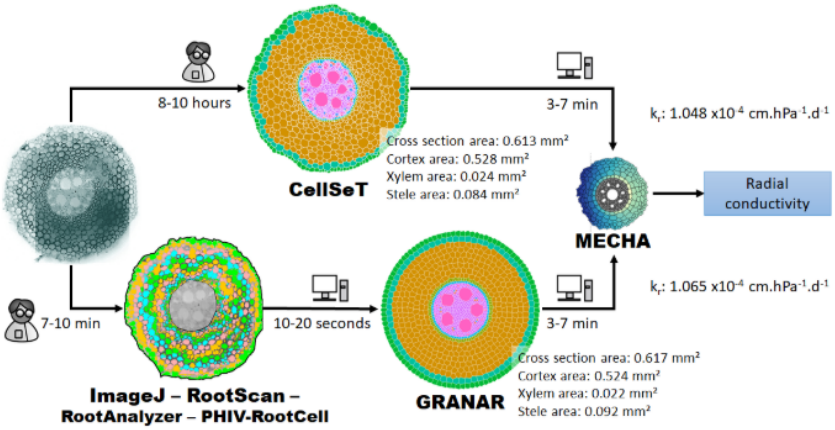


Figure 2.4: Comparison of GRANAR- and CellSeT-based methods used to estimate single-root scale hydraulic properties. The input parameters of GRANAR in the figure were gathered with ImageJ. The radial hydraulic conductivity (k_r) values were calculated using the MECHA model assuming an endodermal Casparian strip as the only apoplastic barrier and uniform subcellular hydraulic properties. The time (indicated as either person or computational using associated graphics) required for each procedure is detailed next to each arrow.

+ GRANAR/cross-section [$15s$]). However, when we compared the k_r obtained by MECHA using either CellSeT or GRANAR anatomy as input, the difference is less than 2% (Figure 2.4).

2.3.2 Generation of diverse anatomies

We validated the output of GRANAR for maize, whose root anatomy is well documented in the literature. We used the experimental data from three independent datasets showing large phenotypic diversity of maize anatomical traits. The three root anatomical datasets were from Burton et al. (2013b) (195 landraces from a diversity panel), from Chimungu et al. (2014b) (38 maize genotypes with large variance of cortex traits), and from Gao et al. (2015) (1 cultivar with 3 different root types and a large proportion of aerenchyma in all the 3 root types). These different datasets contain tissue-scale anatomical data that could be used as input for GRANAR, such as the size of the stele or the number of cortex layers (details about how this data was compiled to create the GRANAR input files are presented in

the "Materials and Methods" section). Using the 239 entries, we generated 717 maize root cross-sections, with three repetitions per entries. Each data point was used to generate three replicates of each root, taking advantage of the randomness in the positions of the individual cells. Another root anatomical dataset from Wahl, and Ryser (2000) containing 19 different perennial grass species was also converted into input parameter files for GRANAR. Their anatomies were generated as well. Similar results were found as compared with the three maize datasets (Annexe 1).

Once all the anatomies were created, we compared organ-scale area-based metrics (that were not directly used as input to create the anatomies) between the experimental and simulated data (Figure 2.5). Area-based comparison is relevant to assess anatomical similarities between the generated anatomies and the ones used as input as demonstrated in the sensitivity analysis. GRANAR was able to accurately represent the total areas and sizes of the different tissues of the root (e.g. Figure 2.5A, total cross-section area; Figure 2.5B, total cortex area, Figure 2.5C, xylem area; Figure 2.5D, aerenchyma area). For each variable analyzed, the r-squared value between the simulated and experimental data was greater than 0.95. The relative error of GRANAR was less than 5% for the total cross-section area, the total cortical area, and the xylem area and less than 15% for the aerenchyma area. For each variable analyzed, no significant differences were found between experimental and simulated data ($P > 0.05$).

2.3.3 Estimation of the radial hydraulic conductivity with GRANAR-MECHA

By design, the anatomical output of GRANAR can be used as an input for the MECHA model (Couvreur et al., 2018). We were therefore able to estimate the k_r for each of the experimental data points, assuming constant subcellular hydraulic properties (see "Materials and Methods" for details). The simulated k_r (across the different root cross-sections) varied between 21.1 and 8.1 10^{-8} $m.MPa^{-1}.s^{-1}$ assuming a hydrophobic endodermal Casparian strip as the only apoplastic barrier.

Using the results of these simulations, we were able to attribute the main changes of k_r to three parameters using a linear regression model (Table 2.3). The simulated k_r for those data points can then be estimated using the following equation:

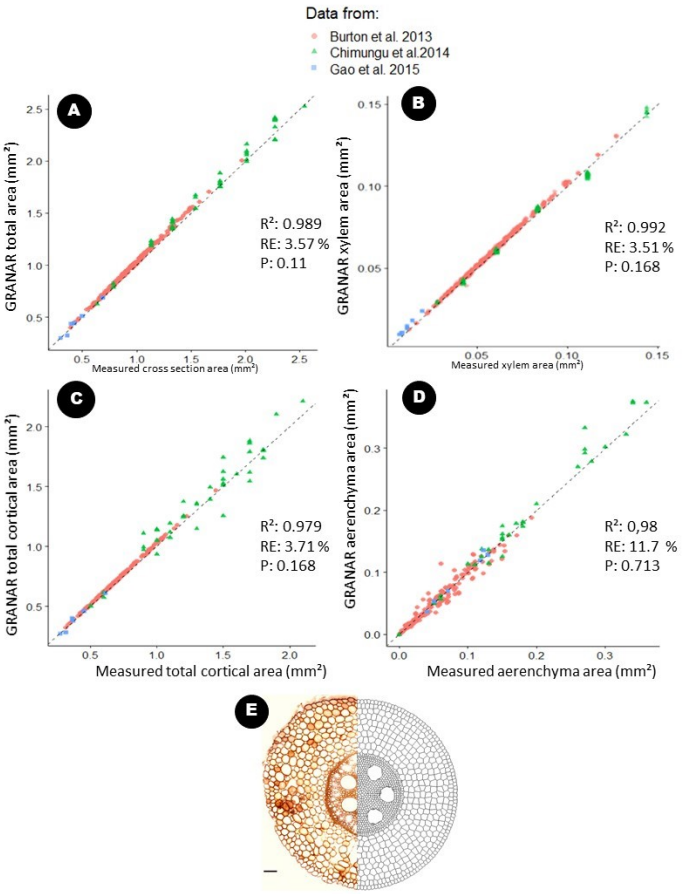


Figure 2.5: Comparison between simulated and experimental anatomies for four anatomical traits. A, Total cross-section area. B, Cortical area. C, Xylem area. D, Aerenchyma area. The different colors and shapes represent the different datasets. The dashed lines represent the 1:1 line. RE, relative error; R^2, R-squared; P, P-value for the F test. E, Illustration depicting one initial image (Chimungu et al., 2014b) and the generated anatomy side by side. Bar = 100 μm.

$$k_r.10^7 = 1.98 + 4.25\,XVA - 0.731\,TCA - 0.0209\,P_a + 0.188\,XVA.P_a \quad (2.1)$$

where k_r is the simulated radial conductivity ($m.MPa^{-1}.s^{-1}$), XVA is the xylem vessel area (mm^2), TCA is the total cortical area (mm^2), and P_a is the aerenchyma proportion (defined as the ratio between the aerenchyma area and non-stellar tissues area).

Table 2.3: Summary of the ANOVA for the effect of the xylem and the total cortical area combined with the aerenchyma proportion on the k_r when the only apoplastic barrier is an endodermal Casparian strip.

Variable	**Sum of Squares**	**F Values**	***P*-value**
XVA	$1.069E^{-14}$	157	< 0.0001
TCA	$2.452E^{-13}$	3599.9	< 0.0001
P_a	$4.09E^{-14}$	600.5	< 0.0001
XVA * P_a	$6.54E^{-15}$	96.1	< 0.0001
Residuals	$7.00E^{-17}$	-	-

The most substantial correlation factor to the simulated k_r was for the cortex width (corr: -0.84; $P < 0.05$, Table 2.4). As a general rule, as the cortex width increases, the k_r decreases (Figure 2.6A). In addition, for a given cortex width, as the xylem area increases, the k_r increases (Figure 2.6A). The ratio between the stele area and the total area of the cross-section is also highly correlated to the k_r (corr: 0.79, $P < 0.05$, Table 2.4). In this regard, as the ratio between the stele and the cross-section area increases, the k_r increases (Figure 2.6B). Additionally, for a given ratio between the stele and the cross-section area, as the xylem area decreases, the k_r increases (Figure 2.6B). Moreover, in the analyzed dataset, an increase in aerenchyma proportion seems to only slightly decrease the simulated k_r (Figure 2.6C). The simulated k_r of our study and the ones measured in the literature for maize were in the same range (Figure 2.7).

2.3.4 The anatomical traits effects on radial hydraulic conductivity

In the previous section, we used the GRANAR-MECHA model to study the theoretical effect of experimental root anatomical traits

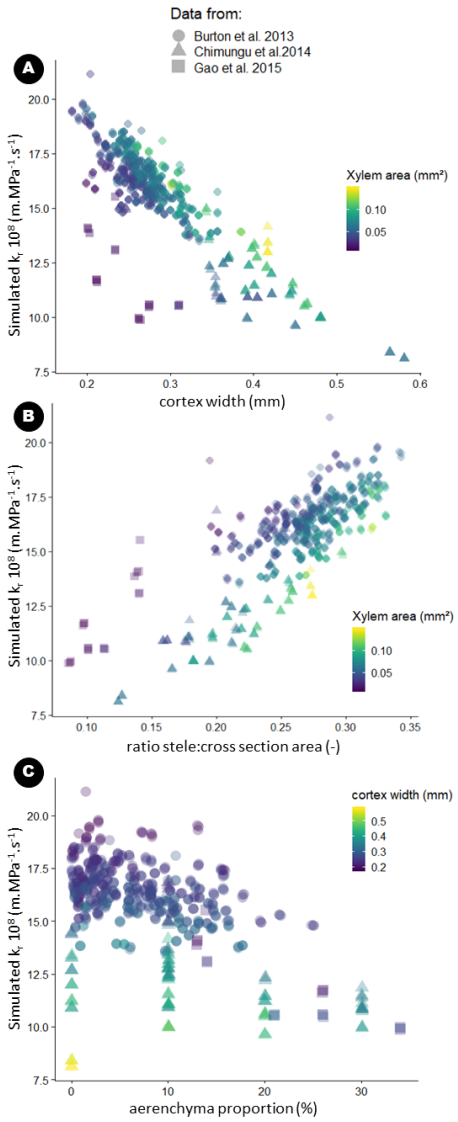


Figure 2.6: Relationship between simulated k_r and anatomical traits for each dataset. Scenario with endodermal Casparian strip. Symbol shape corresponds to datasets. A, Effect of the cortex width on the simulated k_r. Colors represent the xylem area. B, Effect of the ratio between the stele area and the total cross-section area. Colors represent the xylem area. C, Effect of aerenchyma presence on the simulated k_r. Colors represent the cortex width.

Table 2.4: Summary of the ANOVA for the effect of one-by-one anatomical trait on the simulated k_r assuming an endodermal casparian strip as the only apoplastic barrier. Each line shows results from a single one-way ANOVA.

Variable	Radial Conductivity			
	Corr. Coef. of Pearson	**R-square**	**F value**	***P* value**
RXA	-0.624	0.389	448.4	< 0.0001
TSA	-0.222	0.049	36.64	< 0.0001
TCA	-0.715	0.511	736.5	< 0.0001
LCA	-0.638	0.407	483.1	< 0.0001
MXN	-0.252	0.063	47.54	< 0.0001
XVA	-0.175	0.03	26.61	< 0.0001
CCN	0.037	0.001	0.962	0.327
AA	-0.632	0.4	468.4	< 0.0001
P_a	-0.505	0.255	241.3	< 0.0001
CW	-0.841	0.708	1704	< 0.0001
TSA:RXA	0.792	0.627	1181	< 0.0001

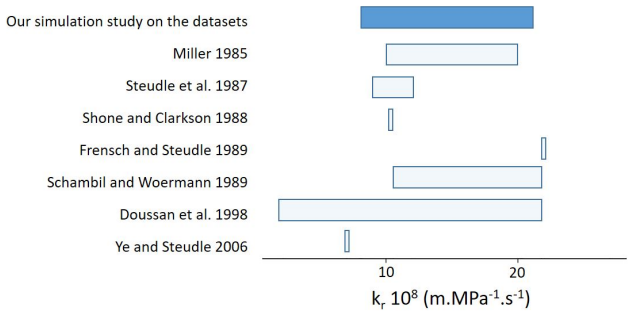


Figure 2.7: Comparison between simulated and measured k_r values in maize.

on the root k_r. The advantage of a modeling approach is that each anatomical traits can be changed independently from the others, which is often impossible experimentally. The capability to change anatomical traits independently allows for a more complete exploration of the theoretical phenotypic spectrum.

Here, we chose to vary the proportion of aerenchyma, the size of the cortex, and the size of the stele as well as the number and area of xylem vessels. For each trait combination, we computed the k_r for three different maturity levels (Figure 2.2). The maturity levels account for three approximate distances from the root tip corresponding to different levels of apoplastic barrier development. Based on Doussan et al. (1998a) and Enstone, and Peterson (2005) we assumed the following apoplastic barrier types for the different distances: 1 = presence of endodermal Casparian strip (5 cm); 2 = presence of suberized endodermis (25 cm); and 3 = presence of suberized endodermis and exodermal Casparian strip (30 cm).

The first anatomical trait we chose to vary was the proportion of aerenchyma, which ranged from 0% to 50% of the cortex area (Figure 2.8). The range observed in the experimental datasets spanned 0 to 35% (see previous section). An increase in aerenchyma induced a decrease in the simulated k_r. The effect was less important as the endodermis started to suberize. However, under the maturity level 3, with a fully suberized endodermis and an exodermal Casparian strip, the relative k_r decrease was stronger than the one observed at maturity level 2 with a suberized endodermis (Figure 2.8). The stronger relative decrease can be explained by the reduced number of cells after the exodermis layer, which allow the water to pass from a cell-to-cell to an apoplastic pathway, whereas there is no shifting of preferential pathway of water next to the exodermis at maturity level 2.

To observe the influence of the cortex traits on the k_r, a range of cross-sections were simulated with increasing cortex cell diameter and numbers of cortex layers (Figure 2.9). We observed an increase of all components induces a decrease in the simulated k_r (Figure 2.9, A, C, D). Moreover, the cortex width (isolines in Figure 2.9A) accounts for the coupled effect of the cell diameter and the number of layers on the simulated k_r. This anatomical trait neatly captures the decreasing trend of k_r with increasing cortex width for the global simulated dataset included in Figure 8B (unlike Figure 2.9, C and D, displaying a single transect across the parametric space each).

The relative influence of each cortex feature was greater at matu-

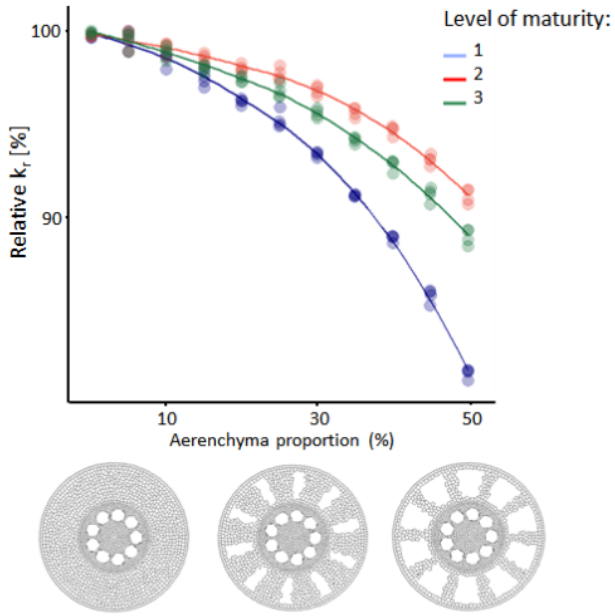


Figure 2.8: Influence of the proportion of aerenchyma on the relative k_r for simulated monocot anatomies. The colors represent different levels of hydrophobic barrier development. 1: Endodermal Casparian strip (blue); 2: Endodermal suberization (red); 3: Endodermis full suberization and exodermal Casparian strip (green). The cross-sections at the bottom of the figure, from left to right, show examples of roots with 0%, 25%, and 50% of aerenchyma.

rity level 1 than for the other maturity level tested. Each additional apoplastic barrier reduced the relative influence of the cortex traits over the water flow. Moreover, under maturity level 3, the cortex traits had the lowest relative influence on the conductivity in comparison with the other ones. Increasing the stele area while keeping the cortex width constant led to an increase of the simulated k_r (Figure 2.10). The influence of the stele area was highest in the scenario with maturity level 2.

Figure 2.11 shows the influence of increased xylem area on k_r. To increase the xylem area, the number of the xylem vessels was increased as well as the size of each pole. As a general rule, having more xylem vessels increases the simulated k_r. However, k_r reached a plateau when the xylem nearly covered the whole stele perimeter

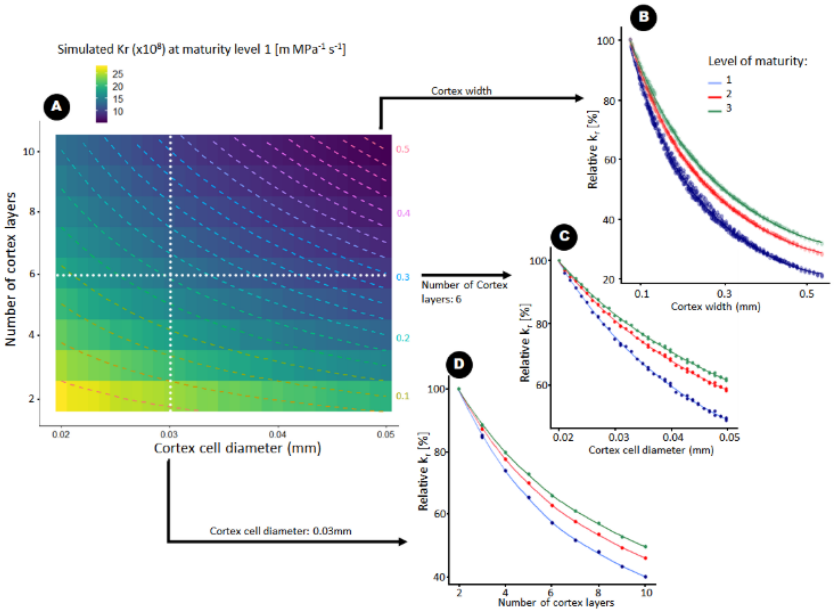


Figure 2.9: Influence of cortex anatomy (number of cortex layers and cell size) on k_r for simulated monocot anatomies. A, Overview of k_r values across the parametric space where endodermal Casparian strip is the only apoplastic barrier. The colored dashed lines represent the cortex width isoline (mm), and the dotted lines are a visual representation of the fixed parameters for the two subplots (C and D). B, Evolution of the relative k_r as the cortex width increases. C, Evolution of the relative k_r as the cortex cell diameter increases for the number of cortex layers fixed to six. D, Evolution of the relative $k_r$as the number of cortex layers increases for a cortex cell diameter set to 0.03 mm. B to D. The colors represent different levels of hydrophobic barrier development. 1: Endodermal Casparian strip (blue); 2: Endodermal suberization (red); 3: Endodermis full suberization and exodermal Casparian strip (green).

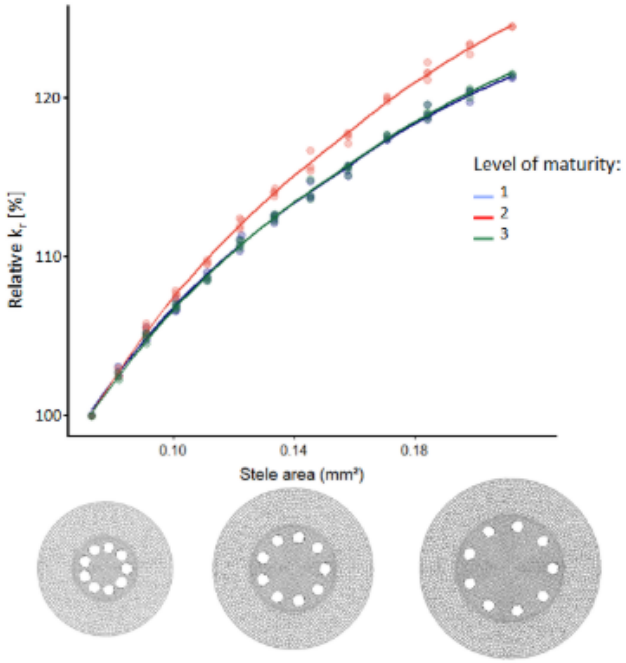


Figure 2.10: Influence of the stele area on the relative k_r for simulated monocot anatomies. The colors represent different levels of hydrophobic barrier development. 1: Endodermal Casparian strip (blue); 2: Endodermal suberization (red); 3: Endodermis suberization and exodermal Casparian strip (green). The cross-sections at the bottom of the figure, from left to right, show examples of roots with 0.3, 0.4, and 0.5 mm stele diameter.

(Figure 2.11A). The relative influence of the increase of the xylem number was the greatest at maturity level 1 compared with other maturity levels.

2.4 Discussion

Previously, when analyzing root anatomical data, scientists had to make compromises. On the one hand, a complete digitalization of the root anatomical network, which might be needed for further computational analysis, was possible to use semi-automated tools, such as CellSeT (Pound et al., 2012). However, this procedure is time consum-

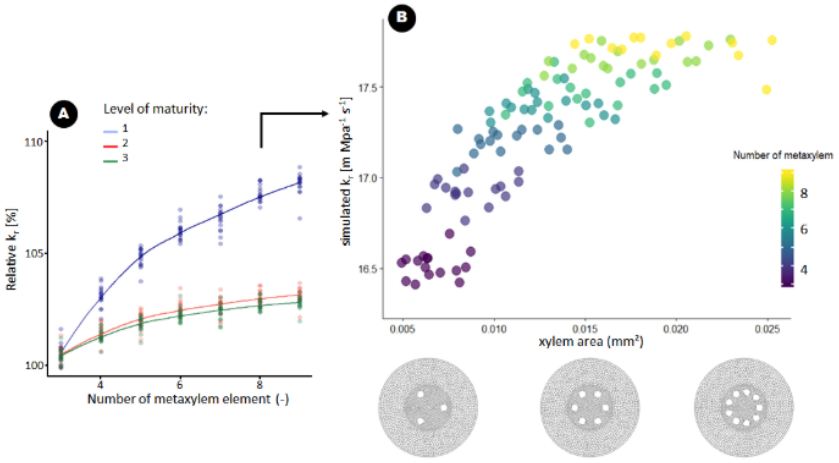


Figure 2.11: Influence of xylem features on the k_r for simulated monocot anatomies. A, Influence of the number of xylem vessels on the simulated relative k_r. The colors represent different levels of hydrophobic barrier development. 1: Endodermal Casparian strip (blue); 2: Endodermal suberization (red); 3: Endodermis full suberization and exodermal Casparian strip (green). B, Influence of the xylem area on the simulated k_r. The simulated k_r was calculated using an endodermal Casparian strip as the only apoplastic barrier

ing, especially for large roots. On the other hand, tissue-scale metrics could be automatically obtained from large datasets using other tools, such as RootScan (Burton et al., 2012), PHIV-RootCell (Lartaud et al., 2014), or RootAnalyzer (Chopin et al., 2015). Such a high throughput pipeline yields quantitative descriptive properties, but does not reach the level of detail required for analysis of the functional role of root anatomy in functional structural plant models (Passot et al., 2019).

With GRANAR, we aimed to bridge the gap between these two pipelines so that researchers do not have to make trade-offs between time consumption and quality of the analysis. Our new method uses tools that gather anatomical traits to create GRANAR input parameters (examples are given in the "Materials and Methods"). GRANAR then generates a complete root anatomical network, which can be used for downstream root functional analysis (Figure 2.4).

GRANAR coupling with other tools enables the estimation of functional properties from root anatomical networks. For instance,

combining GRANAR with MECHA (Couvreur et al., 2018) enables the estimation of the k_r of a root cross-section (Figure 2.4). Other computational tools, such as OpenAlea (Pradal et al., 2008), could use the complete cell network anatomy generated by GRANAR to analyze other functional properties, such as root radial growth. As such, cell wall geometrical information can be integrated with mathematics to simulate how cell tissue behaves with different growth rates, local strain, and elastic deformation of cells under turgor pressure (Chopard et al., 2007). For Arabidopsis (*Arabidopsis thaliana*), a single stereotypical root cross-section was modeled by Dyson et al. (2014) to understand how cell properties and shapes contribute to tissue-level extensibility and yield. Their study could be extended to more diverse and larger roots with GRANAR.

Overall, our simulations showed the cortex width is one of the major predictors of k_r. When the size of the cortex increases, the conductivity decreases, and it is mostly due to an increase in the length of the apoplastic pathway, as shown in our simulation cases. The larger the cortex is, the longer the path between the soil surface and the xylem vessels. Even when apoplastic barriers are fully developed, the cortex thickness still influences the conductivity greatly (Figure 2.9). The influence of the cortex width on k_r was already found experimentally for a wide range of species (Rieger, and Litvin, 1999). Cortex traits have also been found as a factor of drought tolerance (Chimungu et al., 2014a,b; Lynch et al., 2014). Chimungu et al. (2014b) showed increasing the cortex cell diameter would reduce metabolic costs of soil exploration and consequently improve drought tolerance. In that regard, our results showed for the same amount of cell layer, increasing cortex cell size would also reduce k_r and limit water uptake. Reduced k_r would constitute a water saving strategy for the plant (Lynch et al., 2014). Additionally, Chimungu et al. (2014a) showed a reduction of the number of cortical layers would also reduce metabolic cost and therefore improve drought tolerance by enabling deeper rooting depth and increased water uptake. Here, our results showed a reduction of the number of cortical layers would increase k_r and effectively ease water uptake. Thus, as Lynch (2015) suggested, roots with a small number of cortex layers and large cortex cells should have a small metabolic cost. However, our results showed this would have a compensatory effect on k_r because few cortical layers and large cortical cells have an opposite effect (Figure 2.9, C and D). We suggest instead a combination of few but large cortical cell layers which should show deep rooting ability thanks to the low metabolic cost and a small value

of k_r.

Our simulations show an increase in the aerenchyma proportion leads to a decrease in root k_r. This has also been shown experimentally in maize (Fan et al., 2007). The reduction of the number of parallel pathways due to the formation of aerenchyma is likely the cause of the observed reduction of k_r (Figure 2.8). Lynch, and Brown (2008) showed increasing the aerenchyma reduces the root metabolic cost, which in turn enables deeper rooting depth and improves drought tolerance. It has to be noted the aerenchyma proportion is an anatomical trait independent from the many other anatomical traits (Burton et al., 2013b). We acknowledge that we do not know if cell hydraulic properties change with the aerenchyma formation in nature. This discrepancy may explain why in Fan et al. (2007) the observed k_r reduction is stronger than what we estimated with our simulation.

Recent studies show a large number of meta-xylem vessels with small diameters improves drought tolerance (de Souza et al., 2013; York, and Lynch, 2015). A hypothesis to explain the drought tolerance mechanism of small xylem diameter is the reduction of cavitation likelihood (Li et al., 2009). Another hypothesis is the reduction of axial water fluxes (Lewis, and Boose, 1995), which correspond to the water saving strategy (Lynch et al., 2014). In addition, our results showed an increase of the k_r as the number of xylem vessels increases. Moreover, Huang, and Nobel (1993) have found a positive correlation between the number of xylem vessels and the k_r in *Ferocactus acanthodes* and in *Opuntia ficus-indica*. Nevertheless, our simulation also showed the decreasing size of xylem vessels alone would also decrease the k_r (Figure 2.11), which would lead to a water-saving strategy. Another study showed a drought tolerant plant (sorghum, *Sorghum bicolor*) expresses few xylem vessels and large cortex (Salih et al., 1999). In this case, the two factors would limit k_r.

The stele area, to our knowledge, has not been explored as a drought tolerant factor in the field. However, Moreno-Ortega (2016) experiment on maize lateral roots showed a strong correlation between stele diameter and the number of xylem vessels, which was discussed above. In our study, we simulated the change of stele diameter without changing the number of xylem vessels, and the stele alone had a strong impact on k_r (Figure 2.10). The increased simulated k_r as the stele area increased was mostly due to the increase of the pathway area.

The influence of anatomical traits changes with the development of apoplastic barriers. As detailed in the sensitivity analysis for each of the anatomical traits, the relative influence of each feature generally

decreases as the number and strength of apoplastic barriers increase. The reason for this decrease is that the relative influence on water flow of the apoplastic barriers in comparison with anatomical variation is increasingly strong. This behavior typically occurred with the simulation for the cortex traits and with the simulation for the xylem. Rieger, and Litvin (1999) justifiably show apoplastic barriers alone do not explain all changes in k_r. However, our simulation shows relative influence of anatomical variation changes as the apoplastic barriers increase (Figs. 2.8-2.11). This, to our knowledge, has not been pointed out in the literature. Further investigation could shed light on experimental data, where such trends are observed.

As shown in this manuscript, GRANAR is able to reproduce the general anatomical traits of varied experimental data. However, the anatomies produced by GRANAR remain a stereotypical representation of root cross-sections. Specific traits, such as uneven cell divisions (for instance, due to the formation of a lateral root) in specific locations, will not be represented using GRANAR. As a result, scientists might want to use manual image analysis tools to capture such specific anatomical traits. At this stage, it is also worth noticing GRANAR does not represent structures formed during secondary growth (secondary xylem and phloem).

Another current limitation of GRANAR is its static aspect. The model does not explicitly simulate the growth and development of the different cell layers. The root anatomy is the result of a generative algorithm and is fixed in time. One possible improvement to GRANAR would be to include a developmental module within the model, similar to the current root architectural models (Barczi et al., 2018; Postma et al., 2017; Schnepf et al., 2018). This would allow the model to create root anatomies for different root ages in one simulation, enabling the estimation of the evolution of the root conductivity with the root maturation. The downside would be that such a model would be more difficult to parametrize, making it more difficult to link to experimental datasets.

A third limitation of our current pipeline is the lack of information regarding some of the cell layers. Although tools such as RootScan (Burton et al., 2012) or PHIV-RootCell (Lartaud et al., 2014) can automatically extract some of the needed variables, they do not extract all of them. For instance, some assumptions were made in our research regarding the cell size in the epidermis, endodermis, pericycle, stele, and exodermis (see "Materials and Methods" for details). It would therefore be useful to have a concerted development for both the model

and the image analysis tools to create a fully integrated pipeline.

Finally, most of the data presented here were obtained on maize. This choice was a practical one, as maize was the only plant for which we could find sufficiently large and detailed datasets. In the future, additional validation of GRANAR should be performed for other species. The data on the 19 different perennial grass species from Wahl, and Ryser (2000) show the way toward the global validation of GRANAR for monocotyledons. This would be facilitated if experimental data (in this case the images) were more widely shared within the community (e.g. on figshare or Zenodo).

2.5 Conclusion

GRANAR is a new open-source computational tool that is able to generate a range of root anatomies for both monocots and dicots (http://granar.github.io). The input of the models can be rapidly acquired using existing image analysis tools. As output, GRANAR produces an explicit representation of the root anatomy as a network of connected cells. These networks can serve as input for other models, such as MECHA, and be used to estimate functional properties (here radial hydraulic conductivities) of specific anatomies.

In this manuscript, we validated GRANAR by reanalyzing large published datasets of maize root anatomies. GRANAR was able to represent the large range of experimental root anatomies. In addition, by coupling GRANAR with MECHA, we were able to estimate the hydraulic properties of the different anatomies in the dataset. This analysis highlighted the importance of the cortex width and the stele area as major factors influencing the root radial conductivity.

We also used GRANAR-MECHA to further explore the theoretical link between anatomy and radial conductivity. By creating 1000s of theoretical anatomies, we were able to assess the functional importance of individual anatomical properties such as the number of xylem vessels, the proportion of aerenchyma or the size of the stele. The analysis highlighted most anatomical variables have an influence on the hydraulic properties of the root. Their relative importance varied and functioned at the level of apoplastic barrier development. As a general rule, the influence of the anatomical traits was smaller when apoplastic barriers (in the endodermis and exodermis) were present.

In conclusion, we presented GRANAR, a new computational pipeline for the functional characterization of root anatomy.

In the previous Chapter, we learned how to generate root cross-section networks which can be used to estimate the radial hydraulic conductivity in combination with some subcellular hydraulic properties.

We figure it out that this new method could be applied to a root system. From anatomical traits, we could, perhaps, derive an Atlas of the root hydraulics functions associated with the root typology, assuming constant subcellular hydraulic properties over that root system.

Thus, this next Chapter is the result of the application of the new modeling techniques at the root system scale. In addition, we wanted to provide a new root hydraulic atlas, with a higher spatial resolution and which would include more root types than its predecessors.

CREATION OF ROOT HYDRAULIC CONDUCTIVITY ATLASES FROM CROSS-SECTION IMAGES AND MODELING TOOLS

3

This chapter is a modified version of a scientific article published as:

> Adrien Heymans, Valentin Couvreur, and Guillaume Lobet. Combining cross-section images and modeling tools to create high-resolution root system hydraulic atlases in *Zea mays*. Plant Direct 2021.07.16;e00290

ABSTRACT

Root hydraulic properties play a central role in the global water cycle, in agricultural systems productivity, and in ecosystem survival as they impact the canopy water supply. However, the existing experimental methods to quantify root hydraulic conductivities, such as the root pressure probing, are particularly challenging, and their applicability to thin roots and small root segments is limited. Therefore, there is a gap in methods enabling easy estimations of root hydraulic conductivities in diverse root types. Here, we present a new pipeline to quickly estimate root hydraulic conductivities across different root types, at high resolution along root axes. Shortly, free-hand root cross-sections were used to extract a selected number of key anatomical traits. We used these traits to parameterize the Generator of Root Anatomy in R (GRANAR) model to simulate root anatomical networks. Finally, we used these generated anatomical networks within the Model of Explicit Cross-section Hydraulic Anatomy (MECHA) to compute an estimation of the root axial and radial hydraulic conductivities (K_x and k_r, respectively). Using this combination of anatomical data and computational models, we were able to create a root hydraulic conductivity atlas at the root system level, for 14-day-old

pot-grown *Zea mays* (maize) plants of the var. *B73*. The altas highlights the significant functional variations along and between different root types. For instance, predicted variations of radial conductivity along the root axis were strongly dependent on the maturation stage of hydrophobic barriers. The same was also true for the maturation rates of the meta-xylem vessels. Differences in anatomical traits along and across root types generated substantial variations in radial and axial conductivities estimated with our novel approach. Our methodological pipeline combines anatomical data and computational models to turn root cross-section images into a detailed hydraulic atlas. It is an inexpensive, fast, and easily applicable investigation tool for root hydraulics that complements existing complex experimental methods. It opens the way to high-throughput studies on the functional importance of root types in plant hydraulics, especially if combined with novel phenotyping techniques such as laser ablation tomography.

3.1 Introduction

Root hydraulic properties are part of the major functional plant properties influencing root water uptake dynamics. Among them, the radial hydraulic conductivity (k_r) is a key component of the water absorption from the soil to the vasculature of the plant, and the axial hydraulic conductance (K_x) defines the water transport along the root (Leitner et al., 2014). Changes in the local root hydraulic properties, at the cell and organ-scale, are known to have overall repercussions on the plant hydraulic behavior (Meunier et al., 2020; Tardieu et al., 2018) and are considered as important breeding targets to create drought resilient varieties (Maurel, and Nacry, 2020). Quantitative root hydraulic conductivity data along roots are therefore needed for a thorough understanding of root water uptake dynamics.

The root axial conductivity (K_x) is a function of the xylem vessel area, maturation, and number (Martre et al., 2001; Sanderson et al., 1988). It can be approximated using Poiseuille–Hagen's law applied to xylem vessels area (Frensch, and Steudle, 1989) or measured directly using a pressure probe attached to a root segment with cut ends (Meunier et al., 2018b).

The root radial conductivity (k_r) is influenced by different root anatomical traits and subcellular hydraulic properties. On the one hand, root anatomical traits define the baseline for the root radial conductivity as they delineate the structure of the network of root cells (Steudle, 2000). Rieger, and Litvin (1999) showed that the radial

conductivity is inversely related to the root radius and cortex width. Similarly, increasing the number of cell layers in the cortex (Chimungu et al., 2014b), the size of cortex cells (Chimungu et al., 2014a; Lynch et al., 2014), as well as the presence of aerenchyma (Fan et al., 2007) all seem to lower the radial hydraulic conductivity. On the other hand, the subcellular hydraulic properties, such as the contribution of aquaporins to the hydraulic conductivity of plasma membranes, can modulate the root radial conductivity (Javot, and Maurel, 2002; Parent et al., 2009) on the short term. The hydraulic conductance of plasmodesmata may also have a crucial impact, especially after the deposition of suberin lamellae locally blocking the transmembrane pathway (Couvreur et al., 2018). The development of such hydrophobic barriers (e.g., the lignified Casparian strip and suberin lamellae in cell walls of the endodermis and exodermis) drastically reduces the root radial conductivity on the long term (Enstone et al., 2002). The quantification of the radial hydraulic conductivity is challenging due to the complexity of the associated experimental procedures. It is even more complicated to assess it at different locations along the root axis and on different root types. The most direct way to estimate root radial conductivity is on roots grown in soil-less environments using a root pressure probe (Frensch, and Steudle, 1989). Other experimental techniques employ a pressure chamber to measure water flow through roots that were successively cut into smaller parts (Zwieniecki et al., 2002), or employ the high pressure flow meter device on whole root systems (Tyree et al., 1994). From a different perspective, modeling tools may connect the dots between complementary data available, possibly at different scales, to assist the estimation of root radial conductivity (Passot et al., 2019). In Heymans et al. (2020), we used this approach to connect root anatomical with cell hydraulic data using the root anatomy and hydraulic anatomy simulators GRANAR and MECHA. At larger scale, Zarebanadkouki et al. (2016) connected the root hydraulic architecture model of Doussan et al. (1998a) to water tracer data using an inverse modeling method to derive profiles of hydraulic conductivity along roots.

Such estimations are so complex that many studies that simulate water uptake with functional–structural root models still rely on the root hydraulic conductivity profiles estimated more than 20 years ago by (Doussan et al., 1998b) (e.g., R-SWMS, Javaux et al., 2008; OpenSimRoot, Postma et al., 2017; or MARSHAL, Meunier et al., 2020). Today, we need new methods to rapidly quantify root hydraulic conductivities from more easily available data.

Here, we present a procedure to generate a high-resolution hydraulic conductivity atlas from experimental data combined to recent modeling tools. In short, with free-hand root cross-sections and fluorescent microscopy, we were able to extract easily anatomical traits that can be used to run the Generator of Root Anatomy in R (GRANAR). Then, using the generated hydraulic anatomical networks with MECHA, we estimated the k_r and K_x along the root axis of each maize root type. The coupling of these models to multiple root cross-section images creates a new way to generate a root hydraulic conductivity atlas that takes into account the impact of anatomical traits, the development of hydrophobic barriers and the cell hydraulic properties. The method that we developed is cheap, reproducible and adaptable to different environments than the one tested in this study.

3.2 Material and methods

3.2.1 Plant materials and growth condition

Five *Zea mays* (maize cultivar *B73*) plants were grown in pots for 14 days. The PVC pot dimensions were 12 cm diameter, 25 cm deep, and filled with two soil layers for a total volume of 2 L after saturated watering. The bottom soil layer was composed of 1.5 kg per pot of potting soil (80% sieved potting soil DCM [Grobbendonk, Belgium]: 20% sand) and the superficial soil layer was made of 1 kg per pot of sandy soil (50% sieved potting soil DCM [Grobbendonk, Belgium]: 50% sand). The soil drained for two days when the germinated seeds were planted and not rewatered afterwards. The seeds were placed at 1 cm deep in the first soil layer. The germination of the seeds occurred in a Petri dish maintained vertically in dark conditions between two wet filter papers. Ahead, the seeds were initially sterilized in a 50% bleach bath for 5 min then rinsed in water five times, interrupted by the sponging of the rinsing water. From the 15 seeds that were put under germination, five were selected based on the length of the tap root (0.5 to 1 cm long) in order to have a homogeneous root growth. Each seed was planted in a different pot column. The pots were separated from each other over a grid pattern, where the cells are 20 cm long and 13 cm width with a total of 5 rows and 10 columns. The other pots that composed this experimental design were occupied by other maize genotypes following the same growth condition. All plants were grown in a greenhouse (Louvain-la-Neuve, Belgium, May 2018) with the environmental settings of the greenhouse set to 60% for the relative humidity and a temperature of $25°C$ ($\pm 3°C$).

3.2.2 Processing root cross-sections

After 14 days of growth in the pots, the root systems were excavated and carefully washed. The root systems were scanned on a flatbed scanner (Medion 3600 DPI) customized in-house in such a way that the light source and the sensor are positioned on both sides of a large water container (21 x 60 x 4 cm). Root samples were conserved in a FAA (95% ethanol : glacial acetic acid : 37% formaldehyde : water; 50:5:10:35) (Ruzin et al., 1999) and kept at 4^oC. Before staining the roots, they were rinsed in tap water for 15 min. The roots were stained with 1% (w/v) berberine hemi-sulphate for 1 h and post-stained with 0.5% (w/v) aniline blue for 30 min before making free-hand root cross-sections following the Brundrett et al. (1988) protocol. Three or more free-hand root cross-sections per root type were taken on at least three different roots at every 5 cm or less to create an atlas of anatomical traits along each root type. Cross-section images were acquired with a Leitz SM-LUX (Germany) fluorescent microscope equipped with a Leica camera DFC320 (Cambridge, United Kingdom).

3.2.3 Root typology

The root types selected for this analysis are the taproot, the basal roots (embryonic roots), the shoot-born roots on the first node and two types of lateral roots, the short ones and long ones (longer than 5 cm with second order lateral roots on it) (Passot et al., 2018). Because we were able to measure lateral root lengths but not their growth rates, we chose to have two classes of lateral roots instead of the three types characterized by Passot et al. (2018). We had to base the classification on root length instead of root growth rate. After a few days of growth, the length of individual lateral roots clearly discriminates between longer roots classified as a type A by Passot et al. (2018) and the other two lateral types (B and C) that are shorter than the A type after a couple of days.

3.2.4 Root image analysis

From root cross-section image to root anatomical traits

The images were analyzed with the ImageJ (version 1.47) software (Schneider et al., 2012). The anatomical traits that we measured manually are listed in Table 3.1. On each root cross-section image, transects were drawn from one side to the other passing by the center, or two transects from two distinct side meeting in the center if the

image did not cover the entire root cross-section. The selection of the transects was also made in order to have the most intact cells crossing the lines. With the segmented "line" tools of ImageJ, those lines were followed to measure the tissue width of the epidermis, the exodermis, the cortex, the endodermis, and pericycle cell layer, as well as the stele diameter. Following the same lines, the numbers of cells in the cortex and in the stele were counted. The specific cell diameter of the cortex and the stele was calculated by dividing the width of the root tissue by the number of cell layers within the root tissue. The meta-xylem vessels' diameters were calculated from the surface area of all meta-xylem vessels divided by their number. The surface area was measured with the polygon tool of ImageJ. The number of proto-xylem vessels was counted by addition of all lignify cells in the surroundings of meta-xylem vessels. The staining procedure to spot the lignified cell walls is described in the sub-section 3.2.4. An overview of the anatomical traits measurement protocol can be found in the Appendix 3.7.

Table 3.1: List of the measured anatomical traits acquired with ImageJ on the root cross-section images that have been used to get the GRANAR parameters

	Measured traits on the root	**GRANAR parameters**		
Traits	**Description from traits to parameter**	**Tissue type**	**Properties**	**Unit**
EpW	Epidermis cell radial width	*epidemis*	*cell_diameter*	μm
ExW	Exodermis cell radial width	*exodermis*	*cell_diameter*	μm
nCF	Number of cortex cell layer	*cortex*	*n_layer*	#
CoW	Cortex width (CoW) divided by nCF	*cortex*	*cell_diameter*	μm
EnW	Endodermis cell radial width	*endodermis*	*cell_diameter*	μm
PeW	Pericycle cell radial width	*pericycle*	*cell_diameter*	μm
SD	Global stele diameter	*stele*	*layer_diameter*	
nS	SD divided by the number of			
SW	stele cells on the stele diameter (nS)	*stele*	*cell_diameter*	μm
MXA	Meta-xylem area	*xylem*	*max_size*	μm
nMX	Number of meta-xylem vessel	*xylem*	*n_files*	#
nPX	number of proto-xylem vessel divided by nMX	*xylem*	*ratio*	-

From anatomical traits to root cell network generation

We needed to capture anatomical descriptors that are ready-to-use for downstream computational models to create a series of functions that represent the evolution of the hydraulic conductivities as a function to the distance from the root tip. Therefore, such root hydraulic conductivity atlas along the different maize root types would take into account the development of the anatomical traits. With the gathered root cross-section images, and the extracted root anatomical traits measured along the roots axes, we computed linear regressions of the different anatomical traits against the distance to the tip for each root type. The coefficients of the linear models were used to estimate the different GRANAR input parameters along the root type axes at every wanted location (the spatial resolution is described below). However, if the regression between the distance along the root and the anatomical traits did not significantly differ from the uniform model (p value $> .05$), the average value of the anatomical traits along the root axis was taken instead of the value predicted by the linear model.

An exception was made for the relation between the size of the stele and the one of the meta-xylem. Instead of the regular regression methods to obtain the coefficients of the linear models, a Napierian logarithmic transformation was applied on the stele area and the xylem area, similarly as in Yang et al. (2019). The linear regression of the Napierian logarithm between those anatomical traits was used to set the meta-xylem diameter parameter (GRANAR parameter: xylem *max_size*). The goal was to conserve the relationship between the size of the stele and that of the meta-xylem. Nevertheless, the regular regression method was still used to set the number of meta-xylem vessels (GRANAR parameter: xylem *n_files*).

The chosen distances between the simulated root cross-sections used to generate the atlas vary along three regions of the root. From 0 to 2 cm from the tip, the spatial resolution is 0.5 cm. From 2 to 15 cm from the tip, we selected a resolution of one cross-section every centimeter, and between 15 and 40 cm from the tip, one every 5 cm. The number of technical replicates for each simulated root cross-section is two, with small artificial stochasticity (GRANAR parameter randomness set to 1). This artificial stochasticity produces a small random shift in the center of every cell proportional to the distance from the center of the generated root cross-section. We tested the generated root cross-sections to validate that their simulated anatomical traits match the set of experimental values for those anatomies (Figure 3.2).

Estimation of k_r and K_x from generated root cell network

Radial and axial hydraulic conductivities (k_r and K_x) were then estimated for each simulated anatomical network along the selected root types using MECHA and with the maize cell hydraulic parameters described in the section below. To test the effect of the distance from the apex and the factor root type, each hydrophobic barrier scenario or xylem maturation was computed for every generated root cross-section. To identify the type of hydrophobic barriers that were encountered on the cross-section images, we used the berberine-aniline blue fluorescent staining procedures for suberin, lignin, and callose in plant tissue (Brundrett et al., 1988). This procedure was designed to highlight exodermal and endodermal Casparian strips and suberin lamellae, it also works to identify the lignification of the xylem cell walls. Meta-xylem vessels with fully lignified cell walls were considered as mature vessels.

3.2.5 Description of MECHA hydraulic parameters

The simulation framework MECHA (Couvreur et al., 2018) can estimate root radial conductivities from the root anatomy generated with GRANAR from the subcellular-scale hydraulic properties of cell walls, membranes, and plasmodesmata. The cell wall hydraulic conductivity was set to $2.8\,10^{-9} m^2 s^{-1} MPa^{-1}$, as measured by Zhu, and Steudle (1991) in maize. Lignified and suberized wall segments in the endodermis and exodermis were considered hydrophobic and attributed null hydraulic conductivities. The protoplast permeability (L_{pc}, $7.7\,10^{-7} m.s^{-1} MPa^{-1}$) measured by Ehlert et al. (2009) was partitioned into its three components: the plasma membrane intrinsic hydraulic conductivity (k_m), the contribution of aquaporins to the plasma membrane hydraulic conductivity (k_{AQP}), and the conductance of plasmodesmata per unit membrane surface (K_{PD}). The latter parameter was estimated as $2.4\,10^{-7} m.s^{-1} MPa^{-1}$ (Couvreur et al., 2018), based on plasmodesmata frequency data from Ma, and Peterson (2001), and the plasmodesmata conductance estimated by Bret-Harte, and Silk (1994). By blocking aquaporins with an acid-load treatment, Ehlert et al. (2009) measured a k_{AQP} of $5.0\,10^{-7} m.s^{-1} MPa^{-1}$. The remaining value of k_m after subtraction of k_{AQP} and K_{PD} from L_{pc} was $0.3\,10^{-7} m.s^{-1} MPa^{-1}$. Each value of k_m, k_{AQP}, k_{PD}, and L_{pc} was set uniform across tissue types. For details on the computation of k_r, see Couvreur et al. (2018).

The specific root axial hydraulic conductance $K_x (m^4 s^{-1} MPa^{-1})$

is the sum of specific conductances of individual vessels, estimated using the Hagen–Poiseuille equation:

$$K_x = \sum_{i=1}^{N} \frac{\pi r_i^4}{8\eta} \tag{3.1}$$

where A (m^4) is the transverse area of one xylem vessel, i is the xylem vessel number, N is the total number of xylem vessels in parallel within a cross-section, and η ($MPa.s$) is the dynamic viscosity of the xylem sap. Xylem sap being essentially water, η was assumed equal to $10^{-9} MPa.s$.

3.2.6 Root hydraulic conductivities benchmark

As the root hydraulic conductivities obtained in this study are compared, among other studies, with the ones estimated in Doussan et al. (1998b), which refer to lateral root segment ages, we assumed that the lateral roots have an average growth rate of 1 cm per day (Passot et al., 2018) to turn root segment ages into distances from the apex.

The details about the GRANAR-MECHA coupling are available in an online Jupyter NoteBook (https://mybinder.org/v2/gh/HeymansAdrien/GranarMecha/main). The complete procedure can be run online or locally after downloading the related gitHub repository (https://github.com/HeymansAdrien/GranarMecha doi: https://doi.org/10.5281/zenodo.4316762). This complementary open-source tool helps the users to change anatomical traits and cell hydraulic properties to personalize the exercise at will. The outputs of each generated root cross-section can be visualized through different figures that show the proportion of the water fluxes in each compartment (apoplastic and symplastic fluxes) and a table with the estimated k_r and K_x for all maturation scenarios.

The whole script that was used to compute the root hydraulic atlas from the root anatomical measurement is presented as a Rmarkdown script stored in a GitHub repository (https://github.com/granar/B73_HydraulicMap doi: https://doi.org/10.5281/zenodo.4320861). All input and output data of this study are stored in the same repository.

3.2.7 Statistical analysis

The statistical analysis was conducted using R software (version 3.5.1, R Core Team, 2018). The R package that was used for the data manipulation was tidyverse (Wickham, and Chang, 2019). All analyses of variance (ANOVAs) were conducted considering the full length of the roots (not restricted to the actual intervals where the roots show the features). The combination of distance from the apex and the factor root type was included in the performed two-way ANOVAs. The function *'aov'* from the package stats was used for this purpose. Using these generalized linear models and the *'emtrends'* function from the package *"emmeans"* (Lenth et al., 2018), we were able to compare pairwise the change of the anatomical traits along their root type axes. Those tests were used to seek anatomical traits changes along root type axes. Other ANOVAs, used to parameterize GRANAR and benchmark the anatomical input with the output from the cross-section generation procedure, were performed using the same function, but the dataset was split per root type factor, and the distance from the apex was the explicative variable. The Pearson correlation coefficients used in the comparison between the GRANAR output and the theoretical values from the input parameter were computed with the function *'ggpairs'* from the package *"GGally"* (Emerson et al., 2013).

3.3 Results

3.3.1 Changes in anatomical traits

The first step of the procedure to create a root hydraulic atlas is to understand the change of anatomical traits along the different root type axes. The root cross-section images gathered along the different root types show that some anatomical traits change along the root axis (Table 3.2). In general, the axial roots (Tap-, Basal-, and shoot-born-roots) are narrower at their tip than at their base. It is primarily due to a shrinkage of the stele (Figure 3.2). This shrinkage is linked to a smaller stele cell number. Only the long laterals do not present a significant decrease ($p < .05$). However, basal- and shoot-born roots also have smaller diameter closer to the tip ($p < .05$). The change in the stele diameter also differs across root types. The change of stele diameter along the root axes for the shoot-born roots is steeper than for the tap root ($p < .05$). The cortex width tends to be wider as we move away from the tip of the root. The change of cortex width along the root axis is also different between the long lateral and the basal-

and shoot-born roots ($p < .05$).

Table 3.2: *P* value of the two-way analysis of variance (ANOVA) models performed to test the hypothesis under which the cell tissue types are influenced by the distance from the apex and the root type

Anatomical traits	**Apex distance**	**Root type**	**Dist. ⋆ Type**
	***p* value**	***p* value**	***p* value**
Epidermis width (μm)	.01537	.00542	.04410
Exodermis width (μm)	.00281	$7.31e^{-10}$	.42145
Cortex width (μm)	$4.11e^{-7}$	$< 2e^{-16}$	.00109
Cortex cell width (μm)	$1.50e^{-7}$	$2.94e^{-14}$	.033
Endodermis width (μm)	$2.38e^{-13}$	$1.37e^{-5}$	.912
Pericycle width (μm)	.000979	$< 2e^{-16}$	.000519
Stele diameter (μm)	$6.16e^{-16}$	$< 2e^{-16}$	$1.07e^{-8}$
Stele cell width (μm)	$< 2e^{-16}$	$< 2e^{-16}$	.276
Stele cell number (#)	$5.56e^{-9}$	$< 2e^{-16}$	$6.85e^{-5}$
Meta-xylem number (#)	$< 2e^{-16}$	$< 2e^{-16}$	.475
Meta-xylem vessel diam. (μm)	.030735	$< 2e^{-16}$	.000502
Proto-xylem number (#)	$6.21e^{-15}$	$< 2e^{-16}$	.0493

Closer to the tip, as the stele area decreases, the number of xylem vessels is also reduced, whereas the size of the meta-xylem vessels does not shrink significantly for most root types ($p > .05$). The relation between the stele and xylem areas is strong ($R^2 = .975$), but it is not linear. However, when we look at the Napierian logarithm of those areas, similarly as in Yang et al. (2019), the linearity of this relationship is strong ($R^2 = .991$, Figure 3.2). Due to the strong relationship between those anatomical traits, we used the Napierian relationship between the size of the stele and the meta-xylem vessels into the GRANAR parameterization procedures instead of using the regular linear regression.

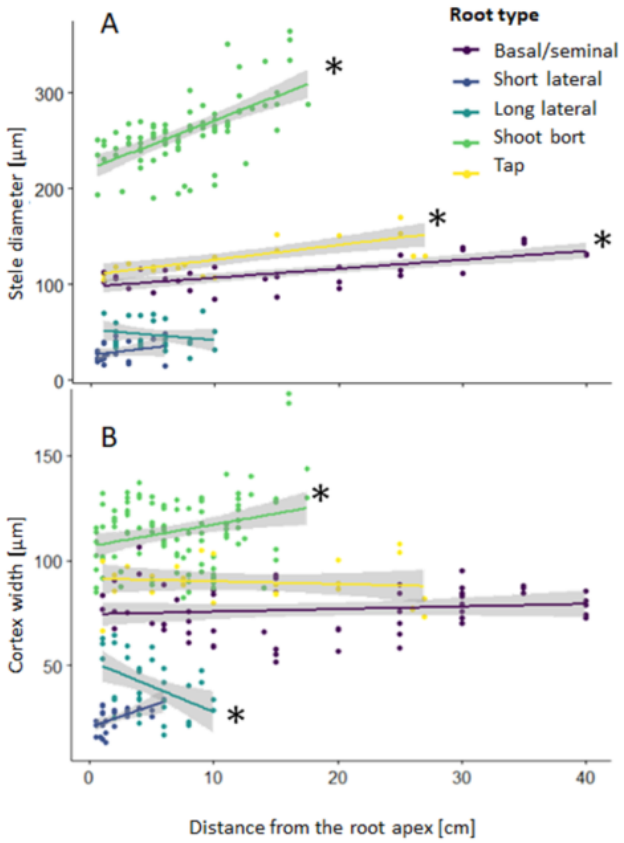


Figure 3.1: Relation between the distance from the apex and (a) the stele diameter, and (b) the cortex width for the different root types. Data shows all experimental measures for the dedicated anatomical traits. The dark shadings show the 95% interval of confidence around the linear regression for each root type. ($\star$): slope different than 0 ($p < .05$; generalized linear model: the anatomical layer width as a function of the distance, the root type and the combination of both)

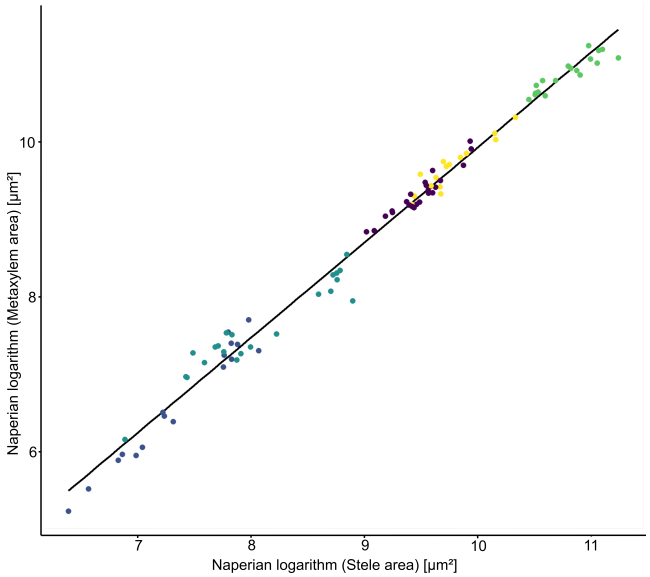


Figure 3.2: Allometric relationship between the Napierian logarithm of the meta-xylem area and the one of the stele area. Data shows experimental averages per root cross-section image. $R^2 = .991$

3.3.2 Building an atlas of root anatomies and hydrophobic barriers

Each input parameter for the model GRANAR is a function depending on the root type and the distance from its apex. With such information, we were able to simulate representative root cross-sections along each root type, at any longitudinal position (Figure 3.3).

In addition to the overview of the root cross-section of the root system, we added the location of hydrophobic barriers and meta-xylem maturation zone based on staining signals (Figure 3.4). The berberine-aniline blue fluorescent staining procedure for suberin, lignin, and callose allowed us to estimate the position of the different maturation zones (Figure 3.5). On the main root axes, the taproot, the basal-, and the shoot-born roots had a fully suberized endodermis before the maturation of the meta-xylem. In addition, the lignification of the meta-xylem vessels usually occurred shortly after the complete suberization of the endodermis. On the opposite, in lateral roots, the meta-xylem vessels were lignified before the complete suberization

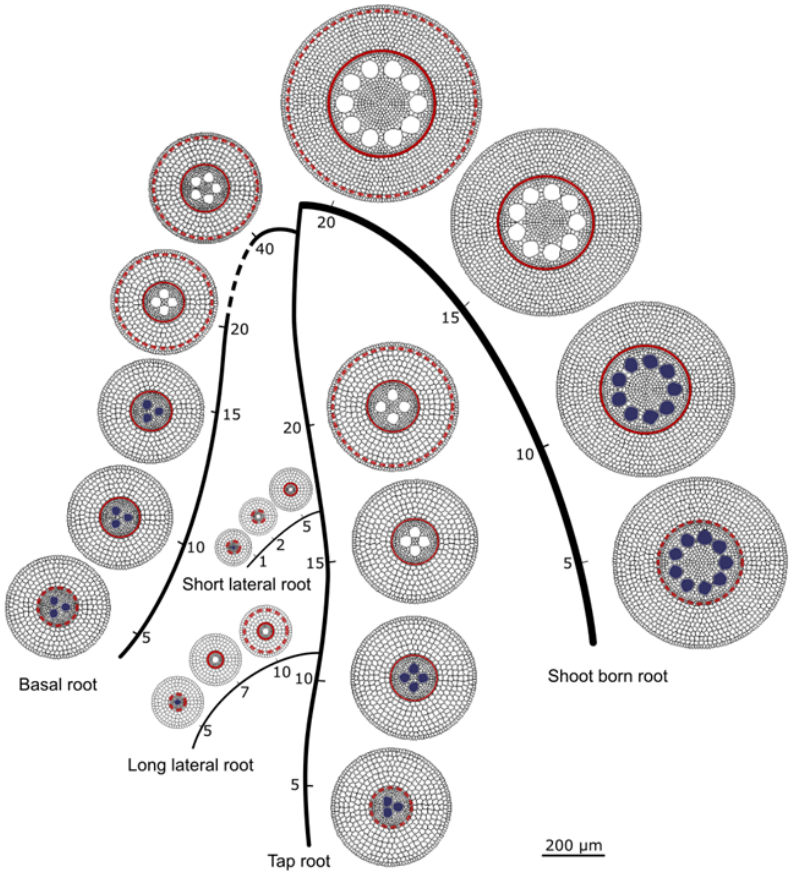


Figure 3.3: Schematic representation of a maize root system with five root types. Along each root type, the generated representative root cross-sections pair with the nearby tick marks. The numbers along the roots describe the distance from the tip of the root in centimeters. The 200-μm bar stands for the displayed root cross-sections, though the scale is free in between in the rest of the figure. The filled meta-xylem vessels are not mature yet. The dashed red circles stand for the Casparian strip. The continuous red circles stand for the fully suberized endodermis

of the endodermis. Moreover, short lateral roots had lignified meta-xylem vessels before the suberin lamellae started to deposit on the cell walls of the endodermis. For long lateral roots, lignified meta-xylem vessels were found where some suberin had started to deposit as a lamellae against primary walls of the endodermis.

The time needed to generate root cross-sections with GRANAR was around 1 to 20 s depending on the number of cells on the anatomical network.

3.3.3 Building an atlas of root hydraulic conductivities

The next step of the process to make high-resolution atlases for the root hydraulic conductivity is to estimate the k_r and K_x of all the generated cross-sections. To estimate the k_r of the generated root cross-section, we used the MECHA model (Figure 3.6).

We adjusted the maturation scenario in MECHA to fit our experimental data of the maturation zone for the hydrophobic barriers and meta-xylem lignification. The cell hydraulic parameters were kept the same for all cross-sections. For the K_x, we used the Hagen–Poiseuille laws (Equations 1.6).

For each hydrophobic scenario, the radial hydraulic conductivity was significantly influenced by the distance from the apex, the root type factor, and the combination of both (Table 3.2). The axial hydraulic conductance, with only protoxylem or with all functioning xylem vessels, was also highly dependent on the distance from the apex, the root type factor, and the combination of both (Table 3.2).

To estimate the k_r for the three scenarios, the model MECHA took around less than 1 to 5 min per root cross-section.

3.4 Discussion

We presented here a protocol to estimate root hydraulic properties that could be repeated in further studies (e.g., with different species, genotypes, or environment). Our method is quicker than root pressure probing (the established experimental procedure) to estimate the root radial conductivity of a root segment (Figure 2.4). This increase in throughput enabled the estimation of k_r on more root cross-sections per experiment. In addition, as root traits can be interpolated along the root axis, hydraulic atlases with high spatial resolution can be created. It takes a total time of 30 min, on average, to link anatomical traits with hydraulic properties. This includes

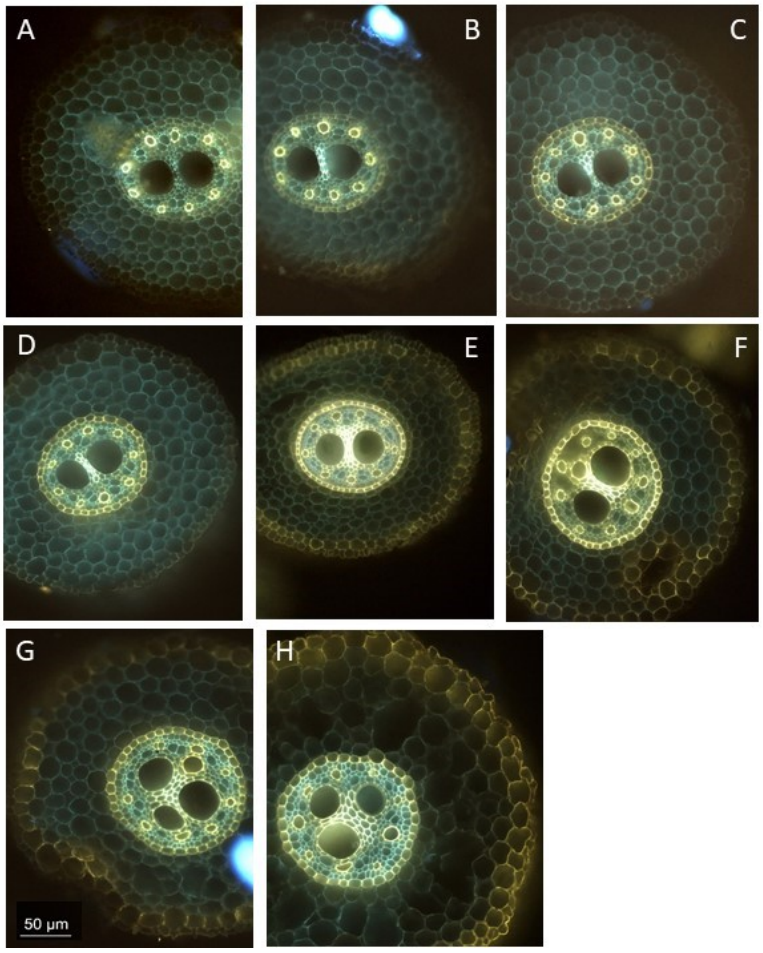


Figure 3.4: Basal root cross-sections. (a) 3 cm from the apex, the arrow point at the endodermal Casparian strip ("*ecs*"); (b) 5 cm from the apex; (c) 8 cm from the apex, the arrow point at the suberin lamellae that deposited on the endodermis ("*sl*"); (d) 10 cm from the apex; (e) 15 cm from the apex, the "*mmx*" arrow points the lignify cell walls of the mature meta-xylem vessels, the "*excs*" arrow points the exodermal Casparian strip; (f) 20 cm from the apex; (g) 25 cm from the apex; and (h) 30 cm from the apex. Bar = 50 μm

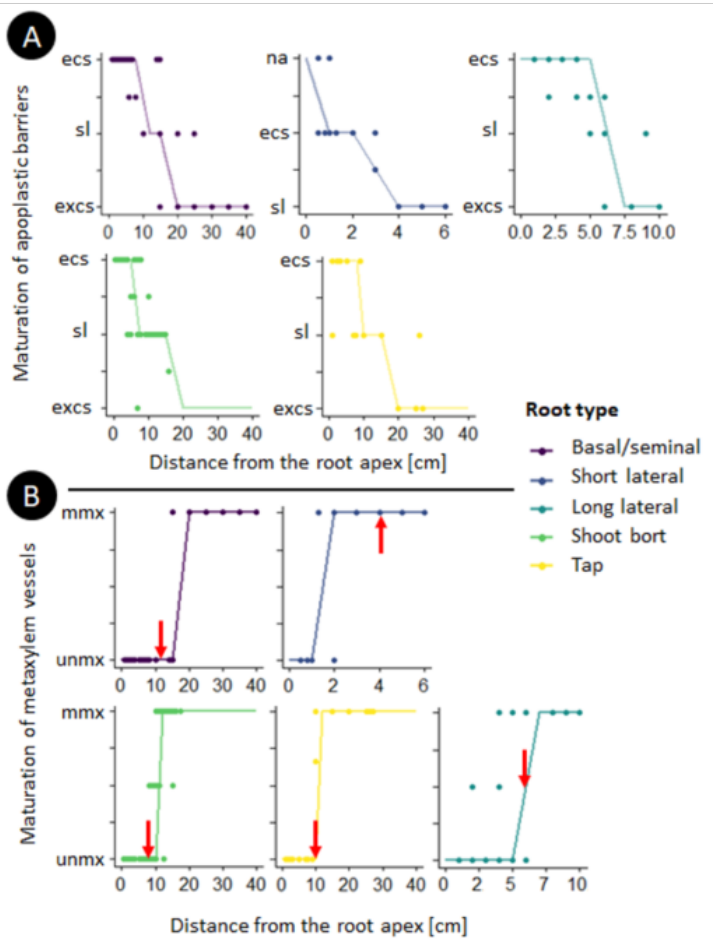


Figure 3.5: Development of the maturation for hydrophobic barriers (a) and for the meta-xylem vessels (b) along the root axis for the different root types. Half values were applied when the transition between two maturation stages was observed. The lines are a discretization of the local weighted regressions of the scatter plots. (a) "na"=no hydrophobic barriers; "*ecs*"=endodermal Casparian strip; "*sl*"=fully suberized endodermis; "*excs*"=suberized endodermis and exodermal Casparian strip. (b) "*unmx*"=only the protoxylem vessels are lignified; "*mmx*"=all xylem vessels are lignified. The arrows point out where the endodermis is fully suberized for the specific root type

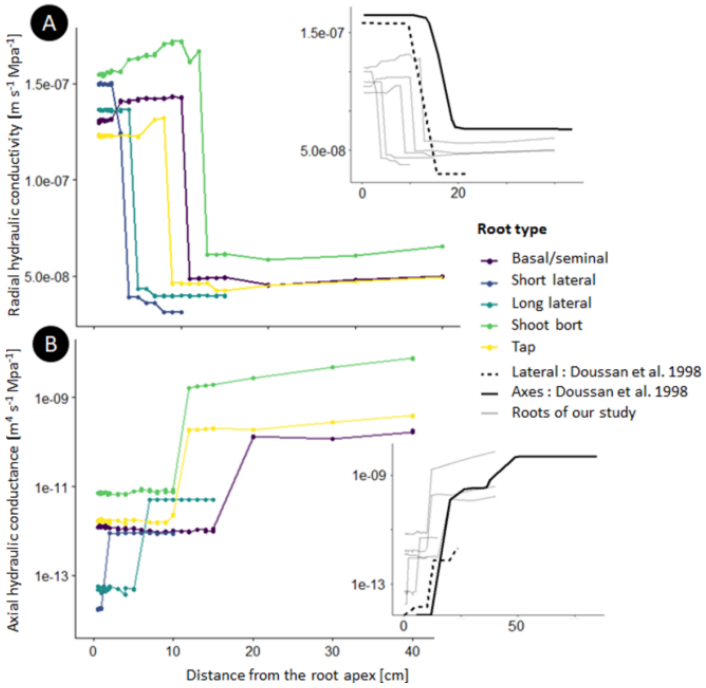


Figure 3.6: Hydraulic conductivity atlas along the different root types. (a) Estimation of the k_r for each generated root cross-section along the different root. The side panel shows the two Doussan et al. (1998b) estimations for k_r and our estimations in comparison. (b) Estimation of the axial hydraulic conductance for each generated root cross-section along the different root. The side panel shows the two Doussan et al. (1998b) estimations for K_x and our estimations in comparison.

the free-hand cross-sections, the extraction of anatomical traits with ImageJ, the generation of root anatomical networks with GRANAR, and the estimation of three hydraulic scenarios with three different types of hydrophobic barriers. On the contrary, one estimation for the radial hydraulic conductivity from the root pressure probe takes at least 3 to 5 h, as steady root pressure has to be established after the connection between the root and the device (Li et al., 2009). In both cases, making free-hand root cross-section takes around 10 to 20 min and is mandatory to link anatomical traits with hydraulic properties. One should keep in mind that the experimental procedure is likely to be more accurate, illustrating the usual tradeoff between precision and throughput.

Meunier et al. (2020) showed that modifying hydraulic properties changes the root system hydraulic architecture and thus affects the whole root system conductance (K_{rs}). Tuning root hydraulic conductivity functions to match experimental data or test new hypotheses through simulation studies could therefore show the local impact of root anatomy or cell hydraulic properties on the whole root system conductance. A better understanding of the effect of local root traits on the global hydraulic behavior of the root system would enhance the breeding efforts towards more drought tolerant cultivars.

We expect our analysis pipeline will be of particular interest with new techniques such as the Laser Ablation Tomography (Strock et al., 2019) and root traits recognition algorithm (Sosa et al., 2014). Those techniques could drastically increase the number of root cross-section images that can be taken on an experiment and the deep learning approach can speed up the process of root traits extraction procedure from those images. These are two limiting aspects in perspective of further improvements of the estimation of radial hydraulic conductivities along roots.

In comparison with the hydraulic conductivity atlas of (Doussan et al., 1998b), our data, for the different root types, show a drop in radial conductivity closer to the tip. Our result is close to the one of Zarebanadkouki et al. (2016), who estimated that the first drop of k_r occurred after four centimeters within the stepwise function with three transition zones due to the development of hydrophobic barriers. This early drop is due to the deposition of suberin lamellae in endodermal cell walls, which has been shown to be sensitive to environmental conditions (Tylová et al., 2017), so variability in its position along the root can be expected. The proportionally smaller second drop due to the addition of the exodermal Casparian strip is compensated further away by the expansion of the stele and larger number of xylem vessels. Those anatomical effects on the radial conductivity follow the same trends as in Heymans et al. (2020). In our study, the estimated radial conductivities are within the range of Doussan et al. (1998b), and in a slightly higher range relative to the estimations of Zarebanadkouki et al. (2016) and Meunier et al. (2018b).

The use of the Hagen–Poiseuille equations to estimate the K_x is straightforward when the area of each xylem vessel is known. Our predicted range and trends both match direct measurements by Meunier et al. (2018b) and estimations from Doussan et al. (1998b). Uncertainties related to the application of the Hagen–Poiseuille law have been discussed in the literature. Frensch, and Steudle (1989)

have shown that it may overestimate experimental K_x values by a factor of two to five. This could be due to the presence of perforation plates (Brodersen et al., 2018; Shane et al., 2000) or persistent xylem cross-walls (Sanderson et al., 1988). In this study, we did not divide the estimated K_x by a coefficient. The uncertainty of identification of mature xylem vessels by the used staining procedure could shift the transition zone shootward. Other staining procedures could lift those uncertainties, such as the one with the Fluorol yellow 088 (synonyms: 2,8-dimethylnaphtho[3,2,1-kl] xanthene; Solvent Green 4, CAS 81-37-8) and PEG 400 (PEG 400:glycerol:water = 10:9:1, v:v) allow intense staining of lipids and suberin lamellae (Kitin et al., 2020). We also assume that xylem sap has the same viscosity as water. This hypothesis could be discussed in relation to xylem sap temperature or solute concentration (Bruno, and Sparapano, 2007).

The hydraulic conductivity atlas that we computed for this genotype in this precise environmental condition (*Zea mays* var. *B73* in pots) is an example case. Our methodology allows the inclusion of the effect of root anatomical changes, the development of the hydrophobic barriers, and takes into account the selected cell hydraulic properties summarized in Section 3.2.5. This study is the first to our knowledge to propose a method to characterize a root hydraulic conductivity atlas with such a high spatial resolution along roots and across five different root types. We posit our approach will allow more realistic parameterizations of functional–structural plant models targeting root water uptake. Such a root hydraulic conductivity atlas can as well be connected to complementary modeling tools (e.g., Meunier et al., 2020) to estimate hydraulic parameters such as the root system conductance or the standard sink fraction for models working at larger scales (e.g., Agee et al., 2021; Cai et al., 2018; Sulis et al., 2019, as envisioned by Passot et al., 2019). Future modeling studies could reuse the anatomical networks and the root hydraulic conductivities that we built on their root system architecture. This modeling framework could as well be used inversely, to search for subcellular hydraulic conductivities that reproduce measured hydraulic properties at the root scale, as in Ding et al. (2020), or at the plant scale.

3.5 Conclusion

In this study, we showed how to use stained root cross-section images and computational tools (organ-scale root models: GRANAR and MECHA) to create a high-resolution hydraulic atlas of a maize root system (*Zea mays* var. *B73* in our example). Our hydraulic atlas includes hydraulic information (radial and axial properties) and anatomical data along five root types (taproot, basal, shoot-born, long laterals, and short laterals).

Anatomical differences along the root axes and between root types have an impact on the radial and axial hydraulic properties of the roots. The values and trends shown in this study are within the same range as the estimations that can be found in the literature.

Compared with measures from root pressure probing, our method has the advantages of being quick and produces high-resolution results on any type of root. We expect our new methodology to be of great use for further root hydraulic studies as it streamlines the estimation of local root hydraulic properties from experimental data. These local root conductivities can be used in functional–structural root models to estimate macroscopic hydraulic properties. It opens the way to test or benchmark the local impact of local root traits on the global hydraulic behavior of a root system.

3.6 Appendix

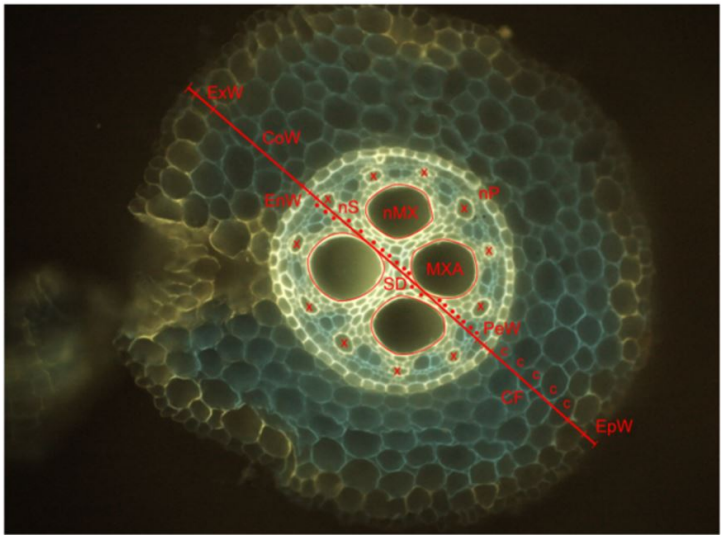


Figure 3.7: Overview of a maize basal root cross-section associated with the measures taken with ImageJ to parameterize GRANAR. From left to right: ExW = exodermis width, CoW = cortex width, EnW = endodermis width, nS = number of stele cells along the transect, nMX = number of meta-xylem vessels, SD = stele diameter, MXA = all meta-xylem area, nP = number of proto-xylem vessels, PeW = pericycle width, CF = number of cortex layers, EpW = epidemis width. The main transect was aligned where the cells were the most intact across the root cross-section.

In the previous Chapter, we presented a new method to create root hydraulic atlases of root system from a combination of root cross-section images and modeling tools. However, during such process we kept the subcellular hydraulic properties constant.

We figured out that if we wanted to include these hydraulic properties, we needed a better understanding of how they influence the root radial hydraulic conductivities in combination with the root anatomy. In addition, we wanted to decrease the computational time that was going to be an issue if we wanted to estimate thousands of root radial hydraulic conductivities. We already had in mind that at one point we would generate thousands of root systems with different root hydraulic functions.

Thus, this next Chapter prepares the computational tools that we required to estimate the root radial hydraulic conductivities of thousands of roots. In addition, we took advantage of this new computational tool to check the proportional influence of anatomical traits and subcellular hydraulic properties on the radial hydraulic conductivity.

A BETTER UNDERSTANDING OF THE HYDRAULIC ANATOMY OF MAIZE ROOTS

4

This chapter is the edited version of a scientific article in preparation, entitle as:

> Adrien Heymans, Valentin Couvreur, Clément Saint-Cast, and Guillaume Lobet. *In silico* analysis of the influence of maize (*Zea may*) root hydraulic anatomy. (in progress)

ABSTRACT

In the soil, roots are the entry point of the water into the plant. They are, however, not necessarily efficient to let the water flow through them. This is highly dependent on their hydraulic anatomy which can be very diverse. This diversity of traits is visible between species and even between varieties. Over a relatively short period of time, plants can regulate their subcellular hydraulic properties. While over a longer period of time, they can adapt their anatomy as well as the deposition of hydrophobic barriers. These adaptations occur either in response to developmental or environmental factors. Such changes in the hydraulic anatomy have potentially large consequences on the global water uptake performance. However, the quantification of the influence of the hydraulic or anatomical traits at the root cross-section level is experimentally challenging.

To overcome the experimental difficulty of measuring the root radial hydraulic conductivity (k_r) and the corresponding root traits, we used computational modeling tools. As the GRANAR - MECHA coupling provides the ability to explore and test any hydraulic anatomy and thus its influence over the k_r, we estimated the k_r of 7000 diverse hydraulic anatomies of maize roots with three levels of hydrophobic barriers deposition. Then, we trained machine learning models (meta-models) to speed up the estimation of the k_r. These meta-models are relevant tools to pin-point the direct influence of their input variables on the k_r. Hence, we conducted a variance decomposition test with

the "extended FAST" and a "Sobol" sampling methods to evaluate the direct and interaction indices of five anatomical traits and three subcellular hydraulic properties on the k_r. We selected the range of variations for these variables during a meta-analysis.

From the meta-analysis of the anatomical data-sets, allometric relationships were quantified between the cross-section area and the stele area, and also between the stele area and the xylem area. However, neither the ratio between the cross-section area and the stele area nor the stele area vs. the xylem area explained more than 1 % of the total k_r variability during the global sensitivity analysis. The factors which directly influenced the most of the k_r before the suberization stage, were the contribution of aquaporins to the cell membrane permeability and then the cell walls hydraulic conductivity. In addition, the interaction effects of both these subcellular hydraulic properties with the other variables were substantial (15-20 % of the variance explained). However, after the suberin deposition, the k_r was mostly influenced by the conductance of individual plasmodesmata (67-72 % of the variance explained). Although anatomical traits seems to be less influential than the subcellular hydraulic properties radially, the total effect index over the k_r of the root radius was about 12 %, and 4 % for the aerenchyma proportion, before the suberization of the endodermis.

The performed global sensitivity analysis suggests that the root radial hydraulic conductivity is mostly influenced by subcellular hydraulic properties and to a lesser extent by the root radius and the aerenchyma.

4.1 Introduction

In roots, the main radial fluxes of water occur along the paths of least hydraulic impedance. These paths are spread in complex networks that are formed by a combination of the apoplastic, transmembrane and symplastic hydraulic pathways (Steudle et al., 1993). These routes are defined by the geometric cell arrangement and the hydraulic conductivity of the different cellular compounds which compose them. In addition, the deposition of hydrophobic compounds in some layers (e.g., at the endodermis and/or the exodermis) of the root highly influence the partitioning between the different water pathways (Steudle, 2000). The anatomical architecture of the root sets the foundation of radial hydraulic conductivity, as it is considered to be less plastic than subcellular hydraulic properties which are more dynamically

controlled by the plant (Hachez et al., 2012). Therefore, to better understand the components of the radial hydraulic conductivity (k_r) and its leverage points, we would need to figure out the influence of the root anatomy and the related subcellular hydraulic properties on these key features of the water uptake.

The quantification of the influence of anatomical traits and cell hydraulic properties on the hydraulic conductivity remains challenging due to complex and time-consuming experimental procedures. Assessing their impact globally on the root system conductance is even more complicated. However, current structural functional plant models make it possible to simulate part of these water movement processes in the plant. Although they may work at different scales or focus on different aspects, allowing them to be connected in a structured network of models containing several aspects of the whole root water uptake process would overcome the difficulty of reaching the hydraulic properties of the plants. It would also have the ability to investigate the effects of certain sets of traits that would be hard to find in nature. As suggested by Passot et al. (2019), we could use different computational models to simulate plants water uptake in soil with a coupling between macro- and micro-scale models to address these questions. Thus, computational models are potentially useful instruments for virtual breeding as they allow the investigation of the performance of any desired combinations of root traits (Chapman, 2008). In addition, they can enable the quantification of the main influence of root traits, but also, the total influence including interaction processes on a series of variables which assess the overall performance within any pedo-climatic scenarios.

Although *in silico* experiments of complex systems are fast in comparison to *in vivo* ones, the computational time can easily stretch as the number of parameters to be tested increases. Doing exploratory studies with modeling tools may help us to navigate across the root traits diversity with a fairly high efficiency. However, a cross-talk between exploratory work using models and *in vivo* testing of promising results should always be kept in mind.

At the cellular scale, the model of explicit cross-section hydraulic anatomy (MECHA, Couvreur et al., 2018) allows the estimation of the radial hydraulic conductivity (k_r). This computational model works at the cellular scale, explicitly taking into account portions of walls, membranes, and plasmodesmata of individual cells. Consequently, it unlocked the possibility to analyze the influence of subcellular hydraulic properties on the k_r. In addition, MECHA requires an accu-

rate representation of the cell arrangement in the root cross-section in order to estimate the radial fluxes of water across it. The digital segmentation of a root cross-section is a limitation to the use of such a model, as it is time-consuming, even with semi-automated software such as CellSeT (Pound et al., 2012). However, in combination with a root anatomy generator (such as GRANAR), it opens the way to a systematic analysis of the functional properties of a large number of root anatomical traits and subcellular hydraulic properties.

Previously, sensitivity analysis with these computational models were performed on some anatomical traits (Heymans et al., 2020), as well as on some different subcellular hydraulic properties (Couvreur et al., 2018) to determine their impact on the k_r. These modeling approaches offered smooth trends over the individual influence of each tested parameter on the k_r. In addition, these trends are also supported by experimental measurements. Thus, it seems that the k_r is reduced when roots present large cortex width due to an increased number of cortex cell layers (Chimungu et al., 2014b), or large cortex cell size (Chimungu et al., 2014a). The aerenchyma lacuna seems to reduce the water pathway by creating gaps in the cortex when they form (Fan et al., 2007). Small stele diameter and, to a lesser extent, low amount of meta-xylem vessels also decrease the k_r (Heymans et al., 2020). The influence of subcellular hydraulic properties on the k_r is well established, via the contribution of aquaporins to the cell membrane permeability (Javot, and Maurel, 2002), or more recently, Couvreur et al. (2018) also showed how the cell wall hydraulic conductivity, or the conductance of plasmodesmata influence the k_r. Both modeling and experimental approaches also showed that the deposition of hydrophobic compounds in the cellular walls of the endodermis act as barriers, forcing the water to rely more on transmembrane and symplastic pathways which reduce the k_r (Couvreur et al., 2018; Wang et al., 2019).

However, the combined effects between the anatomy and the subcellular hydraulic properties is still poorly understood. The impact of interaction effects between the different traits may also change depending on the hydraulic maturation scenario. For example: the impact of the interaction between the aerenchyma proportion and cell wall conductivity may differ under a hydraulic scenario where there is only an endodermal Casparian strip, or where there is a fully suberized endodermis with a Casparian strip on the exodermis.

To highlight the quantitative interaction between the different root traits and better understand the effects related to the root traits diver-

sity, we conducted a global sensitivity analysis. In order to constrain the analysis within ranges that best reflect the reality, we embedded it into a meta-analysis on root anatomical traits. This allowed us to quantify the main and the total contribution of each studied anatomical trait and the ones of the subcellular hydraulic properties. To speed up the global sensitivity analysis part, we also trained different machine learning algorithms which bypass the heavy computational load of the GRANAR and MECHA models. We tested the response of these meta-models to validate the approach for future applications at the root system scale. Machine learning algorithms are often an opportunity when large amounts of data (e.g., simulated data) are available for their training and validation (Lobet et al., 2017). They can be used to bypass long simulation time once they are validated for a specific range of input parameters as they offer near "real-time" predictions.

4.2 Material and methods

To test the impact of the anatomy and the subcellular hydraulic properties simultaneously on the radial hydraulic conductivities (k_r) we performed a series of global sensitivity analysis. The model GRANAR and MECHA allowed us to change the anatomical traits and the subcellular hydraulic properties, respectively. The result between the combination of these models is an estimation of the root radial hydraulic conductivity (k_r), for each root "hydraulic anatomy".

To reduce the scope of the analysis we worked with maize (*Zea mais*) roots. The explanation of all selected input variables is detailed in the two following subsections, but here is the list of the selected anatomical traits that we included in the analysis: the root radius, the ratio between the stele and the cross-section area, the ratio between the xylem and the stele area, the cell wall thickness, and the ratio between the aerenchyma area and the cortex area, hereafter, called aerenchyma proportion. The selected subcellular hydraulic properties were: the cell wall conductivity, the aquaporin contribution to the cell membrane permeability, and the conductance of individual plasmodesmata.

Before conducting any analysis, we constrained the range of variation within predefined boundaries. To do that, we performed a meta analysis of the root anatomical traits with some open anatomical traits data-sets for maize (*Zea mays*).

4.2.1 Meta-analysis on root traits diversity

The anatomical data-sets from Burton et al. (2013a), Chimungu et al. (2014a), Gao et al. (2015), Heymans et al. (2021), Wahl, and Ryser (2000), and Yang et al. (2019) were used in this meta-analysis. All data-sets were reformatted to fit into a variable list which includes the total cross-section area (mm^2), the stele area (mm^2), the xylem area (mm^2), the number of cortex layers (#), the number of meta-xylem vessels (#), and the aerenchyma proportion (%).

To estimate potential allometric relationships between anatomical traits we performed mathematical operations to transform the data. Allometric relationships were then established between the different anatomical traits (Table 4.2.1). The mathematical operations used to transform the data included: (i) the log. natural of the whole root cross-section area *vs.* the log. natural of the stele area; (ii) the log. natural of the stele area *vs.* the square root of the absolute value of the log. natural of the meta-xylem area; (iii) the log. natural of the stele area *vs.* the log. natural of the number of meta-xylem vessels; (iv) the log. natural of the cortex width *vs.* the log. natural of the number of cortex cell layers.

For simplification purposes, we made the hypothesis that the root cross-sections and the meta-xylem vessels are cylindrical. Thereby, the linear regression coefficients could be used to obtain all other anatomical traits from the root radius. The estimated traits were the stele diameter, the meta-xylem area, the number of meta-xylem vessels, the number of cortex cell layers, and the cortex cell diameter. The relations leading to their estimation are summarized in Table 4.2.

This method allowed us to have the average root anatomical traits from any root radius in the range of this meta-analysis. Then, we added back some variation which would represent the root anatomical traits diversity. This was achieved through two coefficients of variation, one for the stele area, and a second for the xylem area. This left us with only one set of equations and four parameters to describe the root anatomical traits: the root radius, the coefficient of variation for the stele area (Cv_{stele}), the coefficient of variation for the meta-xylem area (Cv_{xylem}), and the aerenchyma proportion (P_{aer})

4.2.2 Generation of diverse root anatomies and subcellular hydraulic properties

Once we gathered the four anatomical parameters to describe the root anatomy, we added to the list a set of subcellular traits that could

Table 4.1: Range of variation for the different simulated hydraulic anatomies

Abbreviation, Unit	Variable description	Range of variation
Cv_{MX} (%)	Coefficient of variation from the expected ratio between the meta-xylem area over the stele area.	[-30; 30]
Cv_S (%)	Coefficient of variation from the expected ratio between the stele area and the root cross-section area.	[-30; 40]
W_{thick} (μm)	Cell wall thickness	[0.8; 2]
R (μm)	Root radius	[0.1; 1.5]
P_{aer} (%)	Percentage of aerenchyma area over the root cortex area.	[0; 0.5]
k_W ($cm^2 hPa^{-1} d^{-1}$)	Cell wall hydraulic conductivity	[$2.5E^{-5}$; $2.4E^{-3}$]
K_{PL} ($cm^3 hPa^{-1} d^{-1}$)	Plasmodesmata hydraulic conductance	[$5.7E^{-13}$; $5.3E^{-10}$]
k_{AQP} ($cm^2 hPa^{-1} d^{-1}$)	Aquaporin contribution to the cell membrane hydraulic conductivity.	[$4.5E^{-5}$; $4.3E^{-3}$]

potentially affect the k_r. These added parameters were the root double cell wall thickness ($W_{thickness}$), the contribution of aquaporin to the cell membrane permeability (k_{AQP}), the conductance of individual plasmodesmata (K_{PL}), the cell wall hydraulic conductivity (k_W).

The boundaries for the $W_{thickness}$ parameters were set from 0.8 to 2 μm. In Bouranis et al. (2003) study, the average cell wall thickness of maize root was measured at 1.5-1.6 μm. Then, we added a $\pm 0.5\,\mu m$ range to it to include thin cell walls and larger ones. As the subcellular hydraulic conductivities are difficult to measure experimentally, these parameters were contained in a range from 0.1 to 10 times a reference value derived from literature. The k_{AQP} reference value was estimated at $5.0\,10^{-7}\,m\,s^{-1}MPa^{-1}$ from Ehlert et al. (2009). It was calculated by blocking aquaporins with an acid-load treatment. The k_W of maize root was measured at $2.8\,10^{-9} m^2 s^{-1} MPa^{-1}$ by Zhu, and Steudle (1991). The K_{PL} was estimated at $2.4\,10^{-7} m\,s^{-1} MPa^{-1}$ (Couvreur et al., 2018), based on plasmodesmata frequency data from Ma, and Peterson (2001), and the conductance of individual plasmodesmata estimated by Bret-Harte, and Silk (1994).

To explore broadly each parameter range and obtain a maximal coverage of the multi-spectral dimension created by each input, we used a pseudo random sampling with the Mauntz-Kucherenko's scheme (Saltelli et al., 2010; Tarantola et al., 2007) with a uniform distribution for all parameters (Table 4.2.1). The number of samples was calculated as: $N = 2^{10}(2k + 2)$ thus, equal to 18 432.

In the following, the anatomical traits with artificial variation were used as input in the Generator of Root Anatomy in R (GRANAR) to simulate the cellular arrangement of the root cross-sections (Table 4.2.1). To increase the amount of possible successful root anatomies generated, when the root radius was smaller than 0.2 mm the aerenchyma proportion was reduced tenfold. For small roots, a large proportion of aerenchyma, means that more than the possible number of cortex cells should be removed because the cortical area includes the epidermis, the exodermis and the innermost cortex cell layer. Root anatomies presenting errors were discharged from the analysis. These errors come from misplaced cells and unsuccessful voronoi tessellation. The errors were randomly appearing across the range of root cross-section generation procedures. The total number of root cross-sections generated with no default was 6924 out of the 18 432. No retry with other randomizing seed were tested.

4.2.3 Estimation of the radial hydraulic conductivity

The model MECHA (Couvreur et al., 2018) was used to estimate the k_r from all root cross-sections generated previously with GRANAR. The scripts coupling these computational models are available on the gitHub repository
https://github.com/HeymansAdrien/GranarMecha (doi: 10.5281/zenodo.5582750)

The k_r was estimated for three different hydraulic scenarios. A first one with only an endodermal Casparian strip (En_{cs}), a second one with a fully suberized endodermis (En_{sub}), and a third one with an exodermal Casparian strip and a fully suberized endodermis ($Ex_{cs} + En_{sub}$).

4.2.4 Training the meta-models

The 6924 root cross-sections generated with their three associated values of k_r were imported in the R software (version 3.5.1, R Core Team, 2018) to train the meta-models. Using this software, we used

the library *'caret'* to train and validate the meta-models. The partitioning between the data used to train and validate the meta-models was eighty percent and scattered randomly across the whole range of the k_r values. To control the training process, a tenfold cross validation algorithm was applied, using root mean square error as the metric to assess the training performance. The type of algorithms that were tested were the "support vector machine with radial basis function kernel", and the "random forest" ones. The mean values of both machine learning methods were also evaluated to predict k_r, which was accounted as a third meta-model type.

The final evaluations between the meta-models were made by comparing the accuracy of each meta-model with a Student t-test, the root mean square error, the r-square, and the normalized root mean square error. Each machine learning model was trained five times with different randomized seeds to provide the mean accuracy level for each meta-model.

4.2.5 Global sensitivity analysis

To understand which anatomical traits and subcellular hydraulic properties influence the k_r we did a global sensitivity analysis. The meta-models with the best accuracy were used to predict k_r values for the global sensitivity analysis in each of the three root maturation scenarios.

The metrics used to evaluate the impact of each parameter on the k_r were Sobol's indices, close to a Monte Carlo analysis. Sobol's estimators are divided into two types of indices. A direct variance-based measure of sensitivity S_i, called the "first-order sensitivity index", or "main effect index", and it is described by the following equation:

$$S_i = \frac{V_i}{VAR(Y)} \tag{4.1}$$

where $V_i = VAR(E[Y|X_i])$ is the expected reduction in variance that would be obtained if X_i could be fixed, and Var(Y) is the overall variance of the output

Then, there is the "Total-effect index" or "Total-order index", ST_i. This estimates the contribution to the output variance of X_i, including all variance caused by its interactions, of any order, with any other input variables. It is given as:

$$ST_i = \frac{E_{x\,i}[VAR_{x\,i}(E_{x\,i}[Y|X_i])]}{VAR(Y)} \tag{4.2}$$

where $E_{x\,i}[VAR_{x\,i}(E_{x\,i}[Y\|X_i])]$ is the expected variance that would be left if all factors but X_i could be fixed.

The package *'sensitivity'* was used in the R software (R Core Team, 2018) to perform the analysis. Two methods were used to compute these estimators: (i) the Mauntz-Kucherenko's scheme (Saltelli et al., 2010; Tarantola et al., 2007) to compute first order and total indices using improved formulas for small indices (function: *'Sobol2007'*), and (ii) the Saltelli's so-called "extendedFAST" method (Cukier et al., 1978; Saltelli et al., 1999) (function: *'fast99'*). Hereafter, the first method was renamed "Sobol" and the second "FAST" for more clarity.

Both methods used different sampling sizes to estimate the indices. For the FAST method, the sampling matrix had a Number of samples of $N = 2^{12} * k$, thus N equals 32 768. Sobol's approach used a sampling matrix calculated from $N = 2^h(2k + 2)$, with $h \in [11; 15]$. Sobol's method was applied 20 times to have repetitions in the estimation of the indices. For each repetition, h and the randomizing seed were reshuffled. The average of the different indices was then taken into account for the results.

4.2.6 Statistical analysis

All statistical analyses were conducted in the R software (version 3.5.1, R Core Team, 2018). The function *'t.test'* used to assess the accuracy of the meta-models vs. the ground-truth data for the validation procedure comes from the *"stats"* package. The R^2 values were computed from the *'lm'* fit function within the same package. The function used to compute the Pearson correlation coef. was the *'cor'* function with the argument "use" = *"complete.obs"*. To calculate the allometry coefficient between the different anatomical traits we used the *'aov'* function within the same *"stats"* package.

4.3 Results

4.3.1 Meta-analysis of root anatomical data-sets

From the anatomical data-sets from Burton et al. (2013a), Chimungu et al. (2014a), Gao et al. (2015), Heymans et al. (2021), Wahl, and Ryser (2000), and Yang et al. (2019) a series of allometric relationships were established between different anatomical traits. All transformed anatomical traits showed a strong correlation with the associated

anatomical traits. The results are presented in the Figure 4.1 and in Table 4.2.

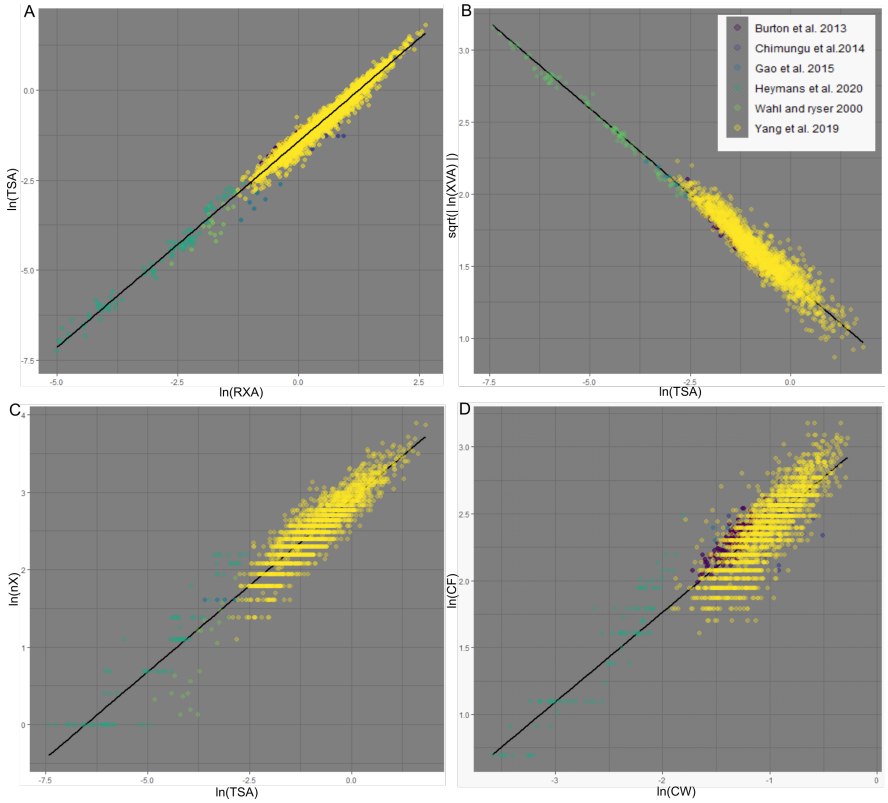


Figure 4.1: Allometry between root anatomical traits: A) Root cross-section area [RXA] and stele area [TSA]; B) Stele area [TSA] and xylem area [XVA]; C) Stele area [TSA] and the number of meta-xylem vessel [nX]; D) The cortex width (CW) and the number of cortex cell layers [CF]. The length unit is mm and the area are expressed in mm^2

We generated 6924 maize root cross-sections with a large range of variation in terms of anatomical traits and subcellular hydraulic properties based on very few parameters (Table 4.2.1). This was made possible with the use of the identified allometric relationships between anatomical traits. We estimated the radial hydraulic conductivities (k_r) for those generated anatomies using the model MECHA for three hydraulic scenarios with different set of hydrophobic barriers: (i) with

Table 4.2: Linear regression among the different Naperian logarithm of the root anatomical traits

Variable	**Equations**	***P* value**	R^2	Pear. corr.
TSA	$ln(TSA) = -1.4217 + 1.1441\, ln(RXA)$	$< 2e^{-16}$	0.9684	0.9839
XVA	$\sqrt{\|ln(XVA)\|} = 1.3955 - 0.2430\, ln(TSA)$	$< 2e^{-16}$	0.9347	-0.9668
nX	$ln(nX) = 2.9116 + 0.4459 ln(TSA)$	$< 2e^{-16}$	0.8834	0.9399
CF	$ln(CF) = 3.1091 + 0.6719 ln(CW)$	$< 2e^{-16}$	0.7543	0.8685

an endodermal Casparian strip (En_{cs}), (ii) with an endodermis completely suberized (En_{sub}), and (iii) an endodermis suberized and an exodermal Casparian strip ($En_{sub} + Ex_{cs}$).

4.3.2 Machine learning algorithms facilitate the estimation of k_r

The three machine learning methods used to predict k_r were accurate in the three hydraulic scenarios (Table 4.3.2). The Student t-tests used to distinguish predicted values from the ground-truth data did not show significant differences ($p > 0.05$, Table 4.3.2). By comparing the average accuracy for each model type, we observed that the best model types were the *"mean model"* (mm), the meta-model which is the mean between the *"support vector model"* (svm) and the *"random forest model"* (rf).

The meta-models, one per hydraulic scenario, were used to speed up the estimation of k_r. This reduced the computational time to less than a millisecond instead of the broad time intervals between 30 seconds to 45 minutes for one GRANAR-MECHA simulation depending on the size of the root cross-section (including the loading of the libraries).

4.3.3 Influence of the anatomy in combination with the hydraulics

The different global sensitivity analysis conducted in the three hydraulic scenarios showed the influence of anatomical traits and the subcellular hydraulic properties on the k_r. The two sampling methods used to perform the variance decomposition show similar trends when

Table 4.3: Machine learning model fitness to rapidly estimate k_r. Five models of each type were trained per hydraulic scenario. The ground-truth data obtained from the coupling between GRANAR and MECHA was used to train and validate these meta-models. The three meta-model types were: the support vector machine with radial basis function kernels (svm), the random forest (rf) and the mean model which is the average between the two predictions of the rf and the svm. The p-value of the Student's t-test for the evaluation between the predicted values and the ground-truth data was considered as non-significant above 0.05.

Hydraulic scenario	**Machine learning methods to estimated kr**	**Norm. root mean square error (n=5)**	R^2 **(mean, n=5)**	**p-value of the t-test (mean, n=5)**
En_{cs}	svm	2.010 %	0.981	0.912
	rf	2.785 %	0.968	0.891
	mm	2.037 %	0.983	0.933
En_{sub}	svm	2.267 %	0.984	0.843
	rf	2.717 %	0.979	0.939
	mm	2.080 %	0.987	0.925
En_{sub} $+Ex_{cs}$	svm	2.219 %	0.984	0.906
	rf	2.446 %	0.983	0.912
	mm	1.963 %	0.988	0.927

hydrophobic scenarios increased from only the presence of a Casparian strip to a complete suberization (Figure 4.2). However, the ranking of the influence strength for the different variables changed depending on the methods. Here, we summarized the impact of each factor when similar trends were observed with both methods.

The most important factor of influence over the k_r varied between the scenarios. In the hydraulic scenario with the En_{cs}, the aquaporin contribution to the cell membrane conductivity (k_{AQP}) had the strongest direct impact on the k_r (39 % of the variance explained). When the endodermis was suberized (En_{sub}), the k_{AQP} influence decreased by a lot ($< 5\%$ of the variance explained). In that case and also when there was an exodermal Casparian strip in addition (En_{sub} + Ex_{cs}), the conductance of individual plasmodesmata (K_{PL}) was influencing the most the k_r (67 to 72 % of the variance explained).

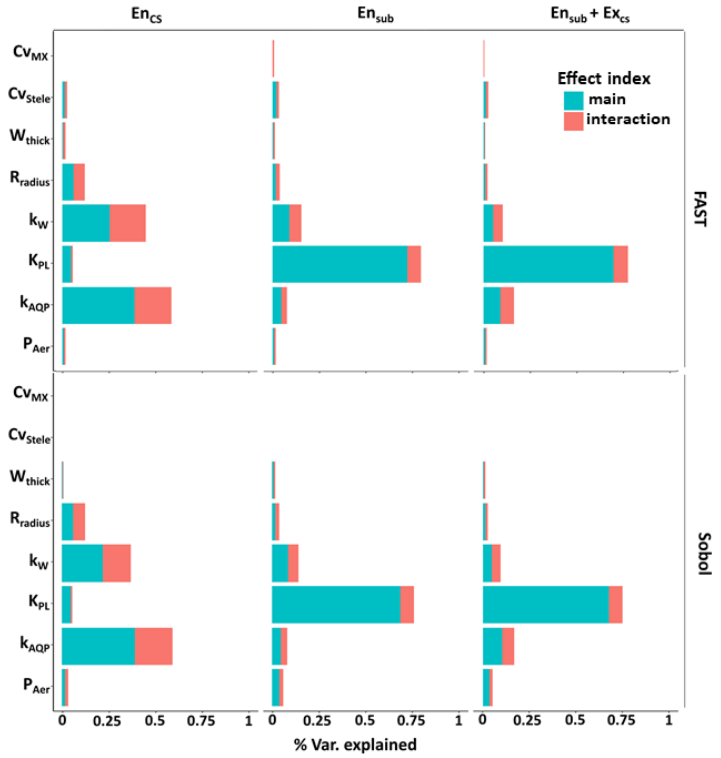


Figure 4.2: Variance decomposition following an extended Fourier Amplitude Sensitivity Analysis Test (FAST) or a Sobol sampling (Sobol). The three maturation scenarios were analyzed: En_{cs} = Endodermal Casparian strip; En_{sub} = Complete suberization of the endodermis; $En_{sub} + Ex_{cs}$ = An Exodermal Casparian strip and a complete suberized endodermis. The height input parameters of two variance decomposition methods are: Cv_{MX} = coefficient of variation from the standard xylem area ratio over the stele area; Cv_{stele} = coefficient of variation from the standard stele area ratio over the root cross-section area; W_{thick} = the cell wall thickness; $Rradius$ = the root radius; k_W = the cell wall hydraulic conductivity; K_{PL} = hydraulic conductance of the plasmodesmata; k_{AQP} = the aquaporin contribution to the cell membrane hydraulic conductivity; P_{Aer} = the aerenchyma proportion in the cortex. The "main effect index" is the direct variance based measure of sensitivity. The "interaction effect index" is the part of the variance which is not part of the direct variance but part of the "total effect index" including all variance caused by its interaction with all other input variables.

The cell wall conductivity (k_W) was also a major factor of influence over the k_r, but more so when there is only an endodermal Casparian strip (from 22 to 26 % of the variance explained under En_{cs}). Its impact over the k_r was decreasing with the deposition and the formation of hydrophobic barriers. More lightly, the root radius (R_{radius}) also had an influence on the k_r, about 6 % of the explained variance under En_{cs}, but with the interaction effects, the total influence reached 12 %. After the suberization stage, its influence decreased with the deposition of hydrophobic barriers. In opposite to the decrease of influence with the deposition of hydrophobic barriers observed for k_W and R_{radius}, the k_{AQP} influence was partially restored in the hydraulic scenario where the exodermal Casparian strips was added to the other hydrophobic barriers (9 to 10 % of the variance explained).

While the root radius had relatively small influence over k_r, this parameter revealed to be one of the major factors of influence over the radial hydraulic conductance (Kr, Appendix Figure 4.4). Approximately 21 to 23 % of the variance explain was mainly due to this parameter across all hydraulic scenarios.

The "direct" effects of all parameters exceeded the interaction effects on the k_r. However, the interaction effects added up substantially to the corresponding "direct" effect. With endodermal Casparian strips, two strong interactions with other variables influencing the k_r were identified: the interaction effect of the k_W which was about 15 to 19 % of the variance explained, and the interaction effect of the k_{AQP} which was approximated at 20 % of the variance explained.

Among the weak influencing factors, the aerenchyma proportion (P_{aer}) accounted for 1 to 4 % of the variance explained. The other factors of influence tested in this global analysis, the cell wall thickness (W_{thick}), the ratio of xylem area over the stele area (Cv_{MX}) and the stele ratio over the total root cross-section area (Cv_{stele}), accounted for less than 1 % of the variance explained.

Globally, all tested factors were positively correlated to the k_r with the exception of the P_{aer} and R_{radius} which were negatively correlated.

4.4 Discussion

The most accurate estimator for the root radial hydraulic conductivity (k_r) was the average of both trained meta-models, which is often the case when we refers to the ensemble theory (Dietterich, 2000). Overall,

the trained meta-models were all accurate with less than 3 % of normalized root mean square error. The average of the different trained meta-models increased the accuracy by 1 %. The real time predictions of the k_r ($60\mu s$ / prediction) sped up the global sensitivity analysis substantially. These meta-models enabled us to quickly perform a Morris screening (Appendix 4.5) and make the comparison between different methods to obtain the Sobol's indices. For future applications with the same range of variation of our study, these meta-models could be re-use for the estimation of the k_r and reduce drastically the simulation time.

The results of the global sensitivity analyses confirmed the importance of the conductance of individual plasmodesmata (K_{PL}) after the suberization stage. This is consistent with the results of Couvreur et al. (2018). They also showed that K_{PL} was the most limiting element of the water pathway under the scenarios with the same hydraulic barriers.

The contribution of the aquaporins to the cell membrane permeability (k_{AQP}) was the most influencing factor on the k_r before the complete suberization of the endodermis. Once the endodermis walls were hydrophobic the influence of k_{AQP} decreased drastically, but it was re-balanced lightly with the addition of the exodermal Casparian strips. The main hypothesis would be that aquaporins allow the switch from the apoplastic pathway to transmembrane at the endodermis and exodermis when there is a Casparian strip but no suberization yet. In the case of complete suberization of the endodermis, the transmembrane transition occurs downstream and upstream of this layer, increasing the length of the symplastic pathway, which then relies exclusively on transport through plasmodesmata across the endodermis. An example case with a visual representation of this phenomenon is provided in Figure 4.3. Then, the K_{PL} influences the rate of the cell-to-cell water transport. In addition, the cell-to-cell water transport is less conductive than the apoplastic pathway in most of the tested cases. Hence, in the selected scenarios, the k_{AQP} is thought to have an impact on the partition of pathways, before and after apoplastic barriers, where the water transport can become transmembrane if the k_{AQP} is high enough. This is in line with the findings of Ding et al., 2020; Hachez et al., 2006 who observed specific "light up" of the aquaporins when a hydrophobic barriers are deposited. Therefore, before the suberization stage, the k_{AQP} had a strong impact on k_r, because the water transport is necessarily taking the transmembrane pathway, without having to flow through the plasmodesmata.

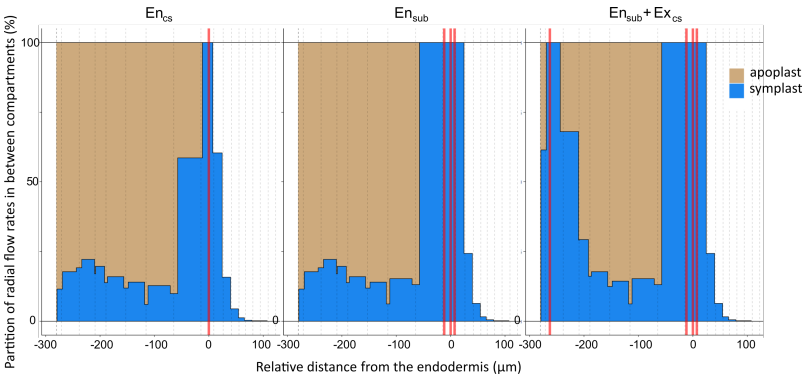


Figure 4.3: Partitioning of the radial water fluxes between the apoplastic and the symplastic compartments. Example case of a maize root cross-section with three hydraulic scenarios: (En_{cs}) an endodermal Casparian strip, (En_{sub}) an endodermis completely suberized, and ($En_{sub} + Ex_{cs}$) an endodermis suberized and an exodermal Casparian strip. Red lines show the position of the hydrophobic deposition. Dashed grey lines represent the discretization of different cell layers. The epidermis cell layers on the left side of the graphics are in perfect contact with the soil water and the center of the root cross-section is further on the right but was cropped out of the graphics for clarity purpose.

The small importance of the xylem parameter on the k_r reflects a trend already observed in Heymans et al. (2020). Although this study showed that xylem area does not influences the k_r as much as the other parameters, this trait was actually less representative of the actual diversity found during the meta-analysis of the anatomical traits. Perhaps including a new input variable for the meta-xylem vessel number which would increase the range could build up the influence of the xylem traits on the k_r. Nevertheless, it is most likely that radially it does not contribute as much as the other tested variables on the k_r. The high potential impacts of the xylem factors on the global water uptake dynamic are thought to be bigger as the axial water movements are accounted for (Bouda et al., 2018).

As we used the allometric relationships found during the meta-analysis to generate realistic root anatomies, a few anatomical traits inherit their values from the four selected anatomical traits (Root radius, ratio of stele area vs. cross-section area, ratio of the xylem area vs. the stele area, and the aerenchyma proportion). Some of them, such as: the cortex cell size, and the number of cortex layers, or the already mentioned number of meta-xylem vessels are subject to

be less representative of the actual diversity found during the meta-analysis of the anatomical traits (Figure in appendix 4.6). However, in Heymans et al. (2020), it was the cortex width as the integration of both cell size and number of layers that influenced the k_r.

Although in Heymans et al. (2020), most anatomical traits showed strong influence on the radial hydraulic conductivity, subcellular hydraulic properties were not included in that analysis. Under a larger scope of investigation, the subcellular hydraulic properties lead to larger variation than the anatomical traits. However, it does not mean that anatomical traits do not have some influence on the radial hydraulic conductivity. At the root system scale, Meunier et al., 2020 showed that the geometry rather than hydraulic properties matters more for the root water uptake function. However, in their simulations, the range of variation for these parameters was smaller than the one tested here.

Nevertheless, the root radius parameter had a stronger influence over the root radial hydraulic conductance. Thus, integrated into the whole hydraulic network, we could expect that this parameter will influence the global root water uptake function strongly.

In terms of equipment and expertise, characterizing subcellular hydraulic properties are more demanding than for anatomical traits. In practice, the hydraulic conductance of individual plasmodesmatal pore is still near impossible to measure experimentally. However, even if subcellular hydraulic properties may explain greater part of the radial hydraulic conductivity, the anatomical traits influence are easier and more accurate to include in future analysis with modeling tools such as the one used in this study.

The small differences in terms of the influence strength shown by the two different variance decomposition techniques are explained by the two sampling methods. Using different techniques to perform a global sensitivity analysis increases the robustness of the conclusions (Cosenza et al., 2013). Thus it is recommended if not too computationally intensif. The extended FAST approach was less computationally intensive than the Sobol method. However, the Sobol sensitivity analysis is more powerful as the number of input variables increases (Zhang et al., 2015), the main drawback being the computational cost.

4.5 Conclusion

The meta-analysis of several maize root anatomical data-sets showed that allometry relationships do exist between the root cross-section

area and the stele area, as well as between the stele area and the xylem area. These relationships can be used to describe a stereotypical maize root anatomy from root radius in the range of 0.1 to 1.5 mm.

The trained meta-models presented good fitness in the estimation of the root radial hydraulic conductivity (k_r) for the three tested levels of apoplastic barriers deposition, relatively to the GRANAR - MECHA coupling. The methods that presented the best accuracy was by taking the average between the different trained meta-models. This enabled us to have k_r predictions in near real time from five anatomical traits and three subcellular hydraulic properties in three hydraulic scenarios.

The "extendedFAST" and the "Sobol" techniques used to perform the global sensitivity analysis gave similar but not identical results.

The variance decomposition analysis of the meta-models on the k_r showed that after the endodermal suberization stage, the conductance of individual plasmodesmata (K_{PL}) is the most influencing factor on the k_r. Whereas, when there was an endodermal Casparian strip, it was the contribution of aquaporins on the cell membrane permeability that had the highest direct influence on the k_r, followed by the cell wall hydraulic conductivity which also strongly influenced the k_r. More lightly, among the selected anatomical traits, the root radius had the highest direct and total effect indices.

4.6 Appendix

Supplemental Figures

Morris screening

The Morris screening (Morris, 1991) is based on the "hypercube", where the sampling strategy follows "trajectory" with "jumps" to evenly sample in the multi-input dimensions. The function in R used to perform the Morris screening was *"morris"* from the package *'sensitivity'*. The number of selected "trajectory" was 20, the number of levels used to correspond to the number of input variables (k = 8), and we followed the recommendation of Morris (1991) to use k/2 for the number of "grid jumps".

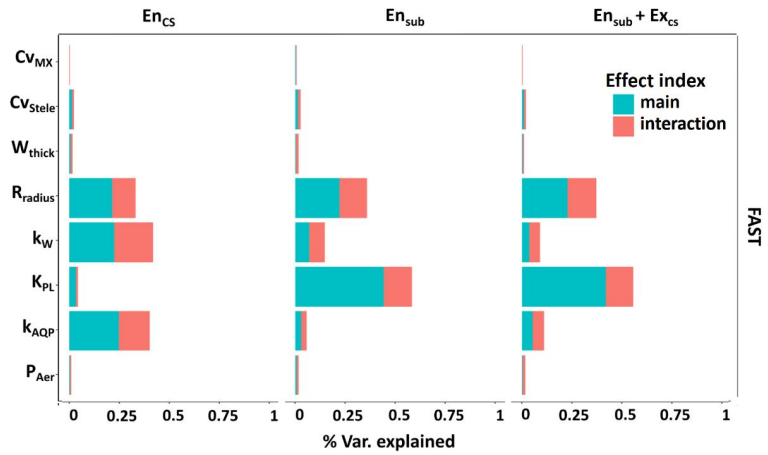


Figure 4.4: Variance decomposition following an extended Fourier Amplitude Sensitivity Analysis Test (FAST). The three maturation scenarios were analyzed: En_{cs} = Endodermal Casparian strip; En_{sub} = Complete suberization of the endodermis; En_{sub} + Ex_{cs} = An Exodermal Casparian strip and a complete suberized endodermis. The height input parameters of two variance decomposition methods are: Cv_{MX} = coefficient of variation from the standard xylem area ratio over the stele area; Cv_{stele} = coefficient of variation from the standard stele area ratio over the root cross-section area; W_{thick} = the cell wall thickness; $Rradius$ = the root radius; k_W = the cell wall hydraulic conductivity; K_{PL} = hydraulic conductance of the plasmodesmata; k_{AQP} = the aquaporin contribution to the cell membrane hydraulic conductivity; P_{Aer} = the aerenchyma proportion in the cortex. The "main effect index" is the direct variance based measure of sensitivity. The "interaction effect index" is the part of the variance which is not part of the direct variance but part of the "total effect index" including all variance caused by its interaction with all other input variables.

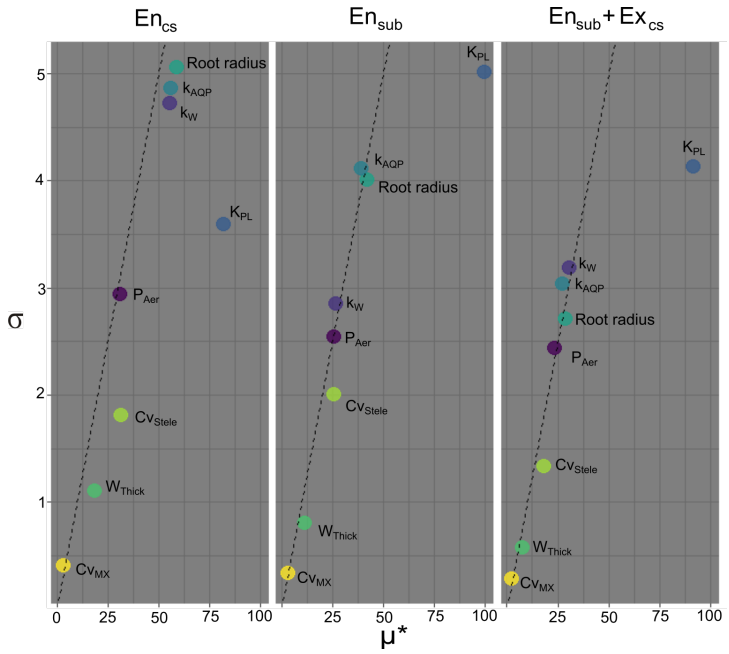


Figure 4.5: Morris screening on the k_r to qualitatively measure the influence of each input variables in each of the three hydraulic scenarios. The three maturation scenarios were analyzed: En_{cs} = Endodermal Casparian strip; En_{sub} = Complete suberization of the endodermis; En_{sub} + Ex_{cs} = An Exodermal Casparian strip and a complete suberized endodermis. The height input parameters were: Cv_{MX} = coefficient of variation from the standard xylem area ratio over the stele area; Cv_{stele} = coefficient of variation from the standard stele area ratio over the root cross-section area; W_{thick} = the cell wall thickness; $Rradius$ = the root radius; k_W = the cell wall hydraulic conductivity; K_{PL} = hydraulic conductance of the plasmodesmata; k_{AQP} = the aquaporin contribution to the cell membrane hydraulic conductivity; P_{Aer} = the aerenchyma proportion in the cortex. μ = the average of the absolute elementary effect ("Direct effect"), and σ = the standard deviation of the absolute elementary effect ("Interaction effect").

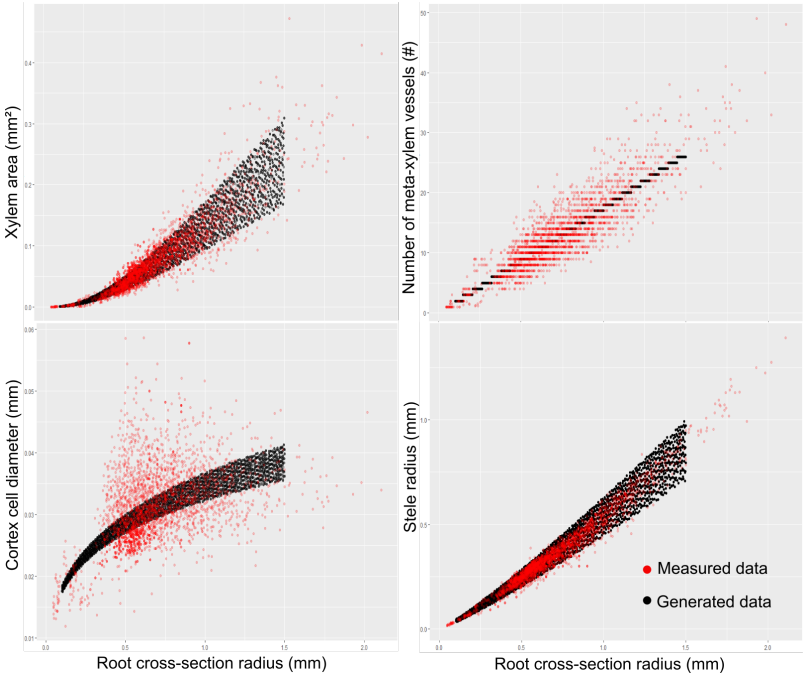


Figure 4.6: Allometry across anatomical traits

PART III

WATER FLOW IN THE ROOT SYSTEMS

The third part of the thesis zoom out from the root cross-section level. It integrates the information gathered at the root cross-section to the whole root system and includes it in an environment.
First, we combined models into a structured network in order to simulate the soil - root water uptake dynamics. This allowed us to pinpoint specific root anatomical traits, subcellular hydraulic properties and maturation rates which could improve the root water uptake ability in a given environment.
Secondly, we tested *in silico* the hypothesis that maize landraces could have a set of root traits hydraulically adapted for their native pedo-climatic conditions.

"The important thing about a problem is not its solution, but the strength we gain in finding the solution." —

Seneca

ANALYSIS OF THE INFLUENCE *IN SILICO* OF HYDRAULIC ANATOMY ON MAIZE ROOT WATER UPTAKE

5

This chapter is the edited version of a scientific article in preparation, entitle as:

> Adrien Heymans, Valentin Couvreur, Clément Saint-Cast, and Guillaume Lobet. *In silico* analysis of the influence of local root traits on global root hydraulic dynamics. (in progress)

ABSTRACT

FINDING PLANTS that are well adapted hydraulically to specific pedo-climatic environments is aimed for present and future yield improvement and increasing the sustainability of our crop systems. Cultivated plants that have been selected through traditional farming systems in a region are most likely to express very different root anatomies and root hydraulic properties from place to place. These germplasms may have developed a root system hydraulic architecture particularly adapted in their location. A better understanding of the underlying properties could be put at use to target strategies, if needed, which could increase their water uptake in these specific environments.

Here, we associated different models into a structured network to virtually simulate water flow in the soil-root system over 30 days of crop development. This Virtual Phenotyping pipeline for root hydraulic traits (Hydraulic Viper) was built so we could pinpoint specific root anatomical traits, subcellular hydraulic properties and maturation rate which could improve the root water uptake in a chosen pedo-climatic environment. We tested this hypothesis on maize plants (*Zea mays* variety *B73*) and in three pedological conditions under a high evaporative demand and water limiting conditions. We

generated 7168 maize plants from a single set of architecture traits but varying sets of anatomical traits, subcellular hydraulic properties and maturation rates. All root traits were sampled in their uniform distributions following pseudo-random techniques (Saltelli et al., 2010) for a Monte-Carlo like analysis. Then, we analysed their root water uptake dynamics in all three environments.

We identified that the root radius of zero-order roots were the most influencing variables over the root water uptake of these *in silico* phenotypes. The phenotypes with a high contribution of aquaporins to the cell membrane permeability and short delay between the suberin deposition and the maturation of the meta-xylem vessels increased their root water uptake when water was available. In each of the three environments, we observed significant differences in terms of root radii optimum when aiming for phenotypes which expressed high cumulative water uptake and high cumulative water uptake per unit of root volume. Next, we generated three batches of 56 new plants designed for each one of the three tested environments. They were able to take up high amount of water in total, at a low carbon cost.

Therefore, using the Virtual Phenotyping pipeline for Root hydraulic traits, it was possible to estimate potential optimum traits depending on pedo-climatic constraints. These early *in silico* results suggest that root radii, the contribution of aquaporins to the cell membrane permeability, and maturation rates are important traits to target when looking for adapted traits in specific environments.

5.1 Introduction

Irrigation has been traditionally used to counter the lack of rainfall and soil water availability when plants are exposed to water limitations. At the same time, it is costly economically and environmentally and more so with the current climate change (Ronco et al., 2017). To alleviate the potential issues related to limited water access, new types of water practices emerged and some plant cultivars were selected with drought tolerant traits (Raza et al., 2012). In addition, breeders have been focusing on yield stability, plant transpiration responses, leaf growth, or temporal adaptation so plant resistance to drought increased (Campos et al., 2004). More so, root traits selection has been set aside of mainstream breeding programs, even if they fulfill the major water uptake function. In some cases, seeking for drought tolerance has led to a decrease of the root biomass and length within a series of selection cycles (Bolaños et al., 1993; Fradgley et al., 2020).

Methods to capture the complexity of the root system are complex, expensive and rarely upscalable at the field level. The major difficulty is the soil itself, which prevents direct experimental observation and access to the roots. Fortunately, new methods start to scratch the surface of this underground world (e.g. shovelomics), allowing researchers to gather few yet important structural traits at the top of the root system (Trachsel et al., 2011). In addition, some modeling tools use state-of-the-art knowledge to recreate plants and their environment as faithfully as possible. These modeling tools enable the quantification of some biological processes, such as the partitioning of root water uptake function, that are difficult to measure experimentally. They allow the exploration of different combinations of phenotypic traits that could offer higher water uptake for their study cases. At the field level, it is complex to measure root traits in high throughput and at the cell scales. This is a gap where structural-functional plant models might help us understand the intricacy of the root water uptake function and provide insights for root traits base selection (Passot et al., 2019; Rellán-Álvarez et al., 2016).

Understanding the root system architecture and its related hydraulic properties as a whole is needed to develop strategies that would increase crop water uptake to specific pedo-climatic environments (Maurel, and Nacry, 2020). The structure of the root system governed by architectural traits, such as the root growth rate or the branching frequency, allow the roots to explore the soil domain and reach accessible soil water. Then, the soil and root hydraulic properties define the ease with which water can be absorbed from the soil. From the bulk soil to the xylem vessels, these properties reflect frictions along the water pathways, the soil but also the different cell layers of the roots, and bypass hydrophobic barriers. Therefore, the full comprehension of the roots ability to take up water requires the fine knowledge of the root system hydraulic architecture at different scales. Recent works aimed at better understanding the role of anatomy (Heymans et al., 2020; Rieger, and Litvin, 1999), cell hydraulic properties (Couvreur et al., 2018; Javot, and Maurel, 2002), or soil hydraulic properties (Carminati, and Javaux, 2020) over the root water uptake. However, individual traits are usually analysed independently to the others, and not always integrated to the global soil-plant system.

At the root system scale, the maize root system hydraulic architecture solver (MARSHAL) (Meunier et al., 2020) can be used to quickly estimate a series of macro-hydraulic properties, such as the equivalent root system conductance (K_{rs}), or the standard uptake fraction (SUF).

Those macro hydraulic properties can implicitly take into account the whole root system hydraulic architecture and be defined at the plant scale, as well as over the entire soil domain (Couvreur et al., 2012). Associated with a hydrological model and the "macroscopic" water uptake model of Couvreur et al. (2012), MARSHAL could enable the simulation of plant water dynamics within a soil. This would provide an exploratory tool to test different sets of root traits and evaluate their potential effects on the global root water uptake dynamics.

In this study, we associated different models into a structured network to virtually simulate water flow in the soil-root system over 30 days of crop development. This phenotyping pipeline was built so we could pinpoint specific root traits at the root cross-section scale which improve the root water uptake in a chosen soil type. Then, we focused at better understanding whether the subcellular hydraulic properties and the root anatomy which were influencing the root radial hydraulic conductivity at the cross-section scale reflect themselves in a similar way at the plant scale. We tested this hypothesis on maize plants (*Zea mays* var. *B73*) and in three pedological conditions under a high evaporative demand.

5.2 Material and methods

5.2.1 Simulation design

For this study, the three chosen pedo-climatic conditions were three different soil types in Palermo (Italy) for 30 days between the months of May and June 2018. This location was chosen because maize plants could have high potential evaporative demand and face scarce rainfall events, which could trigger water stress but also potential recovery (Details in Appendix 5.12). We generated 7168 maize plants with a root system architecture based on experimental data from the cultivar *B73* (Details in subsection 5.2.2, GitHub repository: *HydraulicViper/HydraulicViper*). The root system architectures are similar to one another but a small deviation (10%) was included in that parametric space. The differences between these *in silico* phenotypes were focused on anatomical traits, subcellular hydraulic properties, and root maturation rates (Table 5.2.1). All traits were sampled from their uniform distributions following Tarantola et al. (2007) and Saltelli et al. (2010) techniques for a Monte-Carlo like analysis. Sobol's approach used a sampling matrix calculated from $N = 2^h(2k + 2)$, where $h = 8$ and $k = 13$.

Table 5.1: Range for the input variables used to estimate k_r and K_x along the root axis

Abbreviation, Unit	Variable description	Range of var.
Cv_{MX} (%)	Coefficient of variation from the average ratio between the meta-xylem area over the stele area.	[-20; 20]
Cv_S (%)	Coefficient of variation from the average ratio between the stele area and the root cross section area.	[-30; 40]
R_{Lat} (μm)	Lateral root radius	[100; 150]
R_{Sem} (μm)	Seminal root radius	[200; 400]
R_{SBR} (μm)	Shoot born root radius	[300; 700]
P_{aer} (%)	Percentage of aerenchyma area over the root cortex area.	[0; 0.5]
k_W ($cm^2 hPa^{-1} d^{-1}$)	Cell wall hydraulic conductivity	[$1E^{-4}$; $4E^{-4}$]
K_{PL} ($cm^3 hPa^{-1} d^{-1}$)	Plasmodesmata hydraulic conductance	[$6E^{-13}$; $1E^{-11}$]
k_{AQP} ($cm^2 hPa^{-1} d^{-1}$)	Aquaporin contribution to the cell membrane hydraulic conductivity.	[$2E^{-4}$; $7.5E^{-4}$]
dt_{S-MX}, (day)	time delay between the beginning of the endodermis suberization and of the meta-xylem maturation.	[-0.5; 4]
dt_{MX}, (day)	duration of the maturation of the meta-xylem vessels	[1; 4]
dt_{Hb}, (day)	duration of the deposition of hydrophobic barriers or the delay between two levels of hydrophobic barriers	[1; 4]

Hydraulic Viper

The whole Virtual Phenotyping pipeline for root Hydraulic traits (Hydraulic Viper, Figure 5.1) worked as follow: (i) generation of root system architecture (RSA), (ii) associations of the radial and axial hydraulic conductivities (k_r and K_x) on the root types axis depending on the root anatomy, subcellular hydraulic properties and maturation rates, (iii) simulation of an initial soil water profile ($\Psi_{soil\,water}$), (iv) estimation of the root system hydraulic architecture ($RSHA$), (v) For every time steps, there was an update of the $\Psi_{soil\,water}$ and the root system hydraulic architecture. Then, for the next time step, we updated the estimation of the Soil-Root system hydraulic architecture accordingly to the previous $\Psi_{soil\,water}$. (vi) In the feedback loop, there was a comparison and an update of the collar water potential (Ψ_{col}) to match the potential shoot water demand (T_{pot}) with the root water uptake rate (T_{act}). In addition, the Ψ_{col} was contained above -15 000 hPa to take into account maize isohydricity behavior.

5.2.2 Root system hydraulic architecture

We used the CPlantBox model (Zhou et al., 2020) to simulate the 3D explicit root system architecture (RSA). The root system parameters were derived from a pot experiment in UCLouvain greenhouse where the maize cultivar *B73* grew for 18 days. Plant materials and growing conditions were the same as in Chapter 3, section 3.2.1. The root systems were carefully washed after 18 days, and the roots were scanned on a flatbed scanner. Root traits needed for the parameterization of the five root types of the maize root system of CPlantBox were extracted with the plugin SmartRoot (Lobet et al., 2011) from ImageJ (version 1.47) and processed in the R software (R version 3.5.1). The complete protocol used to simulate the maize cv. *B73* can be found on a GitHub repository (github.com/HydraulicViper/HydraulicViper, doi: 10.5281/zenodo.5582750).

As we accounted for anatomy, we selected three independent root radii, one for seminal roots, one for shoot-born roots, and one for lateral roots (Table 5.2.1). Among the seminal root radius, the basal root radii were resized as 75 % of the tap root radius. For laterals, long lateral root radii were increased by 25 % from the other short laterals. These small changes are related to observation made on our scanned maize root systems. Then, for the shoot-born roots, their root radius (r_i) were resized according to their emergence time ($DelaySB$)

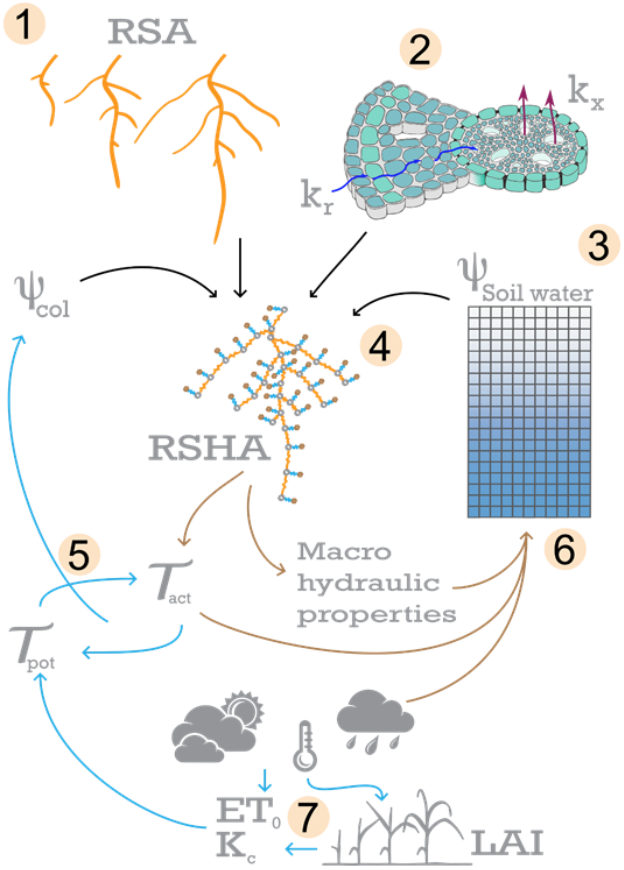


Figure 5.1: Overview of the virtual phenotyping pipeline for root water uptake (Hydraulic Viper). (1) Generation of the root system architecture (RSA); (2) association of the k_r and K_x on the root types axis; (3) simulation of an initial soil water profile ($\Psi_{soil\ water}$); (4) Solving the root system hydraulic architecture ($RSHA$); (5) comparison between the root water uptake rate (T_{act}) with the potential water demand (T_{pot}). If needed, update of the collar water potential (Ψ_{col}); (6) updated the soil water profile based on the implicit root water uptake model, and the atmospheric data. From this point, there is a loop on the soil water profile and the $RSHA$. (7) The atmospheric data were used to estimate the evapotranspiration rate of reference (ET_0) and the Leaf Area Index (LAI). From the LAI, the crop coefficient (K_c) was estimated which was used to estimate the T_{pot}.

relatively to the final recorded time (T_f) with the function:

$$r_i = r_i + r_i * (T_f - DelaySB_1 - (T_f - DelaySB_i))/10 \quad (5.1)$$

This enabled us to take into account the influence of the node level on the shoot-born root radius. The relations are based on an analysis of the root diameters of Yang et al., 2019.

After importing the root system architecture in Hydraulic Viper, we reclassified the root based on their radius with twenty classes which translated into twenty root hydraulic conductivity functions.

Estimation of k_r and K_x

To associate the estimated k_r and K_x values along the root ages, we created functions that would convert root ages into maturation stages, similarly to what we observed at Chapter 3. The visual representation of the functions is shown in Figure 5.2.

We reused the meta-models trained in Chapter 4 to provide the radial hydraulic conductivity (k_r) from the set of anatomical traits and subcellular hydraulic properties. The parameters and their range are described in Table 5.2.1. Each k_r value was related to a specific stage of hydrophobic barriers deposition. The anatomical traits were also used to isolate the number of proto- and meta- xylem vessels and their sizes. Then, from this information we estimated two axial hydraulic conductance (K_x) which would represent two levels of vascular maturation. The estimation was made using the Hagen-Poiseuille law:

$$K_x = \sum_{i=1}^{N} \frac{\pi r_i^4}{8\eta} \quad (5.2)$$

where r is the radius of the i-th xylem vessel, and η the water dynamic viscosity around ($1m\,Pa\,s$)

5.2.3 Environmental feedback

Soil water profile

The soil water profiles were estimated with the model Hydrus-1D (Šimůnek et al., 2008). We selected three soil texture types with strong differences in terms of hydraulic properties: (i) silty clay, (ii) loam, and (iii) sandy loam. The water flow in the soil followed the single-porosity hydraulic model of Van Genuchten and Mualem with no hysteresis. The upper boundary condition was set with atmospheric values from

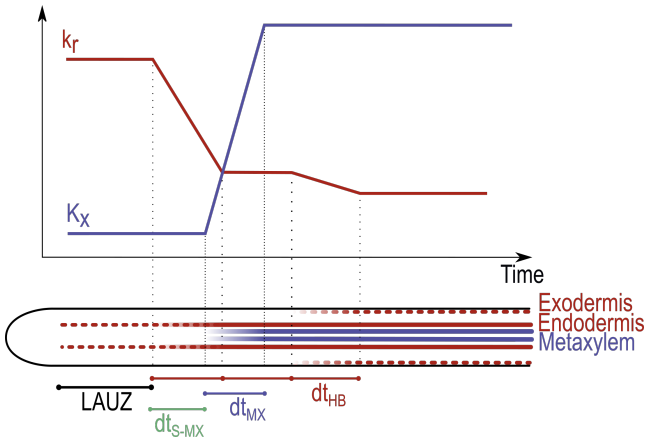


Figure 5.2: Age dependent hydraulic functions creating an offset between k_r and K_x along the root. Conceptual representation of the variation of radial (k_r) and axial (K_x) conductivities due to the maturation of hydrophobic structure (dashed red lines = Casparian strip; full red lines = complete suberization of the cell walls) and the maturation of the meta-xylem vessels (blue lines). LAUZ = duration of the unbranched zone (day); dt_{S-MX} = time delay between the end of the suberization of the endodermis and the beginning of the meta-xylem maturation; dt_{HB} = duration of the deposition of hydrophobic barriers or the delay between two levels of hydrophobic barriers; dt_{MX} = duration of the maturation of the meta-xylem vessels.

weather data (Details below) and potential surface run-off. The soil depth was established at 2 m and the lower boundary condition was set as free drainage. In addition, the Couvreur et al. (2012) model of "macroscopic" root water uptake model regulated the amount of water which was taken up by the plant at each soil layer. Thus, the macro hydraulic requirement for Hydrus to simulate water flow in the soil-plant system were, the root water uptake rate (RW_{act}), the Standard Sink Fraction including the local soil hydraulic conductivity (SSF_s), the equivalent soil-root system hydraulic conductance (K_{srs}), and the compensatory soil-root system hydraulic conductance ($K_{comp,\,s}$).

Each soil-plant simulation started with a uniform soil water profile. The soil water potential was first computed at the field capacity of the different soil types, then dried up by multiplying by two these values. As a result, the initial soil water potential of the silty clay soil was at -708.8 hPa; the loam soil was at -265.7 hPa; the sandy loam soil was at -147.0 hPa. This way, we expected to mimic a soil which is already depleted of some of its water. All generated root systems

were virtually put in all three soil types.

Dynamic adjustments between the soil and the RSHA

During the 30 days growing period, a feedback loop between the macro-hydraulic properties and the soil water profile was implemented in the virtual phenotyping pipeline to simulate the root water uptake dynamics. We made the choice of working with variable time steps: from 0.05 to 0.2 days depending on the conductance ratio of the equivalent soil-root system (K_{srs}) and the root system (K_{rs}) to account for the drop of local soil zone hydraulic conductivity in the soil due to soil drying. To compute the equivalent soil-root radial hydraulic conductivity (kr_{eq}) we used a set of equations from Meunier et al., 2018a; Schröder et al., 2009; Van Genuchten, 1980; van Lier et al., 2006 which are detailed in Appendix 5.6.3. The radial hydraulic conductivity of the soil-root was then used to find most macro-hydraulic hydraulic properties.

Estimation of the macro-hydraulic properties

The macro-hydraulic properties were estimated with the Maize root system hydraulic architecture solver (MARSHAL; Meunier et al., 2020). This model used the RSA, the related root hydraulic conductivities, the Ψ_{col}, and the soil water profile to compute the K_{rs}, the RW_{act}, and the Standard Uptake Fraction[1] (SUF) which translate directly into SSF when applied to the soil domain. In addition, a module was added into MARSHAL for the estimation of the K_{srs} (Appendix 5.6.3). It was computed following Meunier et al. (2018a), based on the local soil hydraulic conductance related to the local soil water content and the relative root zone of influence. This implied that, at each time step, we updated the equivalent soil-root radial hydraulic conductivity with Schröder et al. (2009) geometric parameter and van Lier et al. (2006) half distance between the root and the bulk soil (Appendix 5.6.3). Thus, it also changed the SUF to a soil influenced Standard Uptake Fraction (SUF_s) which would be the relative distribution of radial fluxes of water through the soil-root in a uniform soil water profile. Then, for each time step, $K_{comp,\,s}$ was

[1]The Standard Uptake Fraction (SUF) represents the relative distribution of root water uptake in a uniform soil water profile, based on the root system hydraulic architecture.

computed with the following equation:

$$K_{comp,\,s} = \frac{(\Psi_s - \Psi_{s,\,eq}) \cdot (J_r \oslash SUF_s - RW_{act})}{(\Psi_s - \Psi_{s,\,eq})' \cdot (\Psi_s - \Psi_{s,\,eq})} \tag{5.3}$$

where J_r is a vector of the sum of the water uptake of the root segments in each soil layer, Ψ_s is vector with the water potential of the bulk soil near the roots of a defined soil layer, and $\Psi_{s,eq}$ is the equivalent soil water potential felt by the plant, including the soil zone hydraulic conductance defined as:

$$\Psi_{s,eq} = \sum_{j=1}^{N} \Psi_{sr,j} * SUF_{s,\,j}$$

As the transpiration rate should be the minimum between the root water uptake rate and the shoot water demand, we evaluated the shoot water demand. The estimation was done with the Penman-Monteith method (Allen, and FAO, 1998, Appendix 5.6.2) and the crop coefficient derived from Campos et al. (2017). The specific meteorology data for Palermo (Italy) for 30 days between May and June 2018 were downloaded from the NASA Power project (Sparks, 2018). Script and data are available on the Hydraulic Viper GitHub repository (doi: 10.5281/zenodo.5582750). There was a $\pm$ 14 to 10 hours day-night cycle, with a stepwise function, and night transpiration rates was estimated at 18 percent of the day time transpiration rates based on Tamang, and Sadok (2018) work.

5.2.4 Statistical analysis

All statistical analyses were conducted in R (R Core Team, 2018). The different functions used in the global sensitivity analysis come from the package *"sensitivity"* (Iooss et al., 2021).

To compare the influence between the different root traits that were tested, we used a sensitivity index:

$$S_i = \frac{V_i}{Var\,Y} \tag{5.4}$$

where $V_i = \frac{MSE_{X,i}}{N}$ is the expected reduction in variance that would be obtained if the *'i'* input variable (X_i) could be fixed, and Var(Y) is the overall variance of the output.

The ANOVA conducted for this purpose was applied on a model where we measured the direct influence of all input variables on the

root water uptake at each time step independently. This was achieved with the function *'aov'* from the *"stats"* package. The root water uptake variables were standardized at each time step.

One-way ANOVAs were conducted to test the hypothesis that efficient phenotypes share the same input range across the different soil types. Tukey Tests were then performed to compare the soil type groups from each other with the function *'TukeyHSD'* from the *"stats"* package.

To test if two distributions were similar, we used the Kolmogorov-Smirnov test with the function *'ks.test'*.

When comparing the frequencies of finding "adapted" phenotypes within the boundary of the "highly efficient" ones, we used the function *'xtabs'* from the "stats" package.

5.3 Results

From the root system architecture of cultivar *B73*, 7168 maize root systems with small variability from one another were generated successfully. An example case of the root system architecture which was generated is shown in the Figure 5.3. All these root systems shared the same root architectural traits, but each one was unique in terms of root placement due to the inherent model stochasticity. We were able to simulate the root water dynamics of all growing root systems in three different soils, taking into account anatomical traits, subcellular hydraulic properties and maturation rates. The interaction between the soil water profiles and the root system hydraulic architectures resulted in root water uptake pattern which were evolving through time, linked to the distribution of roots but also to the micro-hydraulic properties (k_r and K_x) directly influenced by the selected input variables.

During the growing period, the root water uptake rate was soil dependent. We observed that the most significant differences between soil types appeared after 15 days. In the silty clay soil type, the simulated plants slowed down the water uptake rate more strongly than in the other soil types (Figure 5.4). Consequently, the cumulative root water uptake ($\sum WU$) was impacted by the soil type factor. After 30 days, it created strong differences between the overall plant water uptake depending on the soil types (P value < 0.05). All input variables had an influence on the root water uptake dynamics. The influence due to individual traits variation across phenotypes is illustrated with an example case in Figure 5.4 and detailed in the next subsection.

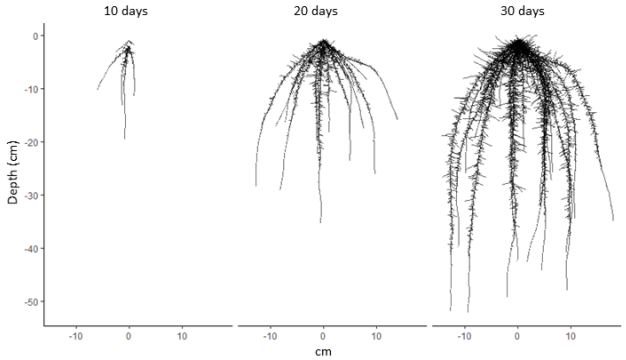


Figure 5.3: Example of the root system architecture for the maize cv. *B73*.

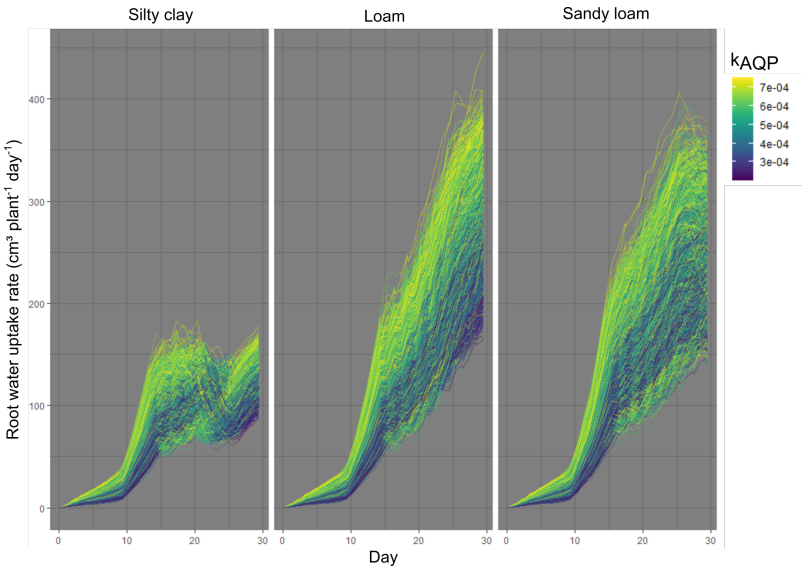


Figure 5.4: Root water uptake rate in the three different soil types. The attributed contribution of aquaporins to the cell membrane permeability (k_{AQP}; $cm\,hPa^{-1}.d^{-1}$) was coloured to highlight potential differences between phenotypes.

5.3.1 Influence of the hydraulic anatomy on the water uptake dynamics

To evaluate the influence due to individual factors (X_i), we quantified the "direct effect" (S_i), expressed here as the % of variance explained by X_i at each time step along the growing period. The cumulative water uptake was defined here as the integration of root water uptake rates over time. During the growing period, the direct influence of the different root traits on the cumulative water uptake changed (Figure 5.5). Before the 9^{th} day, the radius of the seminal roots (R_{Sem}) was the most influential factor on the cumulative root water uptake ($\sum WU$) and its influence was increasing as the plant grew. After that peak of influence on the 9^{th} day, the R_{Sem} influence dropped. However, the decrease of influence for the R_{Sem} was soil type dependent. In the sandy loam soil, the strongest decrease of influence was observed for this factor but it was in the silty clay soil that it was at the minimum at the end of the 30 days (p-value = 0.025). The decline was lessened in the case of the loam soil.

However, when looking at the "direct effect" of the R_{Sem} on the root water uptake rates, some occasional peaks of influence occurred briefly during the growth period. From the 20^{th} to the 25^{th} day, the influence of the R_{Sem} over the root water uptake rate regrew up to ± 0.5 of the variance explained in the silty clay soil (Appendix Figure 5.11). In addition, during that moment, the R_{Sem} was negatively correlated to the root water uptake rate in this soil type.

The contribution of aquaporins to the cell membrane permeability (k_{AQP}) strongly influences the cumulative root water uptake. Two peaks of influence were noticeable, the first one around the second day and the second one after 13 to 15 days. After the second peak, the k_{AQP} influence decreased at different rates depending on the soil type. In the sandy loam soil, it continuously shrank. Whereas, in the loam and in the silty clay soil the weakening trends stop after the 23^{rd} day to re-increase slowly. In the silty clay soil, the regrowth of influence was steeper than in the loam soil but it did not reach the same level of influence as in the loam soil which kept an overall steadier k_{AQP} influence.

The impact of shoot-born root radius (R_{SBR}) started one day after their emergence. The influence of this factor was increasing as the plant grew, but reached a plateau after 25 days. However, the height of the plateau seems to be soil dependent. In the sandy loam soil, the R_{SBR} explained a greater part of the total variation than in the loam

soil. However, in the silty clay soil, a sudden drop of R_{Sem} influence on the root water uptake rate occurred briefly from the 20 to the 25^{th} day (Appendix Figure 5.11).

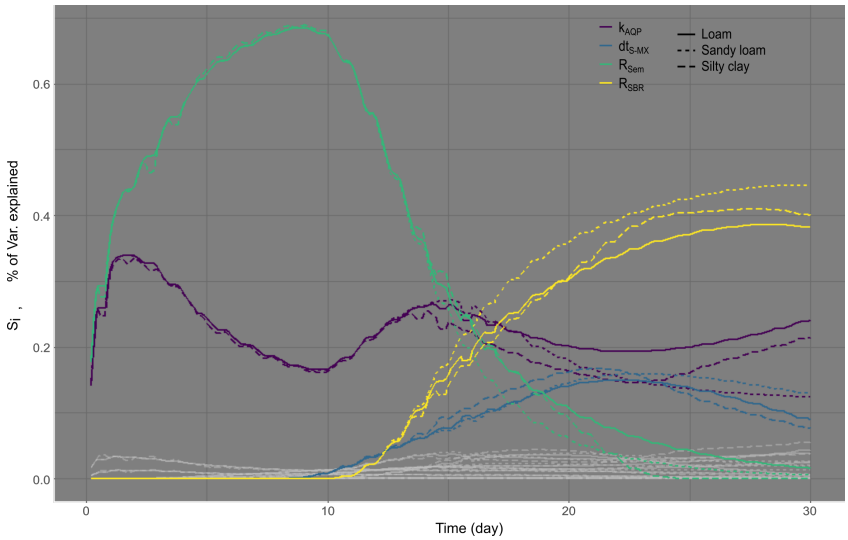


Figure 5.5: Hydraulic anatomy influence on the cumulative root water uptake across the growing period in the three pedo-climatic environments. The three soil types are represented by different dashed patterns. k_{AQP} = the aquaporins contribution to the cell membrane permeability, dt_{S-MX} = delay between the end of suberin deposition in the endodermis cell walls and the beginning of the meta-xylem maturation, R_{Sem} = root radius of the seminal roots, R_{SBR} = root radius of the shoot-born roots.

The impact of the delay between the end of the endodermal suberin deposition and the beginning of the meta-xylem maturation (dt_{S-MX}) started around the 9^{th} day and reached a peak of influence on cumulative root water uptake around the 22^{nd} day. In the sandy loam soil, that peak was observed earlier and higher than for the other tested soil types.

The other input variables were contributing to a lesser extent to the cumulative root water uptake. Among them, the cell wall hydraulic conductivity (k_W) influence reproduced a similar pattern than the k_{AQP} but with a smaller amplitude. The same can be said for the hydraulic conductance of individual plasmodesmata but with an even smaller amplitude.

The lateral root radius (R_{Lat}) influence grew more or less steadily along the growing period but remained low in general. However, R_{Lat} influence was slightly higher after 20 days in the silty clay soil than for sandy loam soil, in addition, the tendency for the loam soil was in between.

Among the small contributing factors to the explained variance, the duration for the deposition of hydrophobic barriers (dt_{HB}) was at its highest around the 20^{th} day.

5.3.2 Soil feedback on water uptake

The soil water content and its hydraulic properties impacted dynamically the way the root system perceived its surroundings. In addition, the phenotype's specificity also influenced the soil hydraulic conductance in their soil zone of influence. The Standard Sink Fraction (SSF) was more impacted in the sandy loam soil than in the other soil types. Figure 5.6 illustrates this phenomenon in an example case. The depth for the preferential water uptake in a uniform soil water potential shifted strongly from shallow to deeper soil layers in the sandy loam soil with the decrease of local soil hydraulic conductivity. This trend was followed for all phenotypes placed in the sandy loam soil. On the contrary, there were only minor modifications to the SSF in the other soil types.

Influence of the hydraulic anatomy on the equivalent conductance ratio

Within the tested climatic scenario, the impact index of the equivalent conductance of the soil zone within roots influence ($\frac{K_{srs}}{K_{rs}} = \lambda$) started decreasing from the 15^{th} day. This index essentially responds to variation of the soil hydraulic conductivity as perceived by the root system. Thus, it shows how the water depletion in the soil zone within roots influence changed the root water uptake.

Beyond day 15, λ showed marked responses across all soil types, though the strongest response was observed in sandy loam ($\lambda < 0.4$ at the end of the growth period; Figure 5.8). The equivalent conductance ratio dropped in the silty clay, and the loam soil, but this decrease gradually diminished more rapidly than in the sandy loam soil. In the silty clay soil, the phenotypes with steeper initial slope were associated with a quicker and deeper plateau than the ones with a more moderate reduction of the impact index.

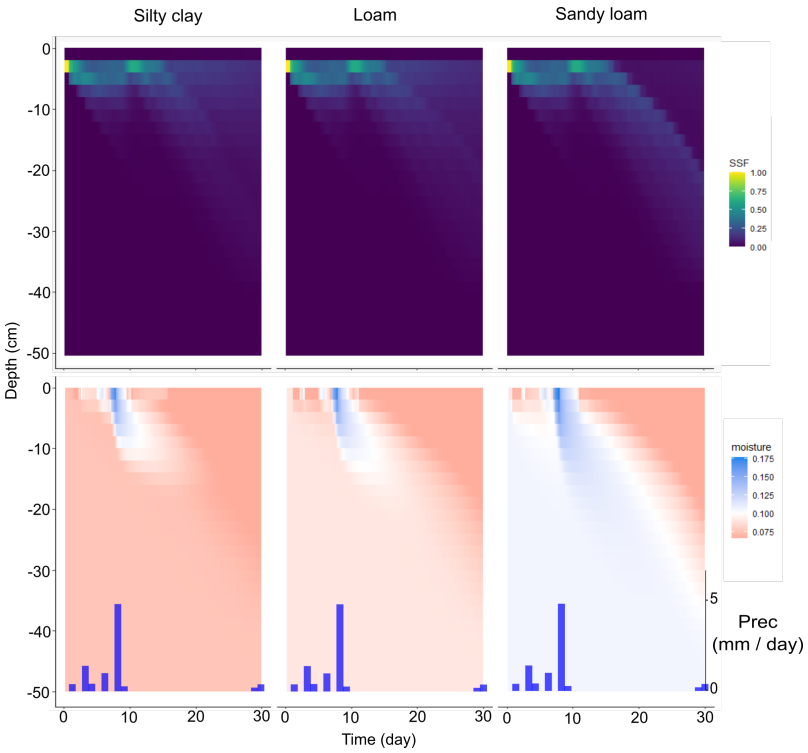


Figure 5.6: Soil water profile records for one example case: the upper panel display the Standard Sink fraction (SSF, -) along the growing period; the lower panel shows the moisture content.

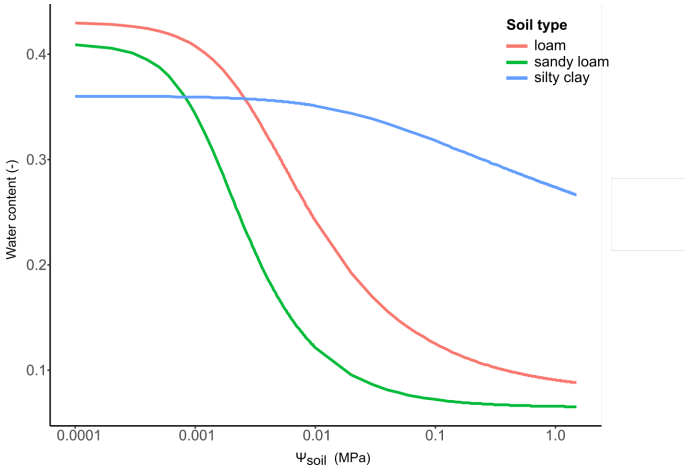


Figure 5.7: Retention curve of the three soil types.

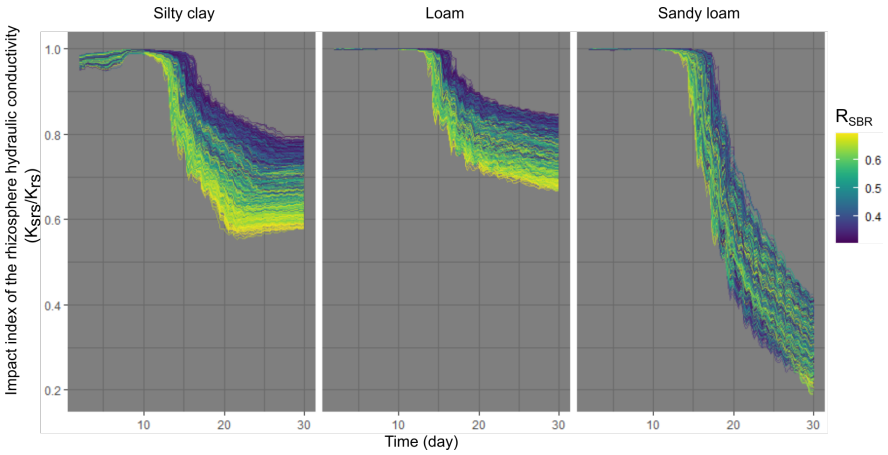


Figure 5.8: Visualization of the conductance ratio between the equivalent soil-root system (K_{srs}) and the one of the root system (K_{rs}) in the three different soil types. The initial root radius of the shoot-born roots (R_{SBR}) was coloured to highlight potential differences between phenotypes.

When we looked at which input variables had a strong "direct effect" on the impact index of the equivalent conductance of the soil zone within roots influence (λ), we observed that the k_{AQP} was the most influential variable (% of variance explained > 0.4 after 20 days). Then, the second input variable to influence the impact index (λ) was the seminal root radius (R_{Sem}). However, it influenced mainly in the silty clay and in the loam soil. In the sandy loam soil, the root radii were less influential, especially from the 18^{th} to the 29^{th} day, where the R_{SBR} explained less than 1% of the total variance of the impact index.

Another soil related observation was that beside their hydraulic properties, the initial water content was different between the soil types. The sandy loam soil had an initial water content higher than the one of the silty clay soil. The initial water content of the loam soil was in between the other two.

5.3.3 Root water uptake efficiency

As we identified key root traits that could explain root water uptake variability, we went one step further and tried identifying the root traits in each soil type that could provide high cumulative water uptake and

high root water uptake efficiency. We also tried to narrow down the distribution of the potential root traits of interest. The **root water uptake efficiency** was calculated as the cumulative water uptake divided by the net root volume.

For each soil type, the phenotype which belonged in the quantile ($> 75\%$) with the highest cumulative root water uptake at the end of the growth period (30 days) were marked. This allowed us to set a minimum threshold at 2.436 $L.plant^{-1}$ for loam soil, at 2.526 $L.plant^{-1}$ for the sandy loam soil, and at 1.430 $L.plant^{-1}$ in the silty clay soil. Then, we marked the phenotypes in the quantile ($> 75\%$) with the highest cumulative root water uptake per net root volume ($L.cm^3$). With these, we set another minimum threshold at 0.1759 $L.cm^{-3}$ for the loam soil, at 0.1777 $L.cm^{-3}$ for the sandy loam, and at 0.1116 $L.cm^{-3}$ in the silty clay soil. The phenotypes included in both categories were then classified as "highly efficient". The distribution of their input was then compared to the other phenotypes.

The distribution of the R_{SBR}, of the dt_{S-MX} and of the k_{AQP} for the "highly efficient" phenotypes were significantly distinct from the input distribution of the other phenotypes (P value < 0.01). In addition, the R_{SBR} optimum within the distribution was soil type dependent (P value < 0.05). Among the efficient phenotypes, the seminal root and the lateral root radius were also soil dependent. The conducted Tukey test showed that efficient phenotypes had different root radius averages depending on the soil types. However, there were no significant differences between the dt_{S-MX} or k_{AQP} for the different efficient phenotypes across the different soil types.

The average value for each trait of the "highly efficient" phenotypes in the three soil types are summarized in Table 5.2. Next, the average input values of the "highly efficient" phenotypes were re-used to simulate 168 new phenotypes, 56 per targeted soil type. Hereafter, these new phenotypes are called "adapted".

The "adapted" phenotypes were virtually replaced in the three same pedo-climatic conditions. They were found again in average above the designated thresholds (Figure 5.9, Table 5.3). However, for their specific environment, no significant difference in terms of cumulative root water uptake nor in terms of cumulative root water uptake per root volume were found between the "adapted" phenotypes. Nevertheless, a significant difference in terms of root volume was observed between phenotypes adapted to silty clay compared to phenotypes adapted to other soil types (p value < 0.05).

We calculated the probability of finding "adapted" phenotypes

Table 5.2: Adapted root traits for efficient soil dependent root water uptake

Variables, Units	**Loam**	**Sandy loam**	**Silty clay**
R_{Sem} (μm)	313	301	294
R_{SBR} (μm)	435	445	419
R_{lat} (μm)	131	129	133
Cv_{Stele} (%)		11.38	
Cv_{MX} (%)		2.14	
dt_{HB} (day)		2.15	
dt_{MX} (day)		2.52	
dt_{S-MX} (day)		0.58	
k_W ($cm^2.hPa^{-1}day^{-1}$)		$2.80E^{-4}$	
k_{AQP} ($cm^2.hPa^{-1}day^{-1}$)		$6.33E^{-4}$	
K_{PL} ($cm^3.hPa^{-1}day^{-1}$)		$6.15E^{-12}$	
P_a (%)		24	

Table 5.3: Performance score of the three "adapted" phenotypes to their specific soil type. The scores were expressed in percentage of finding *in silico* phenotypes (n = 56) above the two threshold lines for the environment they grew up in. If P-value are < 0.05 the probabilities were considered significantly different from each other

Targeted soil type	**Loam**	**Sandy loam**	**Silty clay**
Adapted for Loam	82.14	69.64	41.82
Adapted for Sandy loam	71.43	53.57	18.18
Adapted for Silty clay	66.07	46.43	36.36
Chi-Squared	3.38	6.04	7.78
p-value	0.185	0.049	0.020

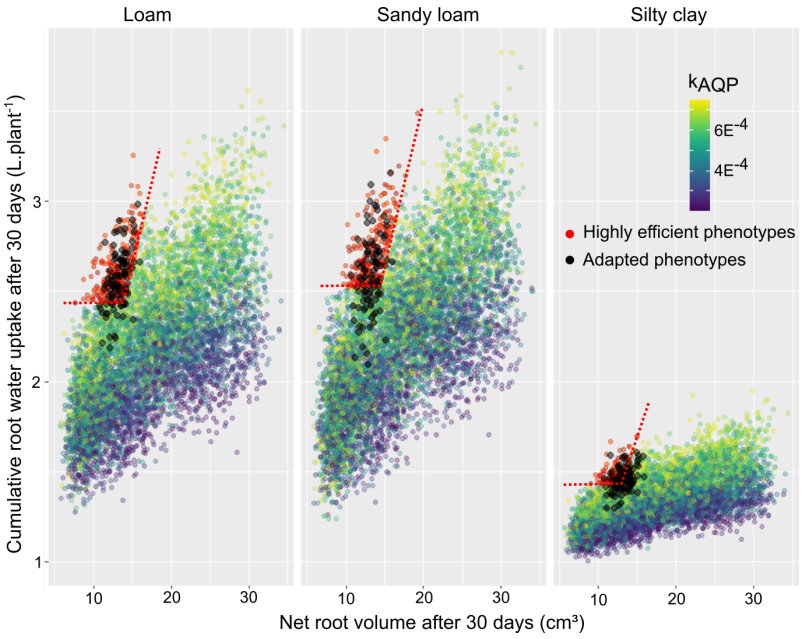


Figure 5.9: Visualization of the total water uptake after 30 days of the "adapted" phenotypes vs. the "highly efficient" phenotypes from the first large sampling. The cumulative root water uptake ($L.plant^{-1}$) and the root volume (cm^3) are displayed to show the total range of variation. The other phenotypes from the first large sampling show the diversity of responses, and the potential overall influence of the k_{AQP} ($cm^2 hPa^{-1} d^{-1}$). The red dashed lines represent the designated threshold value to be considered as "highly efficient".

among the "highly efficient phenotypes" for the specific environment they grew in (Table 5.3). No significant difference was observed between the probabilities of being above the threshold in the loam soil between the different types of "adapted" phenotypes. However, in the sandy loam soil and in the silty clay soil, the probabilities of being among the "highly efficient" were different across the different types of "adapted" phenotypes (Table 5.3).

5.4 Discussion

The sensitivity analysis performed on thousands of *in silico* root systems, in three soil types, showed that local traits related to the hydraulic anatomy of roots have an influence on the global root water

uptake dynamics. Furthermore, the range of variation for these traits were used to narrow down efficient *in silico* phenotypes with high water uptake. They expressed different optimum values within the range of variation in comparison to others. These optimum values also changed, depending on the soil type constraint. The way each individual root trait interacted with each other seems to be more or less consistent across the different soil types. However, by the end of the growing period (30 days), the consistency was less pronounced. We observed that in water deficit, specific root traits expression resulted in different quantities of water taken up in total.

5.4.1 Root anatomy influences on root water uptake

In the tested environments and on a fixed root system architecture, adapting root radius seems to provide a number of leverage points to achieve high cumulative water uptake and high water uptake efficiency. The influence of the seminal root radius on the cumulative water uptake was dominant in the beginning of the growth period and started to diminish as soon as the shoot-born root appeared. Whereas the seminal roots played an important first role at providing the early water needs, once the shoot born roots were able to take up water, they quickly became the primary source of water supply. This hypothesis is supported by the sudden increase of root water uptake rate just after the 9^{th} day. However, the shoot-born root radius influence on the cumulative water uptake outperformed the seminal root radius influence only 5 to 6 days after their emergence, thus, compensating almost all the variability induced by the seminal root radius.

Yet, the sudden change of water uptake which coincided with the appearance of shoot-born roots reveals that their sets of hydraulic conductivities enable them to take up larger amounts of water and more rapidly than the seminal roots. Their large radii were related to a high number of xylem vessels which then translated into higher axial hydraulic conductance, more so closer to the tip, in comparison to other root types which had smaller and fewer xylem vessels. This difference in terms of axial hydraulic conductance played a determining role on the water uptake rate. More so, 5 to 6 days after the emergence of shoot-born roots, when their meta-xylem started to mature, it coincided with the drop of the impact index for the hydraulic conductivity of the soil zone with roots influence, and a fast drying of the shallow soil layers. In addition, it suggests that shoot-born roots were able to take up a high proportion of the water along root segments which had suberin deposition but mature meta-xylem vessels.

These observations on the shoot-born roots water uptake dynamics are also shared by experimental study (Ahmed et al., 2018).

In our study, the axial hydraulic conductance seems to be more sensitive to root diameter than to the ratio between xylem and stele area. A potential cause is that the settings for allometry strongly influenced anatomical traits (Chapter 4, Figure 4.6). It may explain the proportionally small influence of the coefficient of variability for the ratio between xylem and stele area. Here, we hypothesize that the proportion of the cross-section occupied par the stele or the xylem proportion in it would be more influential if the tested range of root radius was smaller.

5.4.2 Subcellular hydraulic properties influence on the root water uptake

The sensitivity analysis showed that, root radius aside, the contribution of aquaporins to the cell membrane hydraulic conductivity was a highly influencing variable. Dynamically, the level of influence brought by this variable changed periodically as the plant grew, which would imply different levels of combination of events for the k_{AQP} to be more influential. A possible explanation is that the first peak of influence happened when seminal roots were actually taking up most of the water, then as the lateral root counts increased, the seminal root function shifted toward hydraulically lifting the water. The second peak, around the 15^{th} day, happened when the shoot-born roots were potentially the largest contributors to the radial flux. The following decrease could be attributed to the soil drying in the shallow layers, which impeded large fractions of shoot-born roots to take up water as they were closer to the surface.

At the root cross-section level, the k_{AQP} was shown previously to be the most influential factor before suberin deposition (Chapter 4). Again, the high k_{AQP} influence was observed, but this time at the global scale. This would suggest that most of the water flow occurred where the root segments did not yet display endodermal suberin deposition. If water uptake was primarily located after suberin deposition, we would have observed a greater influence of hydraulic conductance of individual plasmodesmata, which was not the case. In addition, when we observed the radial water fluxes per segment length normalized by the total water uptake, the so-called standard uptake density (SUD), as a function of the root segment age, most of the radial fluxes occurred when the roots were young. To illustrate

this phenomenon, Figure 5.10 shows an example case of the standard uptake density for one root system after 30 days.

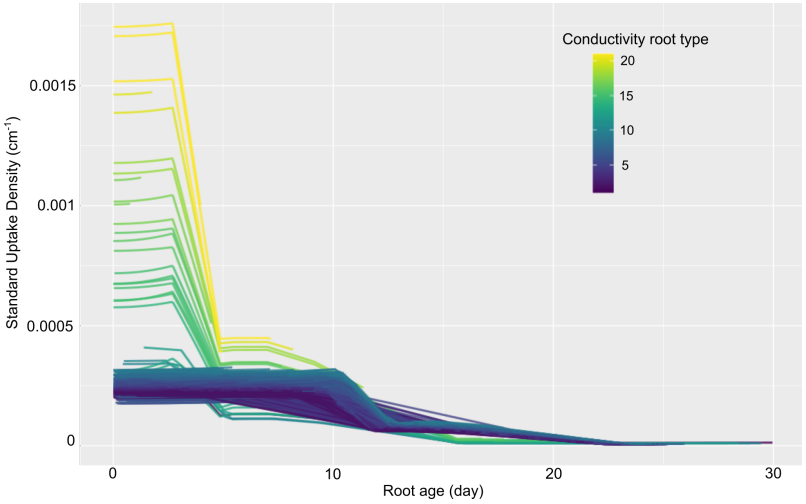


Figure 5.10: The standard uptake density (SUD, cm^{-1}) of one root system displayed as a function of the root segment age. Each line corresponds to one root and the colour conveys the root conductive typology. The root conductive typology goes as follow: 1 = tap root; 2 to 10 = lateral roots; 11 to 13 = basal roots; and > 13 = shoot-born roots

5.4.3 Timing effect

Once the zero-order roots started to be long and mature ($\pm$ 7 to 8 days), a reduced delay between the suberin deposition and the beginning of meta-xylem maturation increased their water uptake. The effect of this delay on the cumulative root water uptake was increasing as the shallow soil layers got depleted of their available water. This suggests that root systems with reduced delay have a better access to the deeper soil water resources. In addition, it has a direct positive influence on the equivalent root-system hydraulic conductance.

However, the positive impact of this delay was challenged in the silty clay soil. Indeed, in that soil type, as all variables that had a strong positive effect on the root water uptake rate until the 20^{th} day, these variables also had the inconvenience of quickly exhausting the soil of its available water. In this particular scenario, soil hydraulic

conductivity limited water uptake by shorter shoot-born roots, reducing their share of the water uptake. On the opposite, the proportion of water was then mostly taken up by the deepest seminal roots. After the 22^{nd} day, the shoot-born roots grew deeper and were then able to take up more water again.

5.4.4 Drainage and water storage capacity

The silty clay soil is thought to be the only tested pedo-climatic scenario where plants experienced strong drought stress. Although, for the sandy loam, the impact index of the hydraulic conductance of the soil zone within roots influence was heavily impacted, there was still water available for the plant at deeper depth. The rearrangement of the standard uptake fraction due to shallow dry areas which lowered drastically the local soil hydraulic conductance reshaped the way the plant absorbed water.

5.4.5 Engineering root traits to optimize water uptake and efficiency

Using the virtual phenotyping pipeline for root hydraulic traits, we were able to estimate potential optimum traits depending on specific pedo-climatic constraints. These early *in silico* results suggest that root radius and subcellular hydraulic properties are important traits to target when looking for adapted traits in specific environments. These results are likely to be affected by some model assumptions.

The root radii were directly related to the root volume, which was here used as a proxy for the metabolic cost. These root radius variables were then given an additional weight when evaluating the root water uptake efficiency. This could explain why among the "highly efficient" phenotypes, the different root radii were the only root traits that were soil dependent. Changing the root cost function when evaluating the root water efficiency could have changed the outcome when we classified the overall water uptake of the different phenotypes. However, when it comes to quantifying the metabolic cost of a root, further research is needed. Indeed, although we removed the aerenchyma volume from the initial estimation of the root system volume (Schneider et al., 2017), we did not take into account the cortex cell size (Chimungu et al., 2014a) which could also potentially have a impact on the global carbon cost.

The extra simulations, did not show that "adapted" phenotypes take up water differently in their designated environment. Slight differ-

ences in terms of probability of being above the designated threshold were found in the sandy loam and in the silty clay soil. However, the overall water uptake was not significantly different from each other in either of the three soil types. Further investigations with higher sampling matrix size should then be able to provide insight about the interconnection between the different root traits. Nonetheless, these "adapted" phenotypes expressed good water uptake efficiency and they still manage to take up a high amount of water in total.

The way each individual input variable interacted with each other seems to be more or less consistent across the different soil types. However, by the end of the growing period, the consistency was less pronounced. We observed that in water deficit, specific root traits expression resulted in different water uptake amount.

5.5 Conclusion

We associated models in a structured network to better understand which root traits at the root cross-section level and within which range could be put to use to develop strategies that would increase crop water uptake in specific pedo-climatic environments.

Within the framework of our analysis, the root radius of zero-order roots were the most influencing variables over the root water uptake of *in silico* phenotypes. The contribution of aquaporins to the cell membrane permeability also played an important role in terms of root water. This adds up to the theory that young and not yet suberized root segments achieve the main root water absorption function. In addition, the shoot-born roots with their high axial hydraulic conductance, even close to the root tip, provided highly conductive roots that have the ability to take up large amounts of water.

Another variable that influenced the root water uptake dynamics was the delay between the suberin deposition and the maturation of the meta-xylem vessels. It affected the equivalent hydraulic conductance which consequently led to higher root water uptake rate when water was within reach.

The way anatomical traits, subcellular hydraulic properties and maturation rates contributed to the cumulative water uptake was dynamically changed along the growth period. Their impact scaled-up at the root system scale and affected the local soil hydraulic conductivities as well. The local soil hydraulic conductivity was related to the water depletion. These reductions of local soil hydraulic conductivity changed the standard sink fraction. This phenomenon was increased

in the sandy loam soil which was the most conductive soil type included in the analysis. Once the soil dried over several depth layers, the impact of all major input variables to the cumulative water uptake were then soil dependent.

The virtual phenotyping pipeline for root hydraulic traits enabled the estimation of potential optimum traits depending on pedo-climatic constraints. These early *in silico* results suggest that root radius, subcellular hydraulic properties and maturation rates are important traits to target when looking for adapted traits in specific environments.

5.6 Appendix

5.6.1 Influence of the hydraulic anatomy on the root water uptake rate

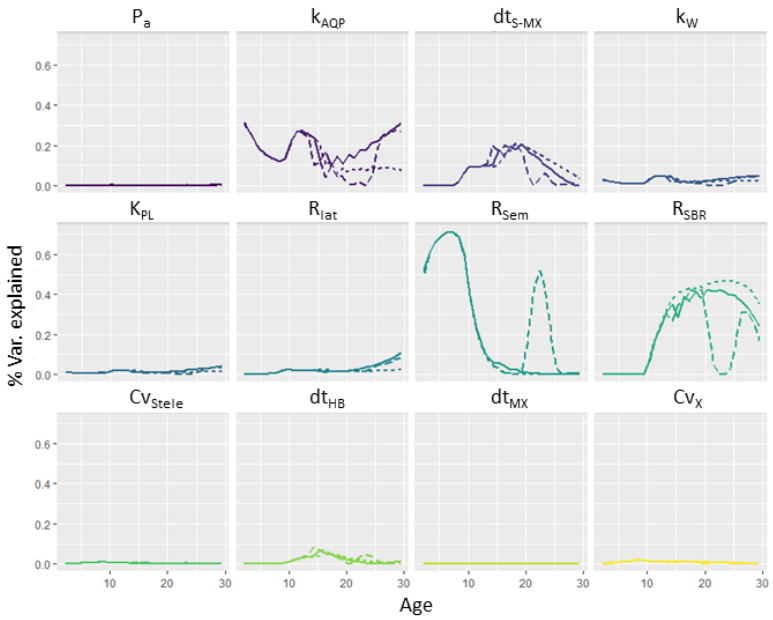


Figure 5.11: Hydraulic anatomy influence on the root water uptake rate during the growing period in the three pedo-climatic environments. The three soil types are represented by different dashed patterns (—— = Loam; - - - sandy loam; – – silty clay). P_a = cortical aerenchyma proportion, K_{AQP} = the aquaporins contribution to the cell membrane permeability, dt_{S-MX} = delay between the end of suberin deposition in the endodermis cell walls and the beginning of the meta-xylem maturation, k_W = the cell walls conductivity, K_{PL} the hydraulic conductance of individual plasmodesmata, R_{lat} = root radius of the lateral roots, R_{Sem} = root radius of the seminal roots, R_{SBR} = root radius of the shoot-born roots, Cv_{Stele} = coefficient of variation for the ratio between stele and cross-section area, dt_{HB} = duration of the establishement of a hydrophobic barrier deposition and the delay between two stages level of hydrophobic barriers, dt_{MX} = duration of the maturation of the meta-xylem, Cv_{MX} = coefficient of variation for the ratio between the xylem and the stele area.

5.6.2 Shoot water demand

The shoot water demand was estimated with the Penman-Monteith framework (Allen, and FAO, 1998). The required meteorology data were provided with the NASA POWER package which gives access to global meteorology, climatology and surface solar energy upon any geographic coordinates (Sparks, 2018). The estimated standard evapotranspiration (ET_0) was derived as:

$$ET_0 = \frac{0.408\,\Delta\,(R_n - G) + \gamma\,(\frac{900}{T+273})\,u_2\,(es - ea)}{\Delta + \gamma\,(1 + 0.34\,u_2)} \tag{5.5}$$

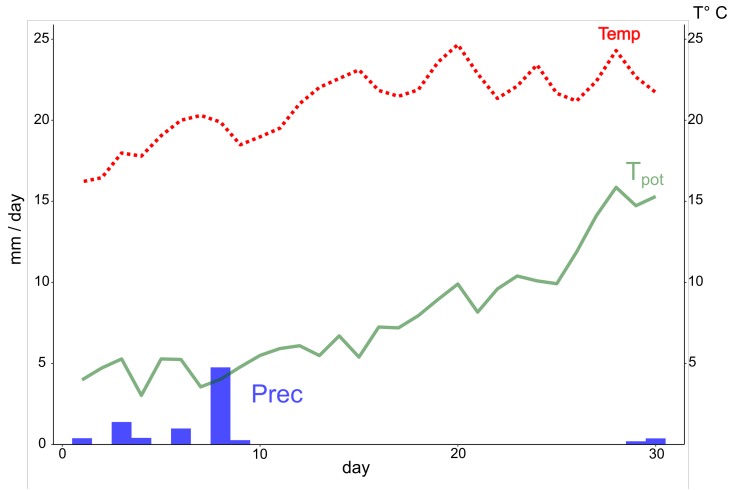


Figure 5.12: Weather during the 30 days of the simulation in Palermo (Italy) for the three soil types during May - June 2018. Prec = Precipitation (mm/day), T_{pot} = potential shoot water demand (mm/day), and Temp = temperature (^oC)

where ET_0 is the reference evapotranspiration ($mm.day^{-1}$), R_n is the net radiation at the crop surface ($MJ.m^{-2}day^{-1}$), G is the soil heat flux density which was assumed to equal 0 when the time step between estimation is on the order of the day ($MJ.m^{-2}day^{-1}$), T is the mean daily air temperature at 2 m height (^oC), u_2 is the wind speed at 2 m height ($m.s^{-1}$), es is the saturation vapour pressure (kPa), whereas ea is the actual vapor pressure (kPa), Δ represent the slope of the vapor pressure curve ($kPa.^oC^{-1}$), and γ is the psychrometric constant ($kPa.^oC^{-1}$).

Once the ET_0 was estimated, we derived the crop coefficient (K_c) from Campos et al. (2017) with the equation:

$$K_c = 1.1\,(1 - e^{(-(GDD/620)^3)} + 0.1$$

where GDD are the "Growing Degree Day" with a base temperature of 10 ^oC. This fitted function is valid until $\pm 700 GDD$.

Therefore, the potential shoot water demand $(T_{pot}) = K_c \cdot ET_0$.

5.6.3 Soil hydraulic properties in root vicinity

Radial flow from or to a root through a soil resistance.
Following van Lier et al., 2006, the half distance between roots can be expressed as:

$$R_{m,j} = \sqrt{\frac{1}{\pi RLD_j}}$$

where RLD_j is the root length density in the j-th layer of the soil according to the depth axis.
The ratio between the half distance and the root radius itself is called ρ_j:

$$\rho_j = \frac{R_{m,j}}{r}$$

and used in the next equation to set the dimensionless parameter B which take into account the geometrical disposition of the roots in a soil layer.

$$B_j = \frac{2(1-\rho_j^2)}{-2\rho_j^2(ln\rho_j - 1/2) - 1}$$

The soil properties were obtained via the Mualem–van Genuchten parameterization (Van Genuchten, 1980), where the soil saturation degree (Θ) was computed through the following equation:

$$\Theta = (\frac{1}{1 + |\alpha\,\Psi_{bulk\,soil,\,j}|^n})^m$$

where $m = 1 - 1/n$. And the empirical soil hydraulic parameters are α (L^{-1}), n and λ.

$$K_{soil} = K_{sat} * \Theta^{\lambda}(1 - (1 - \Theta^{\lambda/m})^m)^2$$

where K_{sat} $(L\,d^{-1})$ is the saturated soil hydraulic conductivity. When this soil conductance is associated in series with a root radial conductivity, the equivalent conductance is (Meunier et al., 2018a):

$$K_{i,\,eq} = \frac{k_r * K_{soil} 2\pi\, l\, r\, B}{B * K_{soil} + r\, k_r}$$

Then, the equivalent hydraulic conductance of the soil and root is converted towards the conductivity values to be incorporated into the analytical solution of the water flow:

$$k_{r,\,eq} = \frac{K_{i,\,eq}}{2\pi\, l\, r}$$

Therefore, by changing the hybrid analytical-numerical method for solving water flow in hydraulic architecture of Meunier et al., 2017b, we get:

$$J_{r,eq,i} = 2{*}\kappa_{eq,i}{*}\tanh\left(\frac{\tau_{eq,i}.l_i}{2}\right){*}\left(\Psi_{bulk\,soil} - \left(\frac{\Psi_{x-1,i} + \Psi_{x,i}}{2}\right)\right) \quad (5.6)$$

where $\kappa_{eq,i} = \sqrt{2\pi r_i * k_{r,eq,i} * k_{x,i}}$ and $\tau_{eq,i} = \sqrt{\frac{2\pi r_i k_{r,eq,i}}{k_{x,i}}}$ are hydraulic-specific root segment properties including the soil zone within their influence.

Thus, by rearranging the equation of the maximum root water uptake:

$$RW_{pot} = \Delta\Psi * K_{rs} \quad (5.7)$$

where $\Delta\Psi$ is the largest possible water potential difference between a wet and uniform soil water profile, and the plant collar. The hypothesis that we took is that, in this scenario, soil water is at -0.01 MPa and the leaf water potential is at -1.5 MPa. Which corresponds to a well-watered soil and high evaporative demand. The water potential within the plant collar was approximated as the leaf water potential. This would hold true if shoot hydraulic conductance was very high and the plant rather small.

The equivalent soil-root system hydraulic conductance:

$$K_{srs} = \frac{\sum J_{r,eq,i}}{\Delta\Psi} \quad (5.8)$$

when all $\Psi_{bulk\,soil}$ values are equal to -0.01 MPa.

In the previous Chapter, we created a virtual phenotyping pipeline for root hydraulic traits. Although, we knew that the root system architecture should have significant impact over the root water uptake performance, we only worked with a fixed root system architecture. However, including the whole spectrum of root system phenotypic diversity would increase too much the number of plants that should be tested and not feasible anymore, computationally speaking.

Thus, we wanted to select plants that should be locally adapted to specific pedoclimatic conditions to reduce the scope of our analysis. From that, we had the chance to work with (*Zea mays*) landraces from very distinctive locations. Theoretically, they should express a level of local fitness adaptation. As such, we thought that it could be a great entry point to test if our models could show the water uptake dynamics of theses *in silico* plants, and perhaps show how these plants are locally adapted (or at least hydraulically).

IN SILICO EVALUATION OF MAIZE LANDRACES WATER UPTAKE IN THEIR OWN NATIVE PEDO-CLIMATIC CONDITIONS

6

This chapter is a practical application of the Virtual Phenotyping pipeline for Root hydraulic traits that we developed previously in Chapter 5. Therefore, the material and methods section are very similar.

This chapter is an edited version of a scientific article in preparation, entitle as:

> Adrien Heymans, Chloee McLaughlin, Ruairidh Sawers, and Guillaume Lobet. *in silico* evaluation of root trait adaptations of maize landraces to their native pedo-climatic conditions. (in progress)

LANDRACES are agronomically adapted plants to their local pedo-climatic conditions, and they are thought to have very different root anatomy and root hydraulic properties from place to place due this local adaptation. However, the contribution of the root system hydraulic architecture to the local fitness of such plants is still poorly understood. A better understanding of the underlying properties could be used to develop strategies that would increase crops water uptake under specific pedo-climatic environments.

Here, we used the Virtual Phenotyping pipeline for root hydraulic traits (Hydraulic Viper) to test the hypothesis that landraces have a set of root traits adapted for their native pedo-climatic conditions. We parameterized eight different Mexican maize (*Zea mays*) accessions based on a pot experiment from which the root system architectural traits and root anatomies were extracted from root scans and laser ablation tomography, respectively. The soil texture properties (clay, silt and sand fractions), and the meteorological data of the different

geographic regions were acquired from *open access* resources. This information was used to re-create the virtual pedo-climatic environments of the location of origins. In total we simulated 4127 root systems and evaluated their water uptake dynamics in the eight environments of origins.

Among the *in silico* plants, the ones with fast growing seminal roots were able to take up more water than the others in most of the tested environments. However, the root systems that took up the largest amount of water were generally the root systems with the minimum efficiency (defined as the cumulative transpiration per unit of root volume). It was especially true when the *in silico* plants were limited by the potential evaporative demands driven by the plant growth and the climatic conditions. The only major exceptions were in the most constraining environment. In that environment, the landrace with the fastest growing basal roots and the fewest amount of shoot-born roots were the one that transpired the most in total and was also the most efficient ones.

The Hydraulic Viper allowed us to test the root hydraulic anatomy of *in silico* landraces and evaluate their water uptake dynamics in their environments of origin. The different sets of local root traits resulted in different water uptake dynamics which were, surprisingly, weakly related to their native pedo-climatic conditions. Further testing, feedback from field experiments, and better integration of other root functions are needed to evaluate the fitness of root systems hydraulic architecture in specific pedo-climatic conditions.

6.1 Introduction

Recently, the concept of non-unique, site-specific phenotypes linked to high water uptake efficiency and high root water uptake performance[1] emerged in the scientific literature (Tardieu et al., 2017). First, it started with the idea of a hypothetical root-ideotype, referenced as the best possible phenotype which optimizes soil resources acquisition in common environments (Lynch, 2013). The features of this root-ideotype envisioned by Lynch (2013) was mostly architecture oriented, with steep, deep, and cheap roots. Then the concept of eco-ideotype tried to balance the supremacy of this previous phenotypic state, with the fact that one well fitted phenotype for one environment may not be the best in another (Tardieu, 2012). Finally, not far from

[1] **Water uptake performance** refers as the cumulative root water uptake in comparison to other plants growing in the same environment

the eco-ideotype concept, Tardieu et al. (2017) reshaped it to the non-unique site specific ideotypes with a good trade-off between the transpiration potential and the soil water depletion risk. The "benefit-risk" approach implies a profound knowledge of the pedo-climatic condition of the crop site to be able to choose phenotypes that will express the right state of phenes at the right time.

Therefore, being able to predict what would be the right set of traits along the growing period requires prescient capabilities. Fortunately, landraces are thought to have adapted traits to their native pedo-climatic conditions, as they are the fruit of long term selection in specific locations (Newton et al., 2011). Furthermore, they should also be nutrient use efficient as they are linked to low input farming practices, which is a requirement for crop sustainability (Newton et al., 2011). Thus, we could phenotype landraces and identify key root traits which would be beneficial in scenarios that are similar to the location of origins of these lines. To do that, we would need to evaluate the different plants root water uptake in these scenarios.

Alternatively, it could be achieved through the simulating of possible scenarios and evaluating within multiple *in silico* plant water uptake dynamics which ones express good trade-off in terms of water uptake *versus* soil water depletion. While measuring the root water uptake dynamically on thousands of plants that are composed of thousands of roots is, in practice, not yet feasible, computational models can be used to bypass experimental constraints and explore complex dynamic systems from conceptual knowledge. Most models simulate part of a complex system, but their association into structured networks can be used to determine key phenomena that were hidden when studied alone (Passot et al., 2019; Rellán-Álvarez et al., 2016). The recent development of a model network into a virtual phenotyping pipeline (Chapter 5) allowed us to estimate root water uptake dynamics by solving the root system hydraulic architecture and quantifying macro-hydraulic properties in different pedo-climatic conditions. These macro-hydraulic properties define where and how much water can be absorbed and are soil dependent (Couvreur et al., 2012; Meunier et al., 2020).

Here, we used the Virtual Phenotyping pipeline for Root Hydraulic traits (Hydraulic ViPeR) to estimate the root water uptake dynamics of eight maize (*Zea mays*) Mexican accessions. The evaluation of their cumulative root water uptake was done in the eight typical pedo-climatic environments corresponding to their eight locations of origins. The *in silico* landraces were parameterized from a pot experiment

where the eight landraces grew in a greenhouse, and the virtual pedoclimatic environments were reconstructed from open access resources.

6.2 Materials and methods

6.2.1 Plant materials

To test the hypothesis that landraces could potentially be adapted to their local hydraulic environment, we selected eight Mexican maize ascensions from very contrasted environments and geographic regions (Figure 6.1, Appendix Figure 6.10). These hereafter so-called "landraces" are CIMMYT maize accessions (Scott et al., 2020) that were selected as representative of their race (Genetically and/or morphologically related plants from the same area).

The landrace *Conico* and *Palomero Toloqueno* are both known to grow in high elevation sites, in soil with low phosphorus availability, and with an early planting month (March). The landrace *Reventador*, *Jala*, and *Tabloncillo* are geographically close and globally rainfed, but the area of origin of the landrace *Reventador* has a low elevation. The landrace *Gordo* comes from the Norden Mexican region and has one of the driest environments of origin. Whereas, the landraces *Nal Tel* and *Zapolate Chico* come from the most tropical regions, with hot and humid environments. From the principal component analysis, which was done prior to this study, the location of origin of the landrace *Nal Tel* clustered far from the other landrace on the first PCA axis (Figure 6.10 in appendix).

From the experimental root systems, we also extracted root anatomical traits. For each of the landraces, from 8 to 12 images of the seminal roots cross-section were gathered with the laser ablation tomography technique. From these pictures, with ImageJ, we measured the area of selected cell tissues: the area of the root cross-section (RXA), the area of the stele (TSA), the area of all the xylem vessels (XVA), and the area of the aerenchyma lacuna (AA). Then, we calculated the ratio between the stele area and the cross-section area (TSA/RXA) as well as the one between the stele area and the xylem (XVA/TSA). From that, we estimated the coefficient of variation of these parameters from a referential based on the root radius (% of variation from the referential). The referential values resulted from a typical root where all anatomical traits are derived from the root radius of the studied root and the allometric relationships established previously (Chapter 4). These relationships were not specific to these eight lan-

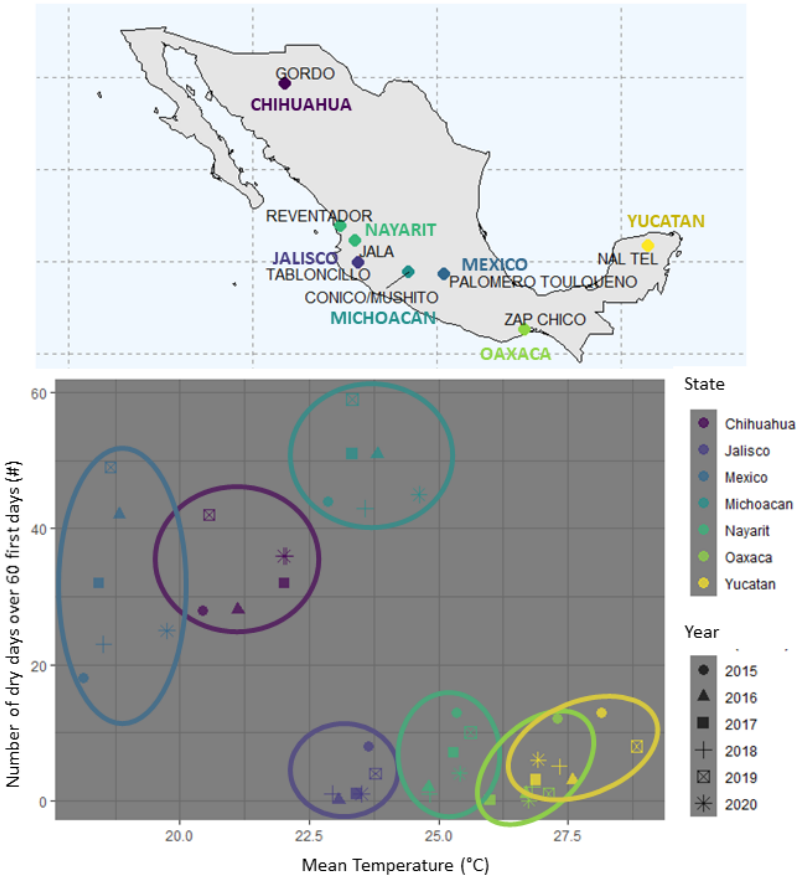


Figure 6.1: Origins of the eight lines selected in the Multi-parent Advanced Generation Inter-Cross (MAGIC) accessions (Scott et al., 2020).

draces. These coefficients and parameters were then used to generate root cross-sections from their root radius (Figure 6.2).

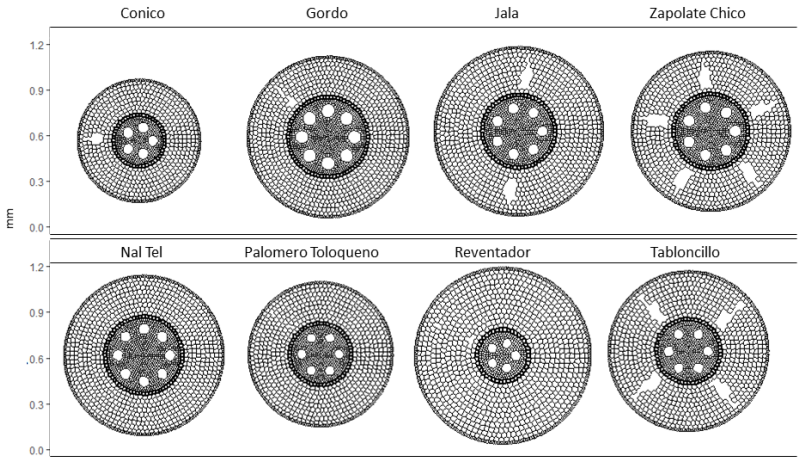


Figure 6.2: *in silico* replicates of the seminal roots of the MAGIC landraces.

6.2.2 Virtual pedo-climatic environments

To create a unique environmental constraint specific to each one of the eight native regions, we downloaded soil and meteorological data with the gps coordinates of the different location of origins from different web open-access resources.

The clay, silt, and sand fraction for each soil were gathered from the website soilgrids.org. The virtual soils of origin were approximated to be constituted with only one media of 2 m depth. We used the module Rosetta (Schaap et al., 2001) included in Hydrus-1D software (Šimůnek et al., 2008) to estimate the soil hydraulic parameters of each soil type (Table 6.1).

The meteorological data were acquired from the NASA Power project (Sparks, 2018). The data from the year 2020 were the one used to set the virtual climatic conditions. As in Chapter 5, the estimation of the shoot water demand was done with the Penman-Monteith method (Allen, and FAO, 1998) and the crop coefficient derived from Campos et al. (2017). This method allowed us to take into account the canopy growth as a function of the number of day

Table 6.1: For each environment, the soil hydraulic parameters were derived from the neural network prediction tool of Hydrus-1D. H = The elevation from the sea level is in meters. The abbreviations are: Θ_r = The residual soil water content (-), Θ_s = Saturated soil water content (-), α = Parameter in the soil water retention function (cm^{-1}), n = Parameter in the soil water retention function (-), Ks = saturated hydraulic conductivity ($cm.d^{-1}$), l = tortuosity parameter in the conductivity function (-), Ψ_{soil} = initial soil water potential (cm).

State (founder)	**Lat.**	**Lon.**	**H**	Θ_r	Θ_s	α	**n**	**Ks**	**l**	Ψ_{soil}
Chihuahua (Gordo)	29,65	-108,25	2141	0,0455	0,3848	0,0309	1,3977	36,34	0,5	-368.1
Jalisco (Tabloncillo)	19,97	-104,27	1355	0,0893	0,4515	0,0184	1,2847	8,47	0,5	-454.6
Mexico (Palomero)	19,30	-99,60	2597	0,049	0,3855	0,028	1,3862	29,77	0,5	-389.8
Michoacan (Conico)	19,42	-101,56	2483	0,0673	0,4089	0,0127	1,445	7,8	0,5	-602.9
Nayarit (Jala)	21,11	-104,45	1098	0,053	0,3926	0,0116	1,4774	14,31	0,5	-753.9
Nayarit (Reventador)	21,95	-105,22	13	0,08	0,4432	0,0082	1,5044	12,39	0,5	-1018.6
Oaxaca (Zapolate)	16,32	-95,24	50	0,0826	0,4279	0,0183	1,323	5,07	0,5	-392.5
Yucatan (Nal Tel)	20,85	-88,52	30	0,0911	0,461	0,0168	1,2959	9,81	0,5	-515

degrees (Base temperature of $10\,^0C$). Shoot growth was therefore site dependent. Since we only had information about the root system of the different landraces, the same shoot water demand properties were shared with all the plants grown in the same environment.

6.2.3 Experimental design

For each landrace, we wanted to have well replicated references in their own environment of origin. Thus, we simulated each landrace in their own environments ± 300 times. Then we simulated each landrace ± 30 times in all the other virtual environments.

The subcellular hydraulic properties, and the maturation rates (meta-xylem maturation, hydrophobic barrier depositions and interval between these depositions) that were not measured experimentally, were sampled from a smaller range than in Chapter 5 (Table 6.6 in appendix). The small ranges were selected to reduce the number of replicates needed to have a valid estimation of the landrace effect. The sampling method followed the pseudo-random techniques of Saltelli et al. (2010) within uniform distribution for all parameters.

6.2.4 Statistical analysis

All statistical analyses were conducted in R (R Core Team, 2018). The different functions used to sample pseudo-randomly the input variables were from the package *"sensitivity"* (Iooss et al., 2021).

The ANOVA conducted to estimate the differences of root water uptake between the landraces in each native environment was achieved with the function *'aov'* from the *"stats"* package. The selected models took into account all the root traits variables that were sampled. These root traits were: the contribution of aquaporins to cell membrane permeability, the cell wall hydraulic conductivity, the hydraulic conductance of individual plasmodesmata, the delay between the end of the endodermal suberization and the beginning of the meta-xylem maturation, the duration of the maturation of the meta-xylem, and the duration of the maturation of hydrophobic deposition. Then, to compare groups, the function *'TukeyHSD'* was used.

6.3 Results

In total, 4217 maize root systems were generated (Figure 6.3), which represented around 510 *in silico* root systems for each landrace. For

each one of these root systems, the root water uptake dynamic was simulated in one of the eight possible pedo-climatic conditions.

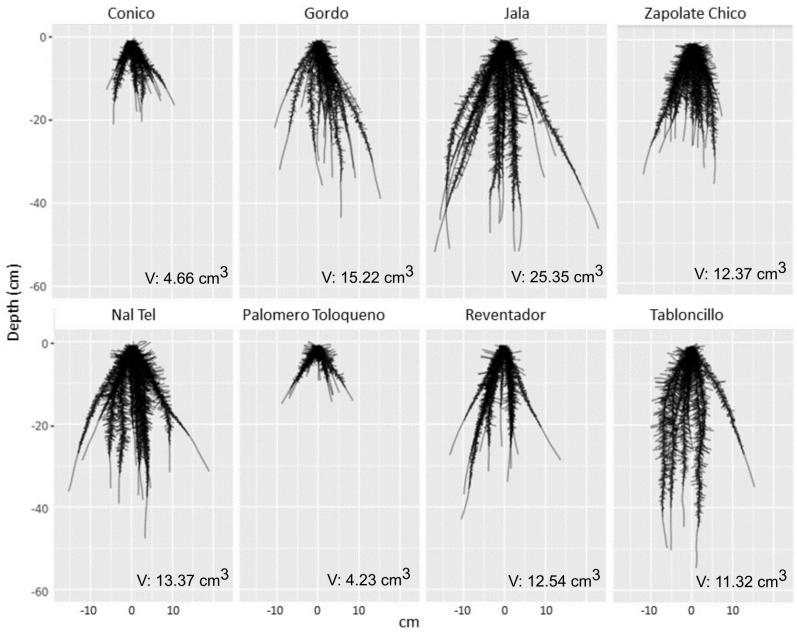


Figure 6.3: Example of generated root system architectures for the MAGIC landraces. V = average root volume (cm^3)

The simulated cumulative root water at the end of the 30 day growing period were locations and landraces dependent (P value $<$ 0.01). The root water uptake rate of *Tabloncillo* was the fastest and especially early on of all, in all the tested environments. The following landraces to take up early high soil water were *Nal Tel*, then *Jala* and *Zapolate Chico* (Figure 6.4). The two landraces which had the lowest root water uptake rates on average, were *Conico* and *Palomero Toloqueno*.

In some instances, some *in silico* phenotypes were limited by their potential evaporative demands driven by the shoot growth and the climatic conditions. If so, their transpiration rates were identical as their root water uptake could only be less or equal to the potential evaporative demands. For example, in Mexico after 20 days, almost none of the root systems were the limiting factor to the plant tran-

spiration rates. On the opposite, in Michoacan where *Conico* is from, none of the *in silico* phenotypes were limited by the shoot water demands along the growing period. This virtual environment was the most restrictive one for the root water uptake.

6.3.1 Soil feedback

The pedo-climatic conditions were different from place to place. There were only four locations where the root water uptake was reduced due to the decrease of soil water content which lowered the hydraulic conductivity of the soil zone within roots influence. In the four other locations, the rainfall events saturated the soil profile more than it was in its initial state (Table 6.1). Figure 6.5 shows example cases of soil water profiles recorded per location along the 30 days.

Among the virtual environments, the conductance ratio between the "soil-root system" and the "root system" alone (K_{srs}/K_{rs}) dropped in four of them. This conductance ratio represents the ratio between an "actual conductance" of the system including the soil zone within root influence opposed to the root system hydraulic conductance in a wet soil. The reductions of the soil hydraulic conductance were environment dependent (Figure 6.6). Although, both in Chihuahua and in Michoacan the global trends had similar patterns, the overall amplitude of the reduction was greater in Michoacan. Both shared the fact that some rainfall events occurred around the 17^{th} day, which re-watered the shallowest soil layers (Figure 6.5). At the same time, the impact index of the hydraulic conductance of the soil zone within roots influence re-increased for all *in silico* plants. The impact index for *Conico* and *Palomero Toloqueno* recovered faster and better than for the other landraces, which remained with a lower impact index. However, the impact index dropped back after these rainfall events. In Chihuahua, the rainfall events at the end of the growing period were also coordinated with a recovery of the impact index for all *in silico* plants.

Another similarity between both Michoacan and Chihuahua was that the drop of the impact index happened around the 10^{th} day. The small differences between both were that in the Chihuahua environment, the first drop occurred earlier for the landraces *Tabloncillo*, and then *Nal Tel*, followed by the others. Whereas, in Michoacan, they all dropped around the same time with the exception of *Palomero Toloqueno* and *Reventador* which had their impact index reduction after the other landraces.

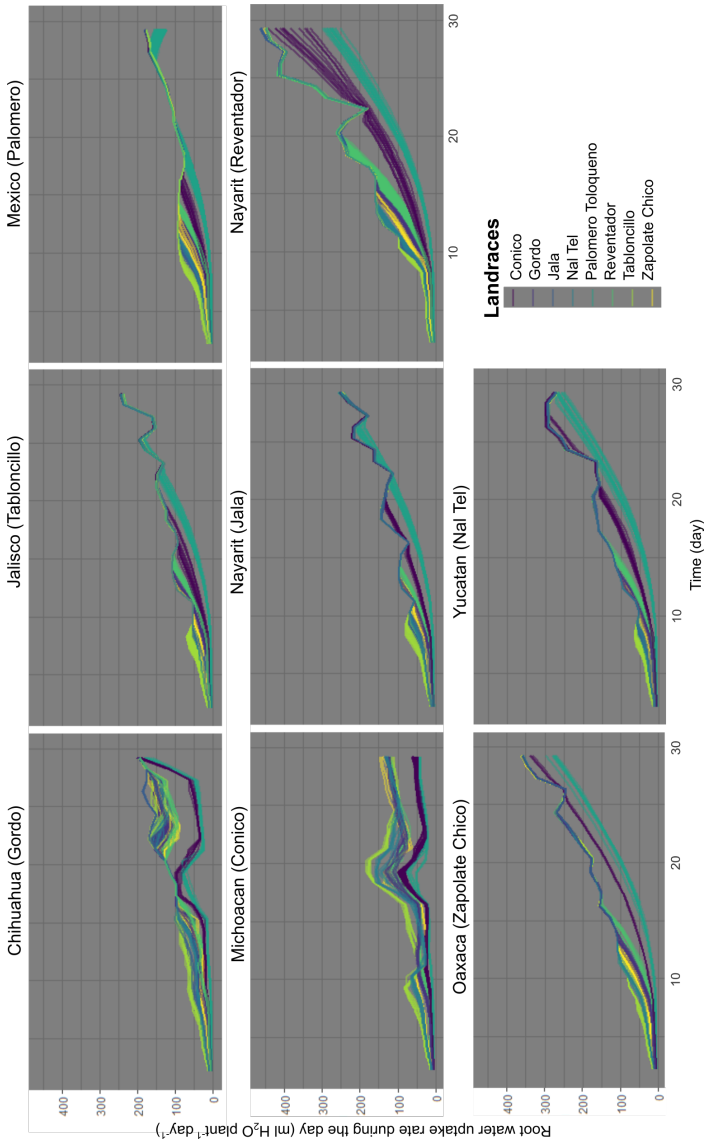


Figure 6.4: Transpiration rates during the day of the different landraces in the different environment of origins. Each panel is an environment and referenced by their state and the native landrace name.

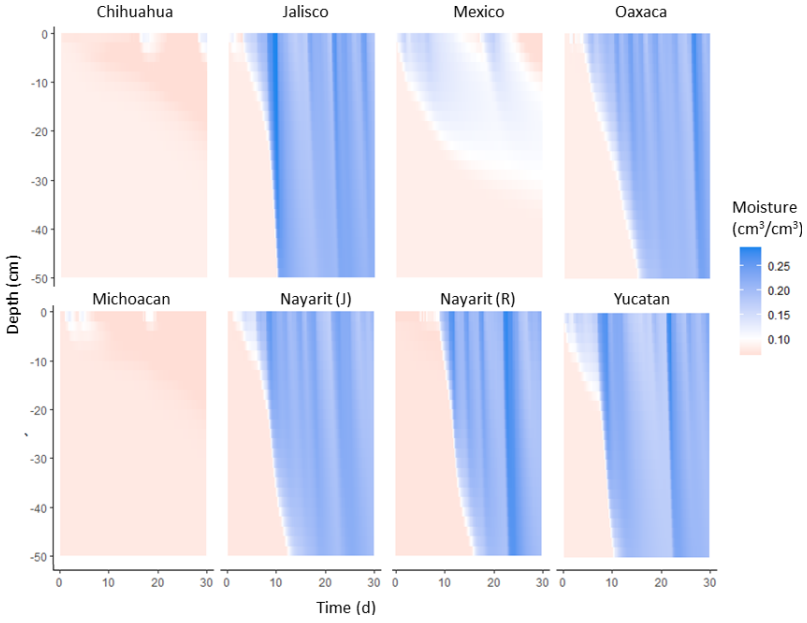


Figure 6.5: Example case of soil water profile records in each one of the eight regions of origins. The soil water profiles are expressed in volumetric moisture content (-).

In Nayarit, where the landrace *Reventador* comes from, the impact index of the hydraulic conductivity of the soil zone within roots influence decreased early on, but not for all landraces. The impact indices for the landraces *Conico*, *Palomero Toloqueno* and *Reventador* seem to be less reduced than the other landraces and also with some delay in comparison to the others. On the contrary, in Mexico, both landraces *Conico* and *Palomero Toloqueno* were the first ones to witness a reduction of their impact index of the hydraulic conductance of the soil zone within roots influence by the end of the growing period.

6.3.2 Root water uptake efficiency

Root water uptake efficiency was defined here as the cumulative uptake per unit of root volume (cm^3/cm^3).

Along the growing period, the root water uptake efficiency was environment and landrace dependent (Figure 6.7). In all virtual envi-

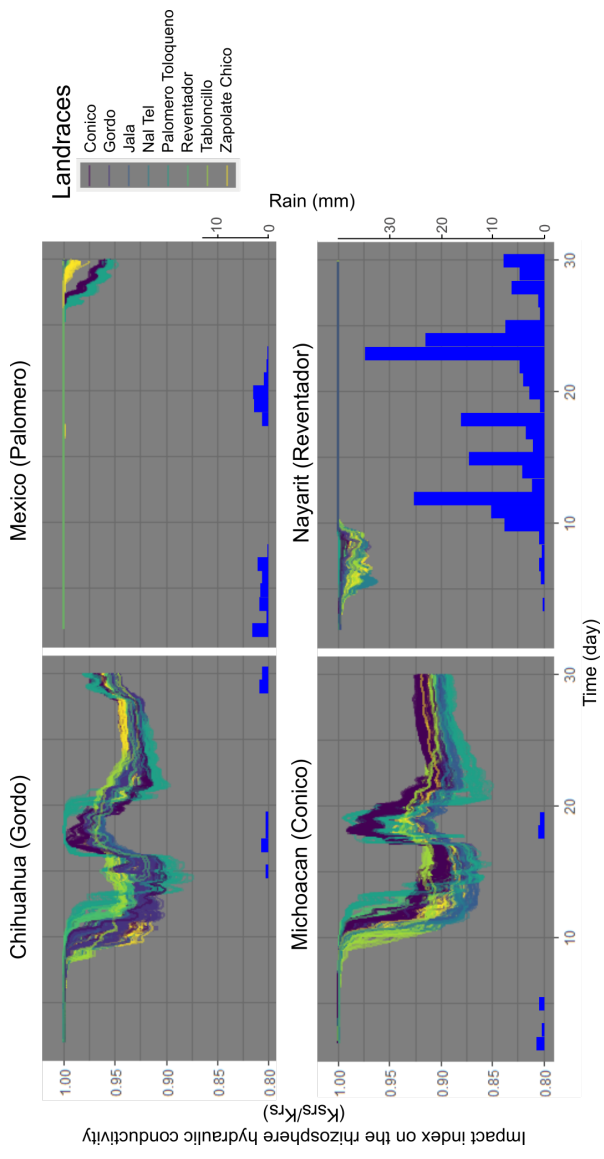


Figure 6.6: Visualization of the dynamic changes of the conductance ratio between the "soil-root system" and the "root system" alone (K_{srs}/K_{rs}) along the 30 days growing period. Each *in silico* plants that grew in one of the four impacted environments is represented by colored lines which depend on the landrace factor. The associated rainfall events (mm) to the environment are presented by their daily mean values.

ronments, linear increases were observed for all landraces during the first 5 days. Yet, the initial slopes were landrace dependent. The oscillations of the root water uptake efficiency have a wavelength of one day, increasing during the day and decreasing during the night, and synchronized with the stepwise function of the potential transpiration rate.

For most of the tested virtual environment, *Conico* and *Palomero Toloqueno* had a stable or even increasing root water uptake efficiency after 10 days, whereas the other had a decreasing trend. In Nayarit, where *Reventador* comes from, almost all *in silico* plants had a better root water uptake efficiency than in other locations. This resulted in non-decreasing trends for all landraces with the exception of the *Jala* landrace which still had a plummeting root water uptake efficiency. There were two environments where the landraces *Conico* and *Palomero Toloqueno* had decreasing efficiency after 10 days. These environments were the two driest environments (in Chihuahua and in Michoacan). Notably, their efficiency regrew for a few days after the rainfall events around the 17^{th} day that occurred in both these environments.

When looking at the end of the 30 days growing period (Figure 6.8), the most efficient root water uptake plants were not the ones that cumulatively took up more water. Root systems that were able to take up large amounts of water in total were not the most efficient either. However, this was mainly true only in the environments that were not the two driest ones. In Michoacan, the landrace *Tabloncillo* was more efficient than *Conico* which was the most efficient in all other tested environments, and was ranked as second in terms of cumulative water uptake. In this environment, the *in silico* landrace that transpired the most water in total was *Jala* (p value < 0.01). In Chihuahua which was also a dry environment, there were no significant differences between the root water uptake efficiency of *Tabloncillo* and the one of *Palomero Toloqueno*. The landrace *Palomero Toloqueno* was the second most efficient root system in the eight environments.

In terms of cumulative root water uptake alone, the landrace *Tabloncillo* was among the best root systems in almost all the tested environments. The only exceptions happened in Michoacan were the landrace *Jala* cumulatively transpired more water than *Tabloncillo* plants (p value < 0.01). In Chihuahua, there was no significant difference between both these landraces. In addition, no significant differences between *Tabloncillo*, *Jala* and *Nal Tel* were observed in the three environments with low elevation, namely: Yucatan (*Nal*

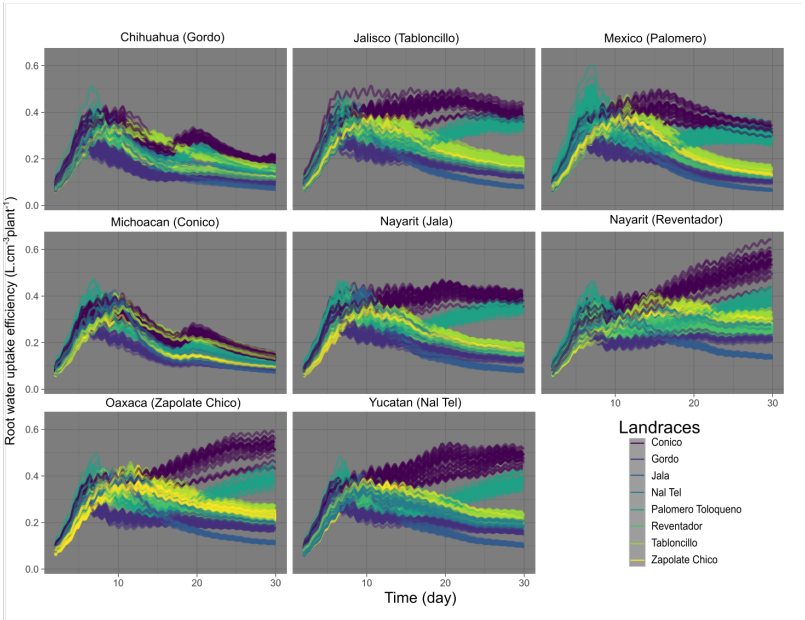


Figure 6.7: Dynamic change of root water uptake efficiency (L.plant^{-1}cm^{-3}) for each landrace and in all eight native locations.

Tel), Nayarit (*Reventador*), and Oaxaca (*Zapolate Chico*).

Among all virtual environments, when comparing the total amount of water taken up (all factors included), the only ones with no significant difference between each other were Nayarit (*Jala*) and Jalisco (*Tabloncillo*) at the end of the 30 days.

6.3.3 Root water uptake efficiency in wet soil

After the analysis of the root water uptake efficiency, one metric that could also potentially be relevant is the root system conductance per unit of Carbon invested in the root system. Here, the proxy of the root volume was used to estimate this Carbon cost. In addition, the equivalent root system hydraulic conductance (K_{rs}) allows the analysis of the root systems independently of their environments.

In Figure 6.9 we divided the conductance of each root system by its root volume at three different stages to evaluate the conductance per unit of Carbon invested in the root system. At first, the landrace

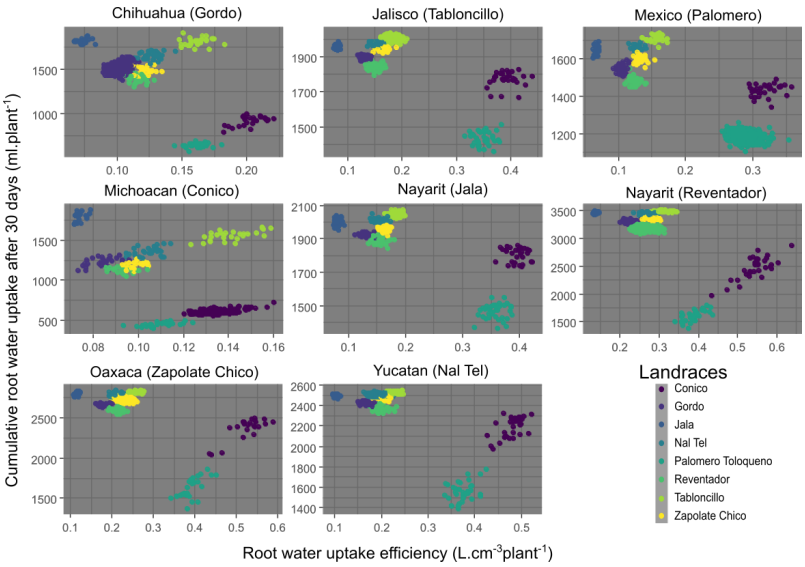


Figure 6.8: Representation of the cumulative root water uptake after 30 days (ml.plant^{-1}) in comparison to the root water uptake efficiency (L.plant^{-1}cm^{-3}) for the eight landraces in the eight regions of origins.

Tabloncillo has the most conductive root system per unit of Carbon invested. During that phase, *Gordo* and *Palomero Toloqueno* were the least conductive per unit of Carbon. Later, after 20 days, the landraces *Tabloncillo*, *Zapolate Chico* and *Conico* were the most conductive per unit of Carbon invested. Whereas, *Gordo* landrace was still the least conductive per unit of Carbon, but after 20 days, the landrace *Reventador* was the second. Along the growing period the *Palomero Toloqueno* landrace decreased less its conductivity per unit of carbon than most of the other landraces, thus it finished at the rank four after 30 days. By the end of the growing period, *Zapolate Chico* took the lead as the most conductive root system per unit of Carbon invested.

6.3.4 Hydraulic properties

The ANOVAs conducted in each virtual environment showed that the subcellular hydraulic properties and the maturation rates influenced the total root water uptake in most environments (Table 6.2). Aside from the landrace factor (root architecture and anatomy) which was the most significant factor to explain the variation of cumulative root

Table 6.2: Mean squares of the landrace factor, subcellular hydraulic properties and maturation rates evaluated after 30 days and their significance. The root traits were: dt_{S-MX} = the duration of the delay between the end of the suberin deposition and the beginning of the maturation of the meta-xylem; dt_{HB} = duration of the deposition of a hydrophobic barrier and the delay between two types of hydrophobic barriers; dt_{MX} = duration of the meta-xylem maturation; k_{AQP} = contribution of aquaporins to the cell membrane permeability ; k_W = cell wall hydraulic conductivity ; K_{PL} = hydraulic conductance of individual plasmodesmata. The abbreviation 'Res.' stands for residuals. The probability levels are: '*' = significant at 95%, '**' = significant at 99%, '***' = significant above 99.9%.

State (founder)	**Landrace**	dt_{S-MX}	dt_{HB}	dt_{MX}	k_{AQP}	k_W	K_{PL}	**Res.**
Chihuahua (Gordo)	5433268 ***	19907 ***	55968 ***	18	129454 ***	12295 **	7269 *	1360
Jalisco (Tabloncillo)	330364 ***	425	23	18	2172 ***	176	39	151
Mexico (Palomero)	518914 ***	14	1583 *	116	10178 ***	328	694	356
Michoacan (Conico)	8315505 ***	30937 ***	36555 ***	439	28504 ***	5320 *	21314 ***	1244
Nayarit (Jala)	240902 ***	616	2426 **	238	6604 ***	45	1	314
Nayarit (Reventador)	1270360 ***	5065	2766	3099	4133	2023	1073	1879
Oaxaca (Zapolate)	782411 ***	9092 *	5218	14	17286 **	16840 **	9745 *	1592
Yucatan (Nal Tel)	560479 ***	11194	1765	2391 *	1772	407	708	593

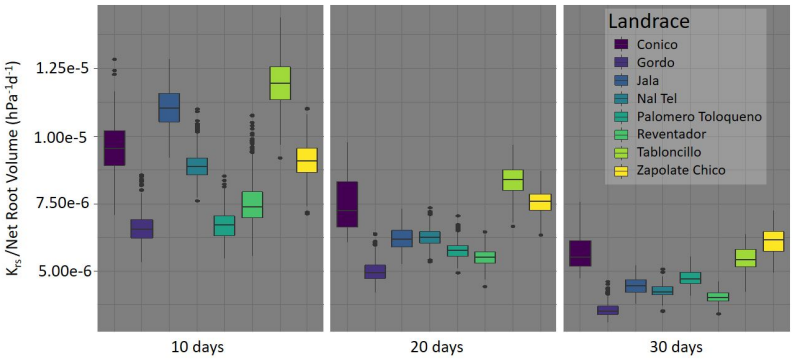


Figure 6.9: The equivalent Root System hydraulic conductance (K_{rs}; $cm^3 hPa^{-1} d^{-1}$) for each landrace per unit of root volume (cm^3) at three different stages of crop development (10, 20, and 30 days).

water uptake after 30 days, it was the contribution of aquaporins to the cell membrane permeability that seemed to explain these variations. However, this was not true in Nayarit (*Reventador*) where the only significant factor was the landrace one. In other locations, such as in Mexico and Nayarit (*Jala*), the duration of the delay between different hydrophobic barriers deposition and the duration of the establishment of these barriers was also significant. Then, in the two driest environments, all subcellular hydraulic properties and maturation rates at the exception of the meta-xylem maturation were significant to explain the variation of total water uptake.

6.4 Discussion

To test the hypothesis that landraces could potentially be hydraulically adapted to their local pedo-climatic environment, we simulated 4127 *in silico* root systems of eight Mexican landraces, in their eight pedo-climatic conditions of origin. The results showed that global root water uptake dynamics were landrace dependent and vary between the virtual locations. Furthermore, the root water uptake efficiency and the cumulative root water uptake of these *in silico* plants were evaluated to see if there were links that could be made between the native landraces with the different environments.

6.4.1 Fast growing roots for early root water uptake ability

Within the framework of this simulation study, the three *in silico* plants that were able to take up the highest amount of water in total in most of the environment were the landrace *Tabloncillo*, *Nal Tel* and *Jala*. One of the differences that could potentially explain why these landraces in comparison to the others had higher cumulative water uptake in most environments was their fast growing basal roots. Indeed, fast growing basal roots in large numbers would establish long absorption sites along the roots from the beginning of the plant development. As in Chapter 5, zero order roots were also contributing to a very large part of the water uptake. In addition, it would allow these *in silico* root systems to reach deeper soil layers more quickly.

Among the three landraces that transpired the most in total, the root systems based on the parameter set of *Tabloncillo* were the best ones in three environments, including their native one. This higher cumulative water uptake seems to be linked to the combination of an average number of basal roots (4) and the fastest growing basal roots ($\pm$ 2.74 cm.d^{-1}). The two others did not display significant differences in terms of total water uptake. The landrace *Jala* was the root system with the second fastest growing basal roots ($\pm$ 2.27 cm.d^{-1}), but had less basal roots (3) than the *Tabloncillo* ones. Whereas, the landrace *Nal Tel* had one more basal root (5) but with slower growth rates ($\pm$ 1.57 cm.d^{-1}). Therefore, a "trade-off" between the growth rate and the number of seminal roots seems to achieve similar results.

6.4.2 Possible trade-off between the transpiration and metabolic cost

In all tested virtual environments, maximizing the cumulative root water uptake was not positively correlated with the overall root water uptake efficiency. The least efficient landrace root systems were often the ones with the highest cumulative root water uptake and inversely. For example, the landrace *Jala* was the least efficient root system of all, in all environments by the end of the growing period. The cause of this phenomenon seems to be linked to fast growing shoot-born roots and their large numbers. Consequently, it increased the root volume and seems to lower the efficiency.

Beside from the landrace *Jala* and *Tabloncillo*, the other landraces seem to rely on the shoot-born roots to reach the deep soil layers and increase their uptake abilities. However, in comparison to the dominant role that the shoot-born roots were supposed to have if we

refer to Chapter 5, it was not as conclusive here. In most of the tested environments, the root systems were not the limiting factor after the first half of the growing period. The shoot water demand clamped the majority of the plant transpiration rates when the shoot-born roots influence should have started. Therefore, in the highly conductive soil with high water availability, the *in silico* plants that took up more during the earliest stage were the ones that took up more water in total.

This constraint played by the shoot water demand hid most of the potential differences between phenotypes in non soil restrictive environments. Adding a module which would account for the landrace differences relative to their shoot part could bring better information about the fitness of these plants in non soil restrictive scenarios. The partitioning of the carbon allocation between the root system and the shoot part is an absent mechanism from this study. Therefore, small root systems like the one of *Conico* and *Palomero Toloqueno* inherited from the same shoot parts as the other root systems which were three to five times bigger at the end of the growing period than them.

Restrictive soil

When analysing the ranking of the landraces in soil restrictive environments, namely: Michoacan where *Conico* comes from, and Chihuahua where *Gordo* comes from, almost all root traits suddenly became significant to explain variation of the total amount of water transpired.

The main factor to explain these differences was the landrace factor. It consisted of the integration of all architectural traits and the root anatomy. In Meunier et al. (2020) study, the root system architecture also counted as the major influential factor when the micro-hydraulic properties have a limited range of variability.

After the landrace factor, the contribution of aquaporins to the cell membrane permeability increased the root water uptake. This is coherent with the findings of Chapter 5. However, within the selected range of variation, the role played by the maturation rates of hydrophobic barriers seems to be more significant than the delay between the end of the suberin deposition and the beginning of the meta-xylem maturation, which was the opposite in Chapter 5. Yet, the influence of the delay between the end of the suberin deposition and the beginning of the meta-xylem maturation was still influential.

6.4.3 Water uptake efficiency with few shoot-born roots

In the two most constraining environments, deeper and bigger root systems seem to increase the total amount of water that the roots were able to take up. However, the landraces with above average root water uptake efficiency were the two smallest root systems, but also the landrace *Tabloncillo*. Surprisingly these *Tabloncillo* root systems with the smallest amount of shoot-born roots managed to still be among the ones that transpired the most and also be among the ones that were very efficient in terms of root water uptake per unit of root volume.

On the one hand, this would suggest that shoot-born roots are not as efficient to take up water in comparison to the other type of roots, but would allow the root system to take up far more water in total and reach the deep soil layers at different times. On the other hand, fast growing seminal roots seem to be simultaneously efficient and able to take up a high amount of water in total. Increasing the analysed growing period could potentially differentiate further the "benefit-risk" approach of such root systems. Potentially, as shoot-born roots revisit the depleted soil layers, they do not participate as much to the water uptake function. Perhaps their values could be noticeable only when they outgrow the seminal roots and their zone of influence.

6.4.4 Possible trade-off between transpiration and soil water depletion risk

Among all the tested environments, four of them were associated with a reduction of the hydraulic conductivity of the soil zone within roots influence. This drop of local soil hydraulic conductivity was the consequence of depleting the soil water.

If the reduction of the conductance ratio between the "soil-root system" and the root system alone (K_{srs}/K_{rs}) occurred early in the growing period, the most impacted phenotypes were the ones that took up the most directly at the beginning. As the water depletion caused the soil conductivity to decrease, the phenotypes that took up large quantities of water faced the consequences of exhausting the soil layer from its water near the absorption sites. However, the depletion of water in the soil layers was balanced by rainfall events.

When the rain replenished the shallow soil layer, the two landraces with the shallowest root systems almost recovered to their maximum potential conductance. Proportionally, for the deep root systems only

a smaller part of their whole soil zone of influence was re-watered. Thus, some deeper soil layers were still drier, and thus less conductive. However, as the shallow root systems were only able to take up water in a narrower region of the soil, even if they took up less water, these shallow layers were depleted again soon after the rain had stopped. This phenomenon seems to have also occurred in the Mexico environment where they both proportionally depleted the most occupied soil layers than the other landraces.

Therefore, to preserve the roots water uptake, it seems that small root systems take advantage of scattered but frequent rainfall at a reduced metabolic cost, whereas, deeper root systems, more carbon costly, are more resilient as the shallow dry soil layers are proportionally in contact with a small surface of the global root system.

6.4.5 Anatomical traits influence

As anatomical traits were merged with the root architectural traits inside the landrace factor, it seems complex to quantify the influence brought by these structural traits at the cross-section level. Although it seems that the influence was rather small, we spotted a feature on the landrace *Reventador* that was most likely linked to its anatomical traits. The strongest and most plausible influence that we could notice was on the equivalent root system conductance per unit of root volume. The *Reventador* landrace had low potential ability to take up water per unit of Carbon invested beside being a landrace with average root architectural traits. The main hypothesis to explain this trend was that the cortex width of this landrace was proportionally larger than for the others, which should have resulted in an increased metabolic cost without any gain in terms of radial hydraulic conductivity nor axial hydraulic conductance. On the contrary to the previous statement, the landrace with the smallest ratio between the cortex width and its root radius was the landrace *Gordo*. Further, *Gordo* was ranked as the least conductive landrace per unit of Carbon. However, this low potential ability to take up water per unit of Carbon was more likely to be due to its low lateral root branching density. The root radial hydraulic conductivity of the lateral roots were 20 to 50 % more conductive than the other root types.

The *in silico* root systems water uptake in the different virtual environments did not seem to be indicative of "local adaptation". However, root anatomical traits were contrasted between landraces. We may have faced a confounding effect due to the intricacy between root

architectural trait and anatomical traits hidden within the landrace factor. Changing one important trait or environmental variable would probably give different results. Further, the weak relation between landrace water uptake and their environment would suggest that we missed somethings. The tested landraces in the virtual phenotyping pipeline were only evaluated based on their root system hydraulic architecture in simplistic scenarios focused on water dynamics.

For example, the proportionally large cortex of the landrace *Reventador* could be an adaptation to a different constraint than water. Recently, Schneider et al. (2021) discussed the utility of a wide root cortex in environments with a strong mechanical impedance. These root traits should potentially improve rooting depth and be an adaptation if the soil of its region of origin are generally compacted.

Other root traits were, perhaps, related to other adaptive functions, such as the adaptation to nutrient deficient soil or to the predation by regional pests. The potential evolutive adaptation behind the shallowest root system of *Palomero Toloqueno* and *Conico* may come from its low phosphorus regional soil (Appendix Figure 6.10), where the highest concentration of phosphorus were in these soil layers (Calderón-Vázquez et al., 2011; Lynch, and Brown, 2008). This particularity of concentrating roots foraging in the top soil reduces spatial competition for phosphorus among roots of the same plant, which is thought to be a positive response to low P availability (Ge et al., 2000). While enhanced top soil foraging is one of the key elements among most P-deficient plants, we would also have expected higher lateral branching density as stated by Lynch, and Brown (2008). Although it was not the case for the known P-deficient landrace *Palomero Toloqueno*, the landraces with increased branching density roots in comparison to the others were *Conico* and *Nal Tel*.

6.5 Conclusion

With the virtual phenotyping pipeline for root hydraulic traits, we tested the hypothesis that there could be non-unique potential sets of root traits for maximizing the total amount of water transpired in specific local hydraulic environments and maximizing the water uptake efficiency.

Among the eight selected maize Mexican landraces from contrasted environments, the *in silico* ones with fast seminal roots were able to take up more water than the others in most of the tested virtual environments. However, the root systems that took up the largest

amount of water were generally the root systems with the minimum efficiency. It was especially true when the *in silico* plants were limited by the above ground conditions. The only major exception was in the most constraining environment. In that environment, the landrace with fastest growing basal roots and the fewest amount of shoot-born roots was the one that transpired the most in total and was also the most efficient one.

Across all environments, we noticed dynamic changes of root water uptake efficiency, which were landrace dependent and varied between locations. The chain of events between the soil water depletion by the roots and drainage, the change of soil hydraulic conductance, and the rainfall precipitations is thought to have a crucial importance over these dynamic changes. Furthermore, the contribution of aquaporins to the cell membrane permeability and maturation rates helped describe the root water uptake of the different landrace as the environments were more and more constraining.

Therefore, we can conclude that when there is a lack of available water, the emergence timing, the numbers, and the growth rate of zero-order roots are "key" candidate traits that allow the root system to explore the soil and absorb water at different depths. A cross-talk between experimentation and the modeling tool would be beneficial to feed the model and check candidate traits. This virtual phenotyping pipeline for root hydraulic traits demonstrated the interest of exploring potential phenotypic adaptation to specific pedo-climatic conditions with dynamic aspects. Further testing and better integration of other root functions are needed to evaluate the fitness of root systems in specific pedo-climatic conditions.

6.6 Appendix

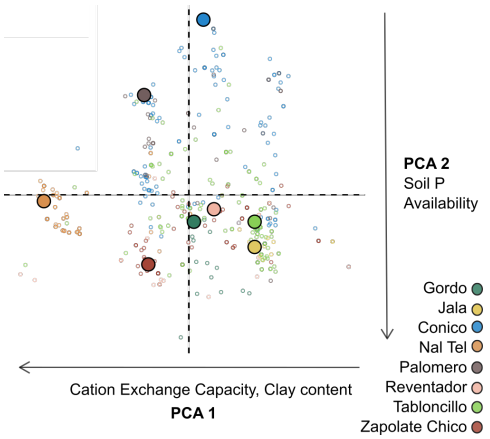


Figure 6.10: Principal Component Analysis (PCA) of the soil factor that could distinguish landraces from each other. The first axis of the PCA was correlated with the cation exchange capacity and the clay content. The second axis of the PCA was correlated with Carbon content, Phosphorus retention which was translated into soil Phosphorus availability. Each dot represents a maize CIMMYT ascension attributed to a race and a location where they were sampled from. The "landrace" are the selected ascensions labeled with a highlighted dot.

Table 6.3: Range for the subcellular hydraulic properties selected as input variables

Abbreviation, Unit	Variable description	Range of variation
k_W $(cm^2 hPa^{-1} d^{-1})$	Cell wall hydraulic conductivity	$[3E^{-4}; 4E^{-4}]$
K_{PL} $(cm^3 hPa^{-1} d^{-1})$	Plasmodesmata hydraulic conductance	$[5E^{-12}; 8E^{-12}]$
k_{AQP} $(cm^2 hPa^{-1} d^{-1})$	Aquaporin contribution to the cell membrane hydraulic conductivity.	$[5E^{-4}; 7E^{-4}]$
dt_{S-MX}, (day)	time delay between the beginning of the endodermis suberization and of the meta-xylem maturation.	[-0.5; 1]
dt_{MX}, (day)	duration of the maturation of the meta-xylem vessels	[1.5; 2.5]
dt_{Hb}, (day)	duration of the deposition of hydrophobic barriers or the delay between two levels of hydrophobic barriers	[1.5; 2.5]

PART IV

DISCUSSION & CONCLUSION

In this last part, outlooks and ideas that emerged from the different studies done in the context of this thesis are presented. They are discussed in the light of the current limitation which are linked to the use of models to describe complex systems. Then, the different elements of answers to the raised scientific questions are summarized in a last chapter.

In some Native languages the term for plants translates to “those who take care of us”.

Robin Wall Kimmerer

DISCUSSION & OUTLOOKS 7

THE GENERAL PURPOSE OF THIS THESIS was to use the root system hydraulic architecture and anatomy of growing plants to estimate possible root water uptake dynamics in specific environments, going from organ scale to plant scale. The integration of the root hydraulic anatomy[1] into the resolution of the water flow in the "soil-root system" brought a large dimension of possible outcomes in terms of root water uptake strategies. This showed how important subcellular hydraulic properties, maturation rates, and root anatomy are in combination with the overall root system architecture to the global root water uptake dynamics.

As the specific objectives of the thesis were divided according to three different scales (the root cross-section, the root system, and the soil-plant system), the discussion will follow the same logic. At the end of the different sections, a few points will merge the discussed topics across the scales.

7.1 The root hydraulic anatomy

The first objective was to better understand the functional importance and diversity of root anatomical traits and subcellular hydraulic properties of maize plants (*Zea mays*).

7.1.1 Biological insights

The first insights brought to functional importance and diversity of root anatomical traits were that (i) the root cortex width played a central role at drawing the baseline of the root radial hydraulic conductivity, (ii) the aerenchyma formation reduces the root radial hydraulic conductivity when it builds up and (iii) the ratio of the stele over the total root cross-section area was proportional to the root radial hydraulic conductivity. However, when analysing the root anatomy in combination with subcellular hydraulic properties, these

[1] **Hydraulic anatomy**: At the root cross-section scale, the hydraulic anatomy corresponds to the combination between the subcellular hydraulic properties and the cells structural network and geometry.

new properties outperformed the influence on the radial hydraulic conductivity by the anatomical traits.

Before suberin deposition, the contribution of aquaporins to the cell membrane permeability was the most influential factor. After that deposition, the conductance of individual plasmodesmata became the most influential factor. The onsets of these hydraulic factors partly hide the variation due to the very structure of the root anatomy. However, the root radius, which allometrically reflects both the influence of the cortex width and the stele size, was still influential over the radial hydraulic conductivity before suberin deposition.

7.1.2 Technological improvements

The creation of the root cross-section computational model, GRANAR, enabled us to rapidly generate anatomies over large ranges or root anatomical traits. These anatomies could then be passed-on to other functional models to estimate functional properties, such as the micro-hydraulic properties that could be acquired with the model MECHA.

One of the key features of GRANAR is that it only requires a simple set of parameters to generate diverse root anatomies, therefore opening the way to the generation of root cross-section avatars from anatomical data sets or from root cross-section images. Unlike other software, such as CellSeT (Pound et al., 2012) or MorphoGraphX (de Reuille et al., 2015) which required either time or heavy microscope equipments to segment organs, GRANAR is user friendly and has low technological requirements.

In addition, once thousands of hydraulic anatomies have been estimated, there was an opportunity to fasten even more these estimations using machine learning algorithms (meta-models). Thus, as long as the range of anatomical traits and subcellular hydraulic properties were within the input range of the trained data, estimation of micro-hydraulic properties can be achieved in a fraction of a second (compared to few minutes with the mechanistic models). These meta-models are powerful tools to perform fast global sensitivity analysis that are very demanding in terms of computational time.

7.1.3 Perspectives

The combined used of GRANAR and MECHA enabled us to gain new knowledge on the determinant of root micro-hydraulic properties. However, there is potentially a lot more to explore with both GRANAR and MECHA (that would, of course, require further validation).

For instance, these tools could be used to explore the influence of other root anatomical traits that were not included in the previous chapters, on the micro-hydraulic properties.

Dicotyledonous roots

In this study, we focused on the root hydraulic anatomies of maize (*Zea mays*), but the model GRANAR is also able to generate basic dicotyledon root cross-section patterns. For example, we tried to simulate vine roots (*Vitis vinifera*), which seem to be visually close to the experimental root cross-section images. (Figure 7.1). In addition, the micro-hydraulic properties of more detailed hydraulic anatomies could be estimated. These added features in the new version of GRANAR are the representation of the intercellular spaces, the septa, and the stellar pith. The MECHA model is still fully compatible with these updates (Figure 7.2).

In the new version of GRANAR, the cortex cells are also rounder than in the previous version, and can be separated into three zones with different cell diameters. This feature can be used to represent multiseriate cortical sclerenchyma, an anatomical trait that seems to matter in terms of foraging ability in soil with high mechanical impedance according to Schneider et al. (2021).

Aerenchyma formation types

The aerenchyma formation process that we implemented in the first GRANAR version was the radial lysogeny (apoptosis). Within the *Poaceae* family, the radial lysogeny process is currently the only known process of aerenchyma formation in the roots (Jung et al., 2008). However, there are other types of aerenchyma formation processes, namely: the tangential lysogeny and the honeycomb schizogeny (cell separation and differentiated cell expansion). As plants develop different types of aerenchyma formations, implementing these other types into GRANAR, and testing whether or not it influences water or solute fluxes, would be of great interest.

In addition, we observed that the aerenchyma formation in grapevine roots was not related to either radial or tangential lysogeny, though it was based on the apoptosis process nonetheless. This new type of aerenchyma formation was implemented in GRANAR and is shown in Figure 7.2. We started to evaluate if this type of cortical lacunae in combination with the intercellular spaces could influence the radial hydraulic conductivity. We reproduce an experimental design similar

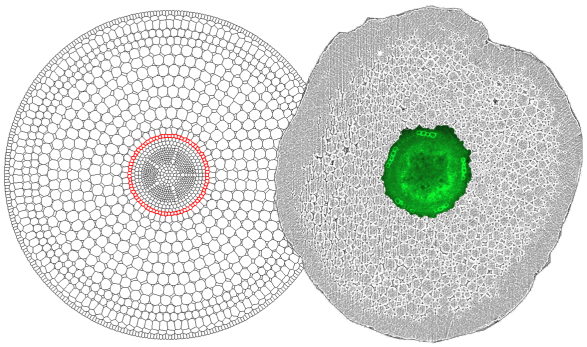


Figure 7.1: Digital avatar of grapevine root cross-section (first order root). The GRANAR root cross-section is on the left and the corresponding experimental image on the right. The anatomical parameters were extracted with ImageJ from two images of the same root performed with two techniques: a micro-CT image of the cortex layers, and an image taken using a fluorescent microscope which replaced the stele. The micro-CT image was obtained by targeting the maturation region of branched clusters of absorptive roots of first order (Cuneo et al., 2021; McCormack et al., 2015). The intercellular spaces which are in darker grey on the micro-CT image are represented on the GRANAR equivalent and the cortex layers were divided in three zones with different cell sizes. The endodermis cell walls are colored in red on the GRANAR root cross-section.

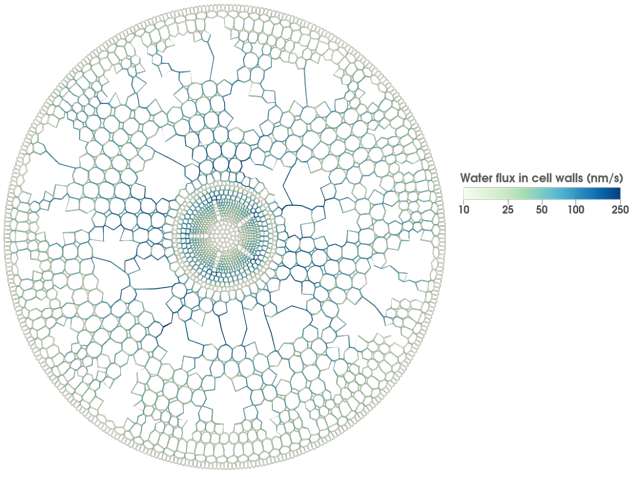


Figure 7.2: Representation of apoplastic fluxes in a grapevine root (*Vitis vinifera*) with cortical lacunae, and septa.

to the one of the Chapter 2 where we could test that. The first glance of answers was that aerenchyma proportion and aerenchyma in combination with intercellular spaces had a significant influence on the radial hydraulic conductivity, but not the intercellular factor alone.

Furthermore, it could be possible to test if the vascular pattern in roots of dicot- or monocotyledonous plants behave differently in function of the type of aerenchyma formation process when everything else is constant.

Secondary growth and cell growth

At the moment, there is no secondary growth nor cell swelling/elongation implemented in the GRANAR model. The addition of a module such as the one existing in OpenAlea (Pradal et al., 2008) or as in CHASTE (Mirams et al., 2013), which account for cell expansion and division could be use to study dicotyledonous roots secondary growth. Those modules could be used to generate age dependent anatomies. Linking these changes in anatomies to the MECHA model would allow us to see how secondary growth influences the root micro-hydraulic properties.

For 3D root representation and growth simulation of *in vivo* plant meristems and local plant organs, the MorphoGraphX software (de Reuille et al., 2015) accounts for mechanical processes and spatial interactions. Although this model is mainly used on *Arabidopsis* which has limited number of cell layers, binding the possible cell network complexity of GRANAR cross-sections with that tool would allow to mimic far more complex organ structures and recreate them *in silico*.

Stem & leaves

To our knowledge, stem and leaf cross-section models which represent the cell network anatomy of these organs are either highly complex (MorphoGraphX) or very schematic (Govaerts et al., 1996). In the future, the versatility of the core algorithm behind the GRANAR model could be modified towards these different plant organs. It would create a new way to evaluate the functional importance of the different anatomical structures inside the plants (this would require an adaptation of the MECHA model as well). At the leaf level, for instance, performing similar sensitivity analysis as the ones done in this study might help us better understand the link between leaf anatomies, transpiration regulation and cavitation prevention.

7.2 Binding root hydraulic anatomies along the root system

The second specific objective of the thesis was to better understand the impact of the root anatomical traits and the development of hydrophobic structure on the overall root system hydraulic architecture.

7.2.1 Biological insights

Experimental root cross-section data along root systems are relatively easy to acquire in comparison to a detailed measurement of the hydraulic conductivity of the different root types. Using the GRANAR-MECHA coupling, we demonstrated how we can translate experimental anatomical traits into hydraulic conductivity estimation and created a high-resolution hydraulic atlas of a maize root system. In the studied case, root anatomical traits changed along the root axis, and this added a significant component of variation in addition to root maturation factor.

7.2.2 Technological improvements

From the root cross-section images of different root systems, we were able to reconstruct possible atlases of the root hydraulic conductivities. This combination of modeling tools with root cross-section images allowed us to estimate potential conductivity function along the roots with very fine resolution and quicker than other available experimental techniques (such as the pressure probe).

7.2.3 Perspective

Root maturation rates influence on the micro-hydraulic traits

One of the missing pieces that we encountered while building the root system hydraulic Atlas was that we did not know how to link unsuberized and suberized root zones hydraulically, nor how to link the un-mature meta-xylem vessels stage to their mature stage. We did a linear regression in between stages but we could actually test different theories with the current tools that we have.

Radially, the suberin deposition in the endodermis cell walls is thought to occupy by batches the cell walls of the endodermis layer (Barberon et al., 2016; Doblas et al., 2017). These depositions by batches are most likely to result in a non-linear decrease of the radial hydraulic conductivity. However, if the suberization occurs one cell at

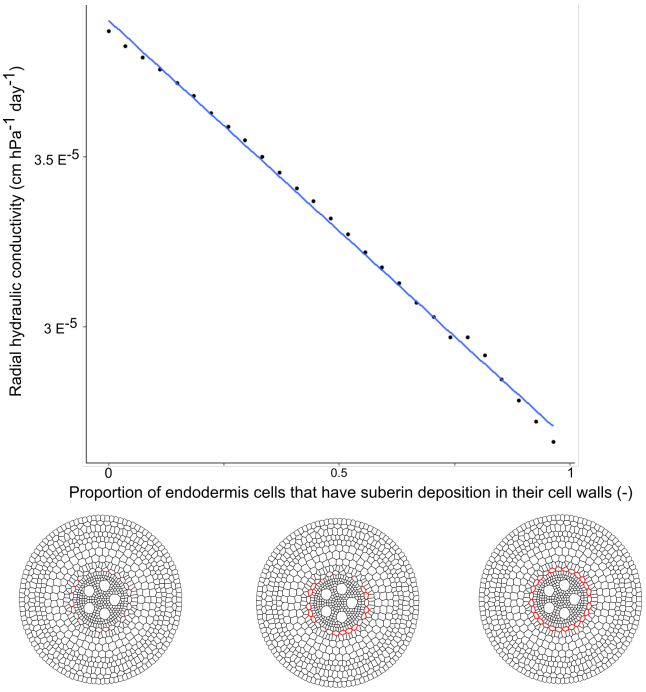


Figure 7.3: Radial hydraulic conductivity decrease for a *in silico* maize as the suberin is deposited in cell walls of endodermis cells, on cell at the time

the time, then, the resulting trend would follow a linear decrease. *In silico* maize root cross-section that we analysed, the decreasing trend of the radial hydraulic conductivity when the cells of the endodermis were suberized one by one randomly was observed to be a monotonic decrease of the radial hydraulic conductivity as the suberization of the endodermis occurred (Figure 7.3).

Axially, meta-xylem maturation was also assumed to be a linear regression between the two stages. However, the way the meta-xylem vessels mature and are progressively integrated into the vascular system of the plant is poorly understood (Sanderson et al., 1988). Cross-walls effect is thought to be strong and reduce the conductance of such conduit. Further, even if meta-xylem vessels are surrounded by lignin, there are slow biological processes to degrade these cross-walls and increase the axial hydraulic conductance. Finally, there is also poor evidence of synchronized meta-xylem maturation or the opposite.

Shoot hydraulic atlases

Once a valid GRANAR-MECHA coupling would be available for the shoot parts, a similar approach to what was done for the root system could be performed on the shoot structure. The creation of hydraulic Atlases for the shoot structures would complete the whole plant model and increase the accuracy of the overall resulting hydraulic architectural model.

The shoot system architecture can be simulated with the model CPlantBox (Zhou et al., 2020) and replace the "big-leaf" approach currently used. Thus, with the shoot hydraulic atlases and the shoot system architecture a modified version of MARSHAL could be used to solve the shoot system hydraulic architecture and provide insight toward preferential flow in homogeneous air conditions. In combination with models such as the one used in Hydraulic Viper, a complete plant hydraulic network could be solved. This would result in plant water dynamics and plant water properties related to complex phene states which would improve our understanding about the plant hydraulic behavior.

7.3 *In silico* maize root water uptake dynamics

The third specific objective of the thesis was to better understand the role of the local hydraulic anatomy on the global root system hydraulic behaviour.

7.3.1 Biological insights

The first insights on how root hydraulic anatomy influence the root water uptake dynamics in different pedo-climatic conditions were that zero-order roots, and their diameters, have a strong influence on both the root water uptake ability and on the uptake efficiency per unit of root volume. Second, the contribution of aquaporins to the cell membrane permeability was the second most influential factor to the cumulative root water uptake and its influence seems to be related to different timing effects dependent on soil water depletion and the root foraging stages. Third, depending on soil hydraulic properties and rainfall pattern, specific sets of local root traits can result in strong water depletion and negative impact on the future transpiration rates of the plants in comparison to other sets of traits for a given root system architecture. Finally, the maturation rates and the length

of the offset period between suberin deposition and the meta-xylem deposition play an important role once the root reaches deep layers.

Among the eight Mexican maize landraces, the *in silico* ones with fast seminal roots were able to take up more water than the others in most of the tested environments. However, the root systems that took up the largest amount of water were generally the root systems with the minimum efficiency. It was especially true when the *in silico* plants were limited by the above ground conditions. The only major exception was in the most constraining environment. In that environment, the landrace with fastest growing basal roots and the fewest amount of shoot-born roots was the one that transpired the most in total and was also the most efficient one.

7.3.2 Technological improvements

By assembling several models into a structured network, we created a virtual phenotyping pipeline for root hydraulic traits (Hydraulic Viper). This computational tool that we developed has a great potential to explore different growing root system hydraulic architectures in various pedo-climatic conditions. Its ability to account for the root anatomical traits, the subcellular hydraulic properties and the maturation rates made it possible to seek potential local root trait adaptation to specific pedo-climatic conditions.

The closest other models that study the root water dynamics and try to account for anatomical differentiation between tested phenotypes is likely the model OpenSimRoot (Postma et al., 2017). OpenSimRoot has the advantages of accounting for carbon partitioning and allocation between root and shoot parts, and of including nutrient uptake and mineralization in the soil. The main advances implemented in Hydraulic Viper come from the analytical resolution of the water flow in the root system (Meunier et al., 2020), the integration of the soil zone within roots influence, the fine tuning of the quantification of root micro-hydraulic properties based on the root age, root cross-section anatomy, and subcellular hydraulic properties.

7.3.3 Perspectives

The future software improvement which would increase the interest of using Hydraulic viper would be to include a carbon partitioning module. Such module could be inspired by the PiafMunch mechanistic approach (Lacointe, and Minchin, 2019) that is currently under development in CPlantBox, or inspired by the functional component of the

model GRAAL-CN (Drouet, and Pagès, 2007). At the moment, the "big-leaf" approach over-simplifies the shoot parts. Thus, increasing the level of complexity of this part would strongly increase the number of biological processes that are included.

In terms of nutrient allocation and organ growth response to available water and nutrients, there is the functional-structural model GRAAL-CN (Drouet, and Pagès, 2007). This model includes many different aspects of growth regulation relatively to the availability of carbon and nitrogen elements. Physiologically, there are many interesting aspects to take from this type of approach. Thus, it would be theoretically possible to move towards a more plastic understanding of the plant phenotypes.

Stomatal regulation

The stomatal regulation is one of the most critical mechanisms which regulate the amount of transpired water. The implemented regulation of the stomatal response was approximate to behave very harshly as a gate. The isohydricity of maize plants is a common feature (Tardieu, and Simonneau, 1998). However, the simplification that plants close their stomata in a way that creates a threshold at -15.000 hPa at the collar is much more debatable and substantially less sharp.

In addition, when the water pressure decreases too much inside the xylem elements, there is a cavitation phenomenon that can occur and dramatically reduce the axial fluxes of water as it opens a discontinuity in the water column (Cochard, 2002). In this study, the consequence is avoided and neglected as the threshold value inside the xylem is capped to -15.000 hPa. Further study could be devoted to understanding the impact of fine stomatal responses and xylem embolism on the root hydraulic architecture and water dynamics of the root system.

Complex 3D soil

The 3D soil representation is far more accurate to simulate root water uptake dynamics than in 1D. One model that accounts for these additional dimensions is the R-SWMS model (Javaux et al., 2008; Koch et al., 2019). The applications of that model are not the same as Hydraulic Viper mainly due to the computational time difference, which is related to the complexity of solving water flow in a 3D mesh across time. However, the way root dries up the soil in its surroundings is more realistic when the horizontal dimension is included, and not

shared in a soil layer reservoir where all roots in the layer have access to.

Plant plasticity

In addition, soil heterogeneity is a key feature which makes the root system very complicated to understand. The root systems are able to develop plastic responses to deal with their changing environment and cause growing patterns and allocation that are still actively investigated. In return, the plants are also able to alter their environment by chemically changing the composition of the soil with mucilage secretion (Kroener et al., 2018).

Benchmarking Hydraulic Viper

At the moment there is not yet a proper validation of our virtual phenotyping pipeline, Hydraulic Viper. However, the transpiration rates were within the same range of value of what is expected for maize plants. During the simulation, the Penman-Monteith equations (Allen, and FAO, 1998) associated with Campos et al. (2017) crop coefficient showed an oscillation between internal and external limiting factors (i.e. the root water uptake ability *vs.* the shoot water demand). This alternation showed that our *in silico* estimations of the root water uptake matched the amount of water transpired by a corresponding plant from a validated crop model.

To benchmark our modeling pipeline, lysimeter experiments could be used to see if, relatively to one another, different plants show similar trend in terms of water uptake dynamics with the models.

In addition, the experimental data that was used to parametrized the models comes from greenhouse experiments in pots and there are a potential differences between the root system of plants in pots and the ones in the field. Shovelomics experiments could increase the transferability of the measure towards the modeling side.

7.4 Structural limitation

7.4.1 On model uncertainties

The main structural limitation that was partially tackled is that complex systems are composed of many interacting parts on many different scales. Reducing the level of complexity by studying each piece individually made us aware of some behavior and mechanisms. Sometimes,

connecting single parts together and expecting the sum of the parts to behave as a whole organism can be misleading. However, this phenomenon is entangled with the way the raised questions were faced in this thesis. Thus, to tackle these issues we gradually increased the interconnections between the lowest scale and the whole soil-plant-atmosphere continuum. That being said, there are still many uncertainties regarding this process and some connections are incomplete or missing.

7.4.2 On computing time

Finally, all the proposed improvement detailed above need to be seen through the lens of computing time and efficiency. The current pipeline is already quite resource intensive and needs to be run on dedicated servers. Adding more modules, or making the existing ones more detailed might increase substantially the computation time, up to a point where the pipeline could not be used as a virtual phenotyping tool. One of the critical loss of efficiency was the continuous change of programming language between model parts. The unification of the different tools under a single languages could increase the global efficiency. Furthermore, the use of artificial intelligence algorithm could always be used to *shortcut* the mechanistic models, as it was done here for the estimation of micro-hydraulic properties.

CONCLUSIONS

8

In crop systems, the phenotypes expressed by plants in their environment are very diverse. Where there is a lack of water availability, the root systems that are sought to improve yield and achieve sustainability are thought to be non-unique, site specific and with a good trade-off between the transpiration potential and the soil water depletion risk. Manipulation of such behavior implies having acute knowledge about the pedo-climatic conditions of the crop site and an ability to choose phenotypes that will express the right state of phenes at the right time.

Along the path of finding such phenotypes, identifying root system hydraulic architecture that expressed the suitable combination of traits for specific pedo-climatic conditions is a complex task. During this thesis, we aimed at providing tools and insights to better understand how the influence of hydraulic anatomy scales up and influences the global root water uptake dynamic.

To do so, we developed GRANAR, a computational model that generates root cross-section anatomies from a simple set of anatomical traits. This model can be coupled with another one (MECHA) which makes possible the estimation of root micro-hydraulic properties. Using this unique combination of computational tools, we were able to pinpoint the crucial role of root anatomy, subcellular hydraulic properties and the maturation stages.

These hydraulic properties were then linked to the root system typology and age. We went along the root axis of different root types and analysed how anatomical trait changes along those axes could add up significant variation to the root hydraulic conductance. Our analysis revealed the importance of maturation rates, such as the timing of the suberin deposition in the endodermis cell walls and the age of maturation for the meta-xylem vessels. These maturation stages change drastically the root hydraulic properties and have the potential to create very different uptake patterns at the root system level.

Finally, we scaled up one step further, and studied the global impact of root hydraulic anatomy on growing plants. To do so we developed a virtual phenotyping pipeline for root hydraulic traits

(Hydraulic Viper) which encompass the previous understanding of the root hydraulic anatomy. This enabled us to understand the pivotal role of the root radii of zero-order roots, the contribution of aquaporins to the cell membrane permeability, and the root maturation rates on the overall root water uptake performance.

The simulations that we performed on the maize variety *B73* showed that the water depletion risk due to high root water uptake can result in a decrease of the potential transpiration rates. This was especially the case in the silty clay soil where the soil retention capacity was low. This trend was also observed when we tested the Mexican maize landraces. However, to recover from over-depleted soil layers, the root systems were either awaiting for the next rainfall events or increasing their reach to deeper soil layers. Therefore, we deduced that when there is a lack of available water, the emergence timing, the numbers, and the growth rate of zero-order roots are key root traits that allow the root system to explore the soil and absorb water at different depths. It was also noticed that some root systems saved up water which was used later without decreasing their potential transpiration rates. These water saving phenotypes had generally small contributions of aquaporins to the cell membrane permeability or small seminal roots, either from small root radius or from small root count and growth rate.

This thesis demonstrated the interest of exploring potential phenotypic adaptation to specific pedo-climatic conditions with dynamic aspects. Further testing and better integration of other root functions are needed to evaluate the fitness of root systems in specific pedo-climatic conditions.

GENERAL BIBLIOGRAPHY

(1) Agee, E., He, L., Bisht, G., Couvreur, V., Shahbaz, P., Meunier, F., Gough, C. M., Matheny, A. M., Bohrer, G., and Ivanov, V. (2021). Root lateral interactions drive water uptake patterns under water limitation. *Advances in Water Resources 151*, 103896 (cit. on p. 86).

(2) Ahmed, M. A., Zarebanadkouki, M., Meunier, F., Javaux, M., Kaestner, A., and Carminati, A. (2018). Root type matters: measurement of water uptake by seminal, crown, and lateral roots in maize. *J. Exp. Bot.* (Cit. on p. 139).

(3) Allen, R. G., and FAO, F., *Crop Evapotranspiration: Guidelines for Computing Crop Water Requirements*; FAO: 1998 (cit. on pp. 31, 127, 145, 156, 191).

(4) Atkinson, J. A., Lobet, G., Noll, M., Meyer, P. E., Griffiths, M., and Wells, D. M. (2017). Combining semi-automated image analysis techniques with machine learning algorithms to accelerate large-scale genetic studies. *Gigascience 6*, 1–7 (cit. on p. 49).

(5) Barberon, M., Vermeer, J. E. M., De Bellis, D., Wang, P., Naseer, S., Andersen, T. G., Humbel, B. M., Nawrath, C., Takano, J., Salt, D. E., et al. (2016). Adaptation of root function by nutrient-induced plasticity of endodermal differentiation. *Cell 164*, 447–459 (cit. on p. 186).

(6) Barczi, J.-F., Rey, H., Griffon, S., and Jourdan, C. (2018). DigR: a generic model and its open source simulation software to mimic three-dimensional root-system architecture diversity. *Annals of botany 121*, 1089–1104 (cit. on p. 63).

(7) Bohm, J. (1893). Capillarität und saftsteigen. *Ber. dtsch. bot. Ges. 11*, 203–212 (cit. on p. 17).

(8) Bolaños, J., Edmeades, G., and Martinez, L. (1993). Eight cycles of selection for drought tolerance in lowland tropical maize. III. Responses in drought-adaptive physiological and morphological traits. *Field Crops Research 31*, 269–286 (cit. on p. 118).

(9) Bomfim, N., Graciano-Ribeiro, D., Nassar, N., et al. (2011). Genetic diversity of root anatomy in wild and cultivated Manihot species. *Genet. Mol. Res 10*, 544–551 (cit. on pp. 25, 40).

(10) Bouda, M., Brodersen, C., and Saiers, J. (2018). Whole root system water conductance responds to both axial and radial traits and network topology over natural range of trait variation. *J. Theor. Biol.* (Cit. on p. 107).

(11) Bouranis, D., Chorianopoulou, S., Siyiannis, V., Protonotarios, V., and Hawkesford, M. (2003). Aerenchyma formation in roots of maize during sulphate starvation. *Planta 217*, 382–391 (cit. on p. 97).

(12) Bret-Harte, M. S., and Silk, W. K. (1994). Nonvascular, Symplasmic Diffusion of Sucrose Cannot Satisfy the Carbon Demands of Growth in the Primary Root Tip of Zea mays L. *Plant Physiol. 105*, 19–33 (cit. on pp. 46, 74, 97).

(13) Brodersen, C. R., Knipfer, T., and McElrone, A. J. (2018). In vivo visualization of the final stages of xylem vessel refilling in grapevine (Vitis vinifera) stems. *New Phytol. 217*, 117–126 (cit. on p. 86).

(14) Brodribb, T. J., and McAdam, S. A. (2017). Evolution of the stomatal regulation of plant water content. *Plant physiology 174*, 639–649 (cit. on p. 21).

(15) Brundrett, M. C., Enstone, D. E., and Peterson, C. A. (1988). A berberine-aniline blue fluorescent staining procedure for suberin, lignin, and callose in plant tissue. *Protoplasma 146*, 133–142 (cit. on pp. 71, 74).

(16) Bruno, G., and Sparapano, L. (2007). Effects of three esca-associated fungi on Vitis vinifera L.: V. Changes in the chemical and biological profile of xylem sap from diseased cv. Sangiovese vines. *Physiol. Mol. Plant Pathol. 71*, 210–229 (cit. on p. 86).

(17) Burton, A. L., Brown, K. M., and Lynch, J. P. (2013). Phenotypic Diversity of Root Anatomical and Architectural Traits in Zea Species. *Crop Sci. 53*, 1042–1055 (cit. on pp. 40, 96, 100).

(18) Burton, A. L., Lynch, J. P., and Brown, K. M. (2013). Spatial distribution and phenotypic variation in root cortical aerenchyma of maize (Zea mays L.) *Plant Soil 367*, 263–274 (cit. on pp. 25, 40, 44, 46, 50, 62).

(19) Burton, A. L., Williams, M., Lynch, J. P., and Brown, K. M. (2012). RootScan: Software for high-throughput analysis of root anatomical traits. *Plant Soil 357*, 189–203 (cit. on pp. 48, 60, 63).

(20) Cai, G., Vanderborght, J., Couvreur, V., Mboh, C. M., and Vereecken, H. (2018). Parameterization of Root Water Uptake Models Considering Dynamic Root Distributions and Water Uptake Compensation. *Vadose Zone J. 17* (cit. on p. 86).

(21) Calderón-Vázquez, C., Sawers, R. J., and Herrera-Estrella, L. (2011). Phosphate deprivation in maize: genetics and genomics. *Plant physiology 156*, 1067–1077 (cit. on p. 173).

(22) Campos, H., Cooper, M., Habben, J., Edmeades, G., and Schussler, J. (2004). Improving drought tolerance in maize: a view from industry. *Field Crops Research 90*, 19–34 (cit. on p. 118).

(23) Campos, I., Neale, C. M. U., Suyker, A. E., Arkebauer, T. J., and Gonçalves, I. Z. (2017). Reflectance-based crop coefficients REDUX: For operational evapotranspiration estimates in the age of high producing hybrid varieties. *Agric. Water Manage. 187*, 140–153 (cit. on pp. 127, 146, 156, 191).

(24) Carminati, A., and Javaux, M. (2020). Soil Rather Than Xylem Vulnerability Controls Stomatal Response to Drought. *Trends Plant Sci.* (Cit. on pp. 6, 18, 21, 119).

(25) Chapman, S. C. (2008). Use of crop models to understand genotype by environment interactions for drought in real-world and simulated plant breeding trials. *Euphytica 161*, 195–208 (cit. on pp. 22, 93).

(26) Chimungu, J. G., Brown, K. M., and Lynch, J. P. (2014). Large root cortical cell size improves drought tolerance in maize. *Plant Physiol. 166*, 2166–2178 (cit. on pp. 61, 69, 94, 96, 100, 141).

(27) Chimungu, J. G., Brown, K. M., and Lynch, J. P. (2014). Reduced root cortical cell file number improves drought tolerance in maize. *Plant Physiol. 166*, 1943–1955 (cit. on pp. 6, 25, 40, 44, 46, 50, 52, 61, 69, 94).

(28) Chopard, J., Godin, C., and Traas, J. In *Proceedings of the 7th International Workshop on Information Processing in Cells and Tissues*, 2007, pp 387–399 (cit. on p. 61).

(29) Chopin, J., Laga, H., Huang, C. Y., Heuer, S., and Miklavcic, S. J. (2015). RootAnalyzer: A Cross-Section Image Analysis Tool for Automated Characterization of Root Cells and Tissues. *PLoS One 10*, e0137655 (cit. on pp. 48, 60).

(30) Cochard, H. (2002). Xylem embolism and drought-induced stomatal closure in maize. *Planta 215*, 466–471 (cit. on pp. 17, 21, 190).

(31) Comas, L. H., Becker, S. R., Cruz, V. M. V., Byrne, P. F., and Dierig, D. A. (2013). Root traits contributing to plant productivity under drought. *Front. Plant Sci. 4*, 442 (cit. on p. 30).

(32) Cornelis, S., and Hazak, O. (2021). Understanding the root xylem plasticity for designing resilient crops. *Plant, Cell & Environment* (cit. on p. 28).

(33) Cosenza, A., Mannina, G., Vanrolleghem, P. A., and Neumann, M. B. (2013). Global sensitivity analysis in wastewater applications: A comprehensive comparison of different methods. *Environmental modelling & software 49*, 40–52 (cit. on p. 108).

(34) Couvreur, V., Faget, M., Lobet, G., Javaux, M., Chaumont, F., and Draye, X. (2018). Going with the Flow: Multiscale Insights into the Composite Nature of Water Transport in Roots. *Plant Physiol. 178*, 1689–1703 (cit. on pp. 6, 11, 15, 20, 22, 25, 40, 41, 45–47, 51, 61, 69, 74, 93, 94, 97, 98, 106, 119).

(35) Couvreur, V., Vanderborght, J., and Javaux, M. (2012). A simple three-dimensional macroscopic root water uptake model based on the hydraulic architecture approach. *Hydrol. Earth Syst. Sci. 16*, 2957–2971 (cit. on pp. 20, 22, 24, 120, 125, 153).

(36) Couvreur, V., Faget, M., Lobet, G., Javaux, M., and Chaumont, F. (2017). Novel multiscale insights into the composite nature of water 2 transport in roots. *BioRxiv* (cit. on p. 25).

(37) Cukier, R., Levine, H., and Shuler, K. (1978). Nonlinear sensitivity analysis of multiparameter model systems. *Journal of computational physics 26*, 1–42 (cit. on p. 100).

(38) Cuneo, I. F., Barrios-Masias, F., Knipfer, T., Uretsky, J., Reyes, C., Lenain, P., Brodersen, C. R., Walker, M. A., and McElrone, A. J. (2021). Differences in grapevine rootstock sensitivity and recovery from drought are linked to fine root cortical lacunae and root tip function. *New Phytologist 229*, 272–283 (cit. on p. 184).

(39) Cuneo, I. F., Knipfer, T., Brodersen, C. R., and McElrone, A. J. (2016). Mechanical failure of fine root cortical cells initiates plant hydraulic decline during drought. *Plant Physiology 172*, 1669–1678 (cit. on p. 25).

(40) Daryanto, S., Wang, L., and Jacinthe, P.-A. (2016). Global synthesis of drought effects on maize and wheat production. *PloS one 11*, e0156362 (cit. on p. 32).

(41) de Dorlodot, S., Forster, B., Pagès, L., Price, A., Tuberosa, R., and Draye, X. (2007). Root system architecture: opportunities and constraints for genetic improvement of crops. *Trends Plant Sci. 12*, 474–481 (cit. on pp. 6, 18).

(42) de Reuille, P. B., Routier-Kierzkowska, A.-L., Kierzkowski, D., Bassel, G. W., Schüpbach, T., Tauriello, G., Bajpai, N., Strauss, S., Weber, A., Kiss, A., et al. (2015). MorphoGraphX: A platform for quantifying morphogenesis in 4D. *Elife 4*, e05864 (cit. on pp. 182, 185).

(43) de Souza, T. C., de Castro, E. M., César Magalhães, P., De Oliveira Lino, L., Trindade Alves, E., and de Albuquerque, P. E. P. (2013). Morphophysiology, morphoanatomy, and grain yield under field conditions for two maize hybrids with contrasting response to drought stress. *Acta Physiol. Plant 35*, 3201–3211 (cit. on p. 62).

(44) Dietterich, T. G. In *International workshop on multiple classifier systems*, 2000, pp 1–15 (cit. on p. 105).

(45) Ding, L., Milhiet, T., Couvreur, V., Nelissen, H., Meziane, A., Parent, B., Aesaert, S., Van Lijsebettens, M., Inzé, D., and Tardieu, F. (2020). Modification of the expression of the aquaporin ZmPIP2; 5 affects water relations and plant growth. *Plant physiology 182*, 2154–2165 (cit. on pp. 27, 86, 106).

(46) Doblas, V. G., Geldner, N., and Barberon, M. (2017). The endodermis, a tightly controlled barrier for nutrients. *Current Opinion in Plant Biology 39*, 136–143 (cit. on p. 186).

(47) Donald, C. M. (1968). The breeding of crop ideotypes. *Euphytica 17*, 385–403 (cit. on p. 30).

(48) Doussan, C., Page, L. C., and Vercambre, G. (1998). Modelling of the Hydraulic Architecture of Root Systems: An Integrated Approach to Water Absorption–Model Description. *Ann. Bot. 81*, 213–223 (cit. on pp. 47, 56, 69).

(49) Doussan, C., Vercambre, G., and Pagè, L. C. (1998). Modelling of the Hydraulic Architecture of Root Systems: An Integrated Approach to Water Absorption–Distribution of Axial and Radial Conductances in Maize. *Ann. Bot. 81*, 225–232 (cit. on pp. 20, 69, 75, 84, 85).

(50) Draye, X., Kim, Y., Lobet, G., and Javaux, M. (2010). Model-assisted integration of physiological and environmental constraints affecting the dynamic and spatial patterns of root water uptake from soils. *J. Exp. Bot. 61*, 2145–2155 (cit. on pp. 17, 20).

(51) Drouet, J.-L., and Pagès, L. (2007). GRAAL-CN: A model of GRowth, Architecture and ALlocation for Carbon and Nitrogen dynamics within whole plants formalised at the organ level. *Ecol. Modell. 206*, 231–249 (cit. on p. 190).

(52) Dunbabin, V. M., Postma, J. A., Schnepf, A., Pagès, L., Javaux, M., Wu, L., Leitner, D., Chen, Y. L., Rengel, Z., and Diggle, A. J. (2013). Modelling root–soil interactions using three–dimensional models of root growth, architecture and function. *Plant Soil 372*, 93–124 (cit. on p. 21).

(53) Dyson, R. J., Vizcay-Barrena, G., Band, L. R., Fernandes, A. N., French, A. P., Fozard, J. A., Hodgman, T. C., Kenobi, K., Pridmore, T. P., Stout, M., Wells, D. M., Wilson, M. H., Bennett, M. J., and Jensen, O. E. (2014). Mechanical modelling quantifies the functional importance of outer tissue layers during root elongation and bending. *New Phytol. 202*, 1212–1222 (cit. on p. 61).

(54) Ehlert, C., Maurel, C., Tardieu, F., and Simonneau, T. (2009). Aquaporin-mediated reduction in maize root hydraulic conductivity impacts cell turgor and leaf elongation even without changing transpiration. *Plant Physiol. 150*, 1093–1104 (cit. on pp. 46, 74, 97).

(55) Emerson, J. W., Green, W. A., Schloerke, B., Crowley, J., Cook, D., Hofmann, H., and Wickham, H. (2013). The Generalized Pairs Plot. *J. Comput. Graph. Stat. 22*, 79–91 (cit. on p. 76).

(56) Enstone, D. E., and Peterson, C. A. Suberin lamella development in maize seedling roots grown in aerated and stagnant conditions., 2005 (cit. on pp. 47, 56).

(57) Enstone, D. E., Peterson, C. A., and Ma, F. (2002). Root Endodermis and Exodermis: Structure, Function, and Responses to the Environment. *J. Plant Growth Regul. 21*, 335–351 (cit. on pp. 25, 40, 69).

(58) Fan, M., Bai, R., Zhao, X., and Zhang, J. (2007). Aerenchyma Formed Under Phosphorus Deficiency Contributes to the Reduced Root Hydraulic Conductivity in Maize Roots. *J. Integr. Plant Biol. 49*, 598–604 (cit. on pp. 40, 62, 69, 94).

(59) Feldman, L. In *The maize handbook*; Springer: 1994, pp 29–37 (cit. on p. 33).

(60) Fradgley, N., Evans, G., Biernaskie, J. M., Cockram, J., Marr, E. C., Oliver, A. G., Ober, E., and Jones, H. (2020). Effects of breeding history and crop management on the root architecture of wheat. *Plant and soil 452*, 587–600 (cit. on p. 118).

(61) Frensch, J., and Steudle, E. (1989). Axial and Radial Hydraulic Resistance to Roots of Maize (Zea mays L.) *Plant Physiol. 91*, 719–726 (cit. on pp. 68, 69, 85).

(62) Fuad-Hassan, A., Tardieu, F., and Turc, O. (2008). Drought-induced changes in anthesis-silking interval are related to silk expansion: A spatio-temporal growth analysis in maize plants subjected to soil water deficit. *Plant, Cell & Environment 31*, 1349–1360 (cit. on pp. 5, 7, 32).

(63) Gaastra, P. Photosynthesis of crop plants as influenced by light, carbon dioxide, temperature, and stomatal diffusion resistance., Ph.D. Thesis, Veenman, 1959 (cit. on p. 17).

(64) Gao, K., Chen, F., Yuan, L., Zhang, F., and Mi, G. (2015). A comprehensive analysis of root morphological changes and nitrogen allocation in maize in response to low nitrogen stress. *Plant Cell Environ. 38*, 740–750 (cit. on pp. 45, 46, 50, 96, 100).

(65) Ge, Z., Rubio, G., and Lynch, J. P. (2000). The importance of root gravitropism for inter-root competition and phosphorus acquisition efficiency: results from a geometric simulation model. *Plant and soil 218*, 159–171 (cit. on p. 173).

(66) Govaerts, Y. M., Jacquemoud, S., Verstraete, M. M., and Ustin, S. L. (1996). Three-dimensional radiation transfer modeling in a dicotyledon leaf. *Applied optics 35*, 6585–6598 (cit. on p. 185).

(67) Hachez, C., Moshelion, M., Zelazny, E., Cavez, D., and Chaumont, F. Localization and Quantification of Plasma Membrane Aquaporin Expression in Maize Primary Root: A Clue to Understanding their Role as Cellular Plumbers., 2006 (cit. on pp. 25, 40, 49, 106).

(68) Hachez, C., Veselov, D., Ye, Q., Reinhardt, H., Knipfer, T., Fricke, W., and Chaumont, F. (2012). Short-term control of maize cell and root water permeability through plasma membrane aquaporin isoforms. *Plant Cell Environ. 35*, 185–198 (cit. on pp. 40, 93).

(69) Harrison, M. T., Tardieu, F., Dong, Z., Messina, C. D., and Hammer, G. L. (2014). Characterizing drought stress and trait influence on maize yield under current and future conditions. *Glob. Chang. Biol. 20*, 867–878 (cit. on p. 5).

(70) Hernández-Hernández, V., Benıtez, M., and Boudaoud, A. (2020). Interplay between turgor pressure and plasmodesmata during plant development. *Journal of experimental botany 71*, 768–777 (cit. on p. 27).

(71) Herrero, M. P., and Johnson, R. (1981). Drought stress and its effects on maize reproductive systems 1. *Crop science 21*, 105–110 (cit. on pp. 7, 32).

(72) Heymans, A., Couvreur, V., LaRue, T., Paez-Garcia, A., and Lobet, G. (2020). GRANAR, a Computational Tool to Better Understand the Functional Importance of Monocotyledon Root Anatomy. *Plant Physiol. 182*, 707–720 (cit. on pp. 69, 85, 94, 107, 108, 119).

(73) Heymans, A., Couvreur, V., and Lobet, G. (2021). Combining cross-section images and modeling tools to create high-resolution root system hydraulic atlases in Zea mays. *Plant direct 5*, e00290 (cit. on pp. 96, 100).

(74) Hose, E., Steudle, E., and Hartung, W. (2000). Abscisic acid and hydraulic conductivity of maize roots: a study using cell- and root-pressure probes. *Planta 211*, 874–882 (cit. on pp. 27, 31, 40).

(75) Huang, B., and Nobel, P. S. (1993). Hydraulic conductivity and anatomy along lateral roots of cacti: changes with soil water status. *New Phytol. 123*, 499–507 (cit. on p. 62).

(76) Iooss, B., Da Veiga, S., Janon, A., Pujol, G., Iooss, M. B., Rcpp, L., Suggests condMVNorm, R., and DiceDesign, D. (2021). Package 'sensitivity'. (cit. on pp. 127, 158).

(77) Jägermeyr, J., Müller, C., Ruane, A. C., Elliott, J., Balkovic, J., Castillo, O., Faye, B., Foster, I., Folberth, C., Franke, J. A., et al. (2021). Climate impacts on global agriculture emerge earlier in new generation of climate and crop models. *Nature Food*, 1–13 (cit. on p. 32).

(78) Javaux, M., Schröder, T., Vanderborght, J., and Vereecken, H. (2008). Use of a Three-Dimensional Detailed Modeling Approach for Predicting Root Water Uptake. *Vadose Zone J. 7*, 1079 (cit. on pp. 21, 69, 190).

(79) Javot, H., and Maurel, C. (2002). The role of aquaporins in root water uptake. *Annals of Botany 90*, 301–313 (cit. on pp. 6, 25, 27, 69, 94, 119).

(80) Johnson, K. D., Herman, E. M., and Chrispeels, M. J. (1989). An abundant, highly conserved tonoplast protein in seeds. *Plant Physiology 91*, 1006–1013 (cit. on p. 27).

(81) Jung, J., Lee, S. C., and Choi, H.-K. (2008). Anatomical patterns of aerenchyma in aquatic and wetland plants. *Journal of Plant Biology 51*, 428–439 (cit. on p. 183).

(82) Kitin, P., Nakaba, S., Hunt, C. G., Lim, S., and Funada, R. (2020). Direct fluorescence imaging of lignocellulosic and suberized cell walls in roots and stems. *AoB Plants 12*, plaa032 (cit. on p. 86).

(83) Koch, A., Meunier, F., Vanderborght, J., Garré, S., Pohlmeier, A., and Javaux, M. (2019). Functional-structural root-system model validation using a soil MRI experiment. *J. Exp. Bot. 70*, 2797–2809 (cit. on p. 190).

(84) Koch, T., Wu, H., and Schneider, M. (2021). Nonlinear mixed-dimension model for embedded tubular networks with application to root water uptake. *Journal of Computational Physics*, 110823 (cit. on p. 21).

(85) Kong, D., Wang, J., Valverde-Barrantes, O. J., and Kardol, P. (2021). A framework to assess the carbon supply–consumption balance in plant roots. *New Phytologist 229*, 659–664 (cit. on p. 30).

(86) Kramer, P. J. (1938). Root resistance as a cause of the absorption lag. *Am. J. Bot. 25*, 110–113 (cit. on p. 6).

(87) Kroener, E., Holz, M., Zarebanadkouki, M., Ahmed, M., and Carminati, A. (2018). Effects of mucilage on rhizosphere hydraulic functions depend on soil particle size. *Vadose Zone Journal 17*, 1–11 (cit. on pp. 16, 191).

(88) Lacointe, A., and Minchin, P. E. In *Phloem*; Springer: 2019, pp 371–386 (cit. on p. 189).

(89) Lambers, H., Atkin, O., Millenaar, F., Waisel, Y., Eshel, A., and Kafkaki, U. (2002). Plant roots: the hidden half. (cit. on p. 30).

(90) Landsberg, J. J., and Fowkes, N. D. (1978). Water Movement Through Plant Roots. *Ann. Bot. 42*, 493–508 (cit. on p. 20).

(91) Lartaud, M., Perin, C., Courtois, B., Thomas, E., Henry, S., Bettembourg, M., Divol, F., Lanau, N., Artus, F., Bureau, C., Verdeil, J.-L., Sarah, G., Guiderdoni, E., and Dievart, A. (2014). PHIV-RootCell: a supervised image analysis tool for rice root anatomical parameter quantification. *Front. Plant Sci. 5*, 790 (cit. on pp. 48, 60, 63).

(92) Lawlor, D., and Cornic, G. (2002). Photosynthetic Carbon Assimilation and Associated Metabolism in Relation to Water Deficits in Higher Plants. *Plant, cell & environment 25*, 275–294 (cit. on p. 17).

(93) Leitner, D., Meunier, F., Bodner, G., Javaux, M., and Schnepf, A. (2014). Impact of contrasted maize root traits at flowering on water stress tolerance – A simulation study. *Field Crops Res. 165*, 125–137 (cit. on pp. 30, 68).

(94) Lenth, R., Singmann, H., Love, J., Buerkner, P., and Herve, M. (2018). Emmeans: Estimated marginal means, aka least-squares means. *R package version 1*, 3 (cit. on p. 76).

(95) Lewis, A. M., and Boose, E. R. (1995). Estimating volume flow rates through xylem conduits. *Am. J. Bot. 82*, 1112–1116 (cit. on p. 62).

(96) Li, Y., Sperry, J. S., and Shao, M. (2009). Hydraulic conductance and vulnerability to cavitation in corn (Zea mays L.) hybrids of differing drought resistance. *Environ. Exp. Bot. 66*, 341–346 (cit. on pp. 62, 84).

(97) Lobet, G., Koevoets, I. T., Noll, M., Meyer, P. E., Tocquin, P., Pagès, L., and Périlleux, C. (2017). Using a Structural Root System Model to Evaluate and Improve the Accuracy of Root Image Analysis Pipelines. *Front. Plant Sci. 8*, 447 (cit. on pp. 11, 95).

(98) Lobet, G., Pagès, L., and Draye, X. (2014). A modeling approach to determine the importance of dynamic regulation of plant hydraulic conductivities on the water uptake dynamics in the soil-plant-atmosphere system. *Ecol. Modell. 290*, 65–75 (cit. on p. 40).

(99) Lobet, G., Pagès, L., and Draye, X. (2011). A novel image-analysis toolbox enabling quantitative analysis of root system architecture. *Plant physiology 157*, 29–39 (cit. on p. 122).

(100) Lynch, J. P. (2015). Root phenes that reduce the metabolic costs of soil exploration: opportunities for 21st century agriculture. *Plant Cell Environ. 38*, 1775–1784 (cit. on p. 61).

(101) Lynch, J. P. (2013). Steep, cheap and deep: an ideotype to optimize water and N acquisition by maize root systems. *Ann. Bot. 112*, 347–357 (cit. on pp. 30, 152).

(102) Lynch, J. P., and Brown, K. M. In *The Ecophysiology of Plant-Phosphorus Interactions*, White, P. J., and Hammond, J. P., Eds.; Springer Netherlands: Dordrecht, 2008, pp 83–116 (cit. on pp. 62, 173).

(103) Lynch, J. P., Chimungu, J. G., and Brown, K. M. (2014). Root anatomical phenes associated with water acquisition from drying soil: targets for crop improvement. *J. Exp. Bot. 65*, 6155–6166 (cit. on pp. 25, 40, 61, 62, 69).

(104) Ma, F., and Peterson, C. A. (2001). Frequencies of plasmodesmata in Allium cepa L. roots: implications for solute transport pathways. *J. Exp. Bot. 52*, 1051–1061 (cit. on pp. 46, 74, 97).

(105) Ma, Z., Guo, D., Xu, X., Lu, M., Bardgett, R. D., Eissenstat, D. M., McCormack, M. L., and Hedin, L. O. (2018). Evolutionary history resolves global organization of root functional traits. *Nature 555*, 94–97 (cit. on pp. 25, 40).

(106) Manschadi, A. M., Christopher, J., deVoil, P., and Hammer, G. L. (2006). The role of root architectural traits in adaptation of wheat to water-limited environments. *Funct. Plant Biol. 33*, 823–837 (cit. on pp. 6, 18).

(107) Martre, P., North, G. B., and Nobel, P. S. (2001). Hydraulic conductance and mercury-sensitive water transport for roots of Opuntia acanthocarpa in relation to soil drying and rewetting. *Plant Physiol. 126*, 352–362 (cit. on pp. 18, 68).

(108) Maurel, C., and Nacry, P. (2020). Root architecture and hydraulics converge for acclimation to changing water availability. *Nat Plants* (cit. on pp. 68, 119).

(109) Maurel, C., Verdoucq, L., Luu, D.-T., and Santoni, V. (2008). Plant aquaporins: membrane channels with multiple integrated functions. *Annu. Rev. Plant Biol. 59*, 595–624 (cit. on p. 27).

(110) McAinsh, M. R., Brownlee, C., and Hetherington, A. M. (1990). Abscisic acid-induced elevation of guard cell cytosolic Ca 2+ precedes stomatal closure. *Nature 343*, 186–188 (cit. on p. 19).

(111) McCormack, M. L., Dickie, I. A., Eissenstat, D. M., Fahey, T. J., Fernandez, C. W., Guo, D., Helmisaari, H.-S., Hobbie, E. A., Iversen, C. M., Jackson, R. B., et al. (2015). Redefining fine roots improves understanding of below-ground contributions to terrestrial biosphere processes. *New Phytologist 207*, 505–518 (cit. on p. 184).

(112) McDonald, M., Galwey, N., and Colmer, T. (2002). Similarity and diversity in adventitious root anatomy as related to root aeration among a range of wetland and dryland grass species. *Plant, Cell & Environment 25*, 441–451 (cit. on pp. 25, 40).

(113) Meunier, F., Couvreur, V., Draye, X., Vanderborght, J., and Javaux, M. (2017). Towards quantitative root hydraulic phenotyping: novel mathematical functions to calculate plant-scale hydraulic parameters from root system functional and structural traits. *J. Math. Biol. 75*, 1133–1170 (cit. on p. 20).

(114) Meunier, F., Draye, X., Vanderborght, J., Javaux, M., and Couvreur, V. (2017). A hybrid analytical-numerical method for solving water flow equations in root hydraulic architectures. *Appl. Math. Model. 52*, 648–663 (cit. on pp. 40, 147).

(115) Meunier, F., Heymans, A., Draye, X., Couvreur, V., Javaux, M., and Lobet, G. (2019). MARSHAL, a novel tool for virtual phenotyping of maize root system hydraulic architectures. *in silico Plants* (cit. on p. 31).

(116) Meunier, F., Heymans, A., Draye, X., Couvreur, V., Javaux, M., and Lobet, G. (2020). MARSHAL, a novel tool for virtual phenotyping of maize root system hydraulic architectures. *in silico Plants 2* (cit. on pp. 22, 68, 69, 85, 86, 108, 119, 126, 153, 170, 189).

(117) Meunier, F., Rothfuss, Y., Bariac, T., Biron, P., Richard, P., Durand, J.-L., Couvreur, V., Vanderborght, J., and Javaux, M. (2018). Measuring and Modeling Hydraulic Lift of Lolium multiflorum Using Stable Water Isotopes. *Vadose Zone J. 17*, 160134 (cit. on pp. 20, 126, 147).

(118) Meunier, F., Zarebanadkouki, M., Ahmed, M. A., Carminati, A., Couvreur, V., and Javaux, M. (2018). Hydraulic conductivity of soil-grown lupine and maize unbranched roots and maize root-shoot junctions. *J. Plant Physiol.* (Cit. on pp. 68, 85).

(119) Mirams, G. R., Arthurs, C. J., Bernabeu, M. O., Bordas, R., Cooper, J., Corrias, A., Davit, Y., Dunn, S.-J., Fletcher, A. G., Harvey, D. G., et al. (2013). Chaste: an open source C++ library for computational physiology and biology. *PLoS computational biology 9*, e1002970 (cit. on p. 185).

(120) Moreno-Ortega, B. Developmental instability in lateral roots of maize: a multi-scale analysis., Ph.D. Thesis, Montpellier SupAgro, 2016 (cit. on pp. 45, 62).

(121) Morris, M. D. (1991). Factorial sampling plans for preliminary computational experiments. *Technometrics 33*, 161–174 (cit. on p. 109).

(122) Newton, A., Akar, T., Baresel, J., Bebeli, P., Bettencourt, E., Bladenopoulos, K., Czembor, J., Fasoula, D., Katsiotis, A., Koutis, K., et al. (2011). Cereal landraces for sustainable agriculture. *Sustainable Agriculture Volume 2*, 147–186 (cit. on p. 153).

(123) OECD-FAO Agricultural Outlook., Type: dataset, OECD Publishing (cit. on p. 7).

(124) Ogle, K., Barber, J. J., Willson, C., and Thompson, B. (2009). Hierarchical statistical modeling of xylem vulnerability to cavitation. *New Phytologist 182*, 541–554 (cit. on p. 26).

(125) Oparka, K., and Prior, D. (1992). Direct evidence for pressure-generated closure of plasmodesmata. *The Plant Journal 2*, 741–750 (cit. on p. 28).

(126) Parent, B., Hachez, C., Redondo, E., Simonneau, T., Chaumont, F., and Tardieu, F. (2009). Drought and abscisic acid effects on aquaporin content translate into changes in hydraulic conductivity and leaf growth rate: a trans-scale approach. *Plant Physiol. 149*, 2000–2012 (cit. on p. 69).

(127) Passioura, J. (2006). Increasing crop productivity when water is scarce—from breeding to field management. *Agricultural water management 80*, 176–196 (cit. on p. 18).

(128) Passot, S., Couvreur, V., Meunier, F., Draye, X., Javaux, M., Leitner, D., Pagès, L., Schnepf, A., Vanderborght, J., and Lobet, G. (2019). Connecting the dots between computational tools to analyse soil-root water relations. *J. Exp. Bot. 70*, 2345–2357 (cit. on pp. 6, 40, 41, 60, 69, 86, 93, 119, 153).

(129) Passot, S., Moreno-Ortega, B., Moukouanga, D., Balsera, C., Guyomarc'h, S., Lucas, M., Lobet, G., Laplaze, L., Muller, B., and Guédon, Y. (2018). A New Phenotyping Pipeline Reveals Three Types of Lateral Roots and a Random Branching Pattern in Two Cereals. *Plant Physiol. 177*, 896–910 (cit. on pp. 21, 32, 71, 75).

(130) Pesquet, E., Zhang, B., Gorzsás, A., Puhakainen, T., Serk, H., Escamez, S., Barbier, O., Gerber, L., Courtois-Moreau, C., Alatalo, E., et al. (2013). Non-cell-autonomous postmortem lignification of tracheary elements in Zinnia elegans. *The Plant Cell 25*, 1314–1328 (cit. on p. 28).

(131) Pierret, A., Doussan, C., and Pagès, L. (2006). Spatio-temporal variations in axial conductance of primary and first-order lateral roots of a maize crop as predicted by a model of the hydraulic architecture of root systems. *Plant and soil 282*, 117–126 (cit. on p. 21).

(132) Postma, J. A., Kuppe, C., Owen, M. R., Mellor, N., Griffiths, M., Bennett, M. J., Lynch, J. P., and Watt, M. (2017). OpenSimRoot: widening the scope and application of root architectural models. *New Phytol. 215*, 1274–1286 (cit. on pp. 21, 63, 69, 189).

(133) Pound, M. P., French, A. P., Wells, D. M., Bennett, M. J., and Pridmore, T. P. (2012). CellSeT: novel software to extract and analyze structured networks of plant cells from confocal images. *Plant Cell 24*, 1353–1361 (cit. on pp. 25, 41, 46, 59, 94, 182).

(134) Pradal, C., Dufour-Kowalski, S., Boudon, F., Fournier, C., and Godin, C. (2008). OpenAlea: a visual programming and component-based software platform for plant modelling. *Funct. Plant Biol. 35*, 751–760 (cit. on pp. 61, 185).

(135) R Core Team R: A Language and Environment for Statistical Computing.; R Foundation for Statistical Computing, Vienna, Austria, 2018 (cit. on pp. 47, 100, 127, 158).

(136) Radford, J., Vesk, M., and Overall, R. (1998). Callose deposition at plasmodesmata. *Protoplasma 201*, 30–37 (cit. on p. 27).

(137) Raza, A., Friedel, J., and Bodner, G. In *Agroecology and strategies for climate change*; Springer: 2012, pp 167–211 (cit. on p. 118).

(138) Rellán-Álvarez, R., Lobet, G., and Dinneny, J. R. (2016). Environmental Control of Root System Biology. *Annu. Rev. Plant Biol. 67*, 619–642 (cit. on pp. 6, 119, 153).

(139) Reynolds, F. Herbaceous Dicot Root: Mature Ranunculus. https://www.flickr.com/photos/146824358@N03/35613585260/in/album-72157682034849461/ (accessed Sept. 15, 2021) (cit. on p. 49).

(140) Rieger, M., and Litvin, P. (1999). Root system hydraulic conductivity in species with contrasting root anatomy. *J. Exp. Bot. 50*, 201–209 (cit. on pp. 6, 61, 63, 68, 119).

(141) Rodriguez Casal, A., and Pateiro-Lopez, B. (2010). Generalizing the convex hull of a sample: the R package alphahull. (cit. on p. 44).

(142) Ronco, P., Zennaro, F., Torresan, S., Critto, A., Santini, M., Trabucco, A., Zollo, A., Galluccio, G., and Marcomini, A. (2017). A risk assessment framework for irrigated agriculture under climate change. *Advances in Water Resources 110*, 562–578 (cit. on p. 118).

(143) Ruzin, S. E. et al., *Plant microtechnique and microscopy*; Oxford University Press New York: 1999; Vol. 198 (cit. on p. 71).

(144) Salih, A. A., Ali, I. A., Lux, A., Luxová, M., Cohen, Y., Sugimoto, Y., and Inanaga, S. (1999). Rooting, Water Uptake, and Xylem Structure Adaptation to Drought of Two Sorghum Cultivars. *Crop Sci. 39*, 168–173 (cit. on p. 62).

(145) Saltelli, A., Annoni, P., Azzini, I., Campolongo, F., Ratto, M., and Tarantola, S. (2010). Variance based sensitivity analysis of model output. Design and estimator for the total sensitivity index. *Computer physics communications 181*, 259–270 (cit. on pp. 98, 100, 118, 120, 158).

(146) Saltelli, A., Tarantola, S., and Chan, K.-S. (1999). A quantitative model-independent method for global sensitivity analysis of model output. *Technometrics 41*, 39–56 (cit. on p. 100).

(147) Sanderson, J. (1983). Water uptake by different regions of the barley root. Pathways of radial flow in relation to development of the endodermis. *Journal of Experimental Botany 34*, 240–253 (cit. on p. 28).

(148) Sanderson, J., Whitbread, F. C., and Clarkson, D. T. (1988). Persistent xylem cross-walls reduce the axial hydraulic conductivity in the apical 20 cm of barley seminal root axes: implications for the driving force for water movement. *Plant Cell Environ. 11*, 247–256 (cit. on pp. 68, 86, 187).

(149) Schaap, M. G., Leij, F. J., and Van Genuchten, M. T. (2001). Rosetta: A computer program for estimating soil hydraulic parameters with hierarchical pedotransfer functions. *Journal of hydrology 251*, 163–176 (cit. on p. 156).

(150) Schneider, C. A., Rasband, W. S., and Eliceiri, K. W. (2012). NIH Image to ImageJ: 25 years of image analysis. *Nat. Methods 9*, 671–675 (cit. on pp. 48, 71).

(151) Schneider, H. M., Strock, C. F., Hanlon, M. T., Vanhees, D. J., Perkins, A. C., Ajmera, I. B., Sidhu, J. S., Mooney, S. J., Brown, K. M., and Lynch, J. P. (2021). Multiseriate cortical sclerenchyma enhance root penetration in compacted soils. *Proceedings of the National Academy of Sciences 118* (cit. on pp. 173, 183).

(152) Schneider, H. M., Wojciechowski, T., Postma, J. A., Brown, K. M., Lücke, A., Zeisler, V., Schreiber, L., and Lynch, J. P. (2017). Root cortical senescence decreases root respiration, nutrient content and radial water and nutrient transport in barley. *Plant Cell Environ. 40*, 1392–1408 (cit. on pp. 25, 40, 141).

(153) Schnepf, A., Leitner, D., Landl, M., Lobet, G., Mai, T. H., Morandage, S., Sheng, C., Zörner, M., Vanderborght, J., and Vereecken, H. (2018). CRootBox: a structural–functional modelling framework for root systems. *Ann. Bot.* (Cit. on p. 63).

(154) Schreiber, L., Franke, R., Hartmann, K.-D., Ranathunge, K., and Steudle, E. (2005). The chemical composition of suberin in apoplastic barriers affects radial hydraulic conductivity differently in the roots of rice (Oryza sativa L. cv. IR64) and corn (Zea mays L. cv. Helix). *J. Exp. Bot. 56*, 1427–1436 (cit. on p. 40).

(155) Schröder, T., Javaux, M., Vanderborght, J., Körfgen, B., and Vereecken, H. (2009). Implementation of a Microscopic Soil-Root Hydraulic Conductivity Drop Function in a Three-Dimensional Soil-Root Architecture Water Transfer Model. *Vadose Zone J. 8*, 783–792 (cit. on pp. 18, 20, 126).

(156) Schulz, A. (1995). Plasmodesmal widening accompanies the short-term increase in symplasmic phloem unloading in pea root tips under osmotic stress. *Protoplasma 188*, 22–37 (cit. on p. 28).

(157) Scott, M. F. et al. (2020). Multi-parent populations in crops: a toolbox integrating genomics and genetic mapping with breeding. *Heredity 125*, 396–416 (cit. on pp. 154, 155).

(158) Shane, M. W., M C Cully, M. E., and Canny, M. J. (2000). Architecture of Branch-root Junctions in Maize: Structure of the Connecting Xylem and the Porosity of Pit Membranes. *Ann. Bot. 85*, 613–624 (cit. on p. 86).

(159) Šimůnek, J., van Genuchten, M. T., and Šejna, M. (2008). Development and Applications of the HYDRUS and STANMOD sofware Packages and Related Codes. *Vadose Zone Journal 7* (cit. on pp. 16, 124, 156).

(160) Sinclair, T. R. (1994). Limits to crop yield? *Physiology and determination of crop yield*, 509–532 (cit. on p. 5).

(161) Sosa, J. M., Huber, D. E., Welk, B., and Fraser, H. L. (2014). Development and application of MIPAR^{TM}: a novel software package for two-and three-dimensional microstructural characterization. *Integrating Materials and Manufacturing Innovation 3*, 123–140 (cit. on p. 85).

(162) Sparks, A. H. (2018). nasapower: a NASA POWER global meteorology, surface solar energy and climatology data client for R. (cit. on pp. 127, 145, 156).

(163) Sterratt, D. C., Lyngholm, D., Willshaw, D. J., and Thompson, I. D. (2013). Standard anatomical and visual space for the mouse retina: computational reconstruction and transformation of flattened retinae with the Retistruct package. *PLoS Comput. Biol. 9*, e1002921 (cit. on p. 44).

(164) Steudle, E., Murrmann, M., and Peterson, C. A. (1993). Transport of Water and Solutes across Maize Roots Modified by Puncturing the Endodermis (Further Evidence for the Composite Transport Model of the Root). *Plant Physiol. 103*, 335–349 (cit. on pp. 45, 92).

(165) Steudle, E. (2001). The cohesion-tension mechanism and the acquisition of water by plant roots. *Annu. Rev. Plant Physiol. Plant Mol. Biol. 52*, 847–875 (cit. on pp. 5, 17).

(166) Steudle, E. (2000). Water uptake by plant roots: an integration of views. *Plant Soil 226*, 45–56 (cit. on pp. 6, 18, 68, 92).

(167) Steudle, E., and Peterson, C. A. (1998). How does water get through roots? *J. Exp. Bot. 49*, 775–788 (cit. on pp. 24, 28).

(168) Strock, C. F., Schneider, H. M., Galindo-Castañeda, T., Hall, B. T., Van Gansbeke, B., Mather, D. E., Roth, M. G., Chilvers, M. I., Guo, X., Brown, K., et al. (2019). Laser ablation tomography for visualization of root colonization by edaphic organisms. *Journal of Experimental Botany 70*, 5327–5342 (cit. on p. 85).

(169) Struik, P., and Makonnen, T. (1992). Effects of timing, intensity and duration of pollination on kernel set and yield in maize (Zea mays L.) under temperate conditions. *Netherlands Journal of Agricultural Science (Netherlands)* (cit. on p. 32).

(170) Sulis, M., Couvreur, V., Keune, J., Cai, G., Trebs, I., Junk, J., Shrestha, P., Simmer, C., Kollet, S. J., Vereecken, H., et al. (2019). Incorporating a root water uptake model based on the hydraulic architecture approach in terrestrial systems simulations. *Agricultural and forest meteorology 269*, 28–45 (cit. on p. 86).

(171) Tai, H., Lu, X., Opitz, N., Marcon, C., Paschold, A., Lithio, A., Nettleton, D., and Hochholdinger, F. (2016). Transcriptomic and anatomical complexity of primary, seminal, and crown roots highlight root type-specific functional diversity in maize (Zea mays L.) *Journal of Experimental Botany 67*, 1123–1135 (cit. on pp. 25, 40).

(172) Tamang, B. G., and Sadok, W. (2018). Nightly business: links between daytime canopy conductance, nocturnal transpiration and its circadian control illuminate physiological trade-offs in maize. *Environmental and Experimental Botany 148*, 192–202 (cit. on p. 127).

(173) Tarantola, S., Gatelli, D., Kucherenko, S., Mauntz, W., et al. (2007). Estimating the approximation error when fixing unessential factors in global sensitivity analysis. *Reliability engineering & system safety 92*, 957–960 (cit. on pp. 98, 100, 120).

(174) Tardieu, F. (1993). Will increases in our understanding of soil-root relations and root signalling substantially alter water flux models? *Philosophical Transactions of the Royal Society of London. Series B: Biological Sciences 341*, 57–66 (cit. on p. 19).

(175) Tardieu, F. (2012). Any trait or trait-related allele can confer drought tolerance: just design the right drought scenario. *J. Exp. Bot. 63*, 25–31 (cit. on pp. 30, 152).

(176) Tardieu, F., Draye, X., and Javaux, M. (2017). Root Water Uptake and Ideotypes of the Root System: Whole-Plant Controls Matter. *Vadose Zone J. 16* (cit. on pp. 19, 30, 152, 153).

(177) Tardieu, F., and Simonneau, T. (1998). Variability among species of stomatal control under fluctuating soil water status and evaporative demand: modelling isohydric and anisohydric behaviours. *Journal of experimental botany*, 419–432 (cit. on p. 190).

(178) Tardieu, F., Simonneau, T., and Muller, B. (2018). The Physiological Basis of Drought Tolerance in Crop Plants: A Scenario-Dependent Probabilistic Approach. *Annu. Rev. Plant Biol. 69*, 733–759 (cit. on pp. 5, 40, 68).

(179) Trachsel, S., Kaeppler, S. M., Brown, K. M., and Lynch, J. P. (2011). Shovelomics: high throughput phenotyping of maize (Zea mays L.) root architecture in the field. *Plant and soil 341*, 75–87 (cit. on pp. 5, 119).

(180) Turner, R. (2019). Package 'deldir'. (cit. on pp. 42, 44).

(181) Tyerman, S., Niemietz, C., and Bramley, H. (2002). Plant aquaporins: multifunctional water and solute channels with expanding roles. *Plant, cell & environment 25*, 173–194 (cit. on p. 27).

(182) Tylová, E., Pecková, E., Blascheová, Z., and Soukup, A. (2017). Casparian bands and suberin lamellae in exodermis of lateral roots: an important trait of roots system response to abiotic stress factors. *Ann. Bot. 120*, 71–85 (cit. on p. 85).

(183) Tyree, M. T., Yang, S., Cruiziat, P., and Sinclair, B. (1994). Novel Methods of Measuring Hydraulic Conductivity of Tree Root Systems and Interpretation Using AMAIZED (A Maize-Root Dynamic Model for Water and Solute Transport). *Plant Physiol. 104*, 189–199 (cit. on pp. 18, 69).

(184) Tyree, M. T. (1997). The cohesion-tension theory of sap ascent: current controversies. *Journal of Experimental Botany 48*, 1753–1765 (cit. on p. 17).

(185) Tyree, M. T., and Sperry, J. S. (1988). Do woody plants operate near the point of catastrophic xylem dysfunction caused by dynamic water stress? Answers from a model. *Plant physiology 88*, 574–580 (cit. on p. 26).

(186) Van Genuchten, M. T. (1980). A closed-form equation for predicting the hydraulic conductivity of unsaturated soils. *Soil science society of America journal 44*, 892–898 (cit. on pp. 16, 126, 146).

(187) van Lier, Q. d. J., Metselaar, K., and van Dam, J. C. (2006). Root Water Extraction and Limiting Soil Hydraulic Conditions Estimated by Numerical Simulation. *Vadose Zone J. 5*, 1264–1277 (cit. on pp. 126, 146).

(188) Vejchasarn, P., Lynch, J. P., and Brown, K. M. (2016). Genetic Variability in Phosphorus Responses of Rice Root Phenotypes. *Rice 9*, 29 (cit. on p. 40).

(189) Vetterlein, D., and Doussan, C. (2016). Root age distribution: how does it matter in plant processes? A focus on water uptake. *Plant Soil 407*, 145–160 (cit. on pp. 25, 40).

(190) Villalobos-González, L., Muñoz-Araya, M., Franck, N., and Pastenes, C. (2019). Controversies in midday water potential regulation and stomatal behavior might result from the environment, genotype, and/or rootstock: evidence from Carménère and Syrah grapevine varieties. *Frontiers in plant science 10*, 1522 (cit. on p. 19).

(191) Wahl, S., and Ryser, P. (2000). Root tissue structure is linked to ecological strategies of grasses: RESEARCH Interspecific variation in root tissue structure. *New Phytol. 148*, 459–471 (cit. on pp. 40, 51, 64, 96, 100).

(192) Wang, P., Calvo-Polanco, M., Reyt, G., Barberon, M., Champeyroux, C., Santoni, V., Maurel, C., Franke, R. B., Ljung, K., Novak, O., et al. (2019). Surveillance of cell wall diffusion barrier integrity modulates water and solute transport in plants. *Scientific reports 9*, 1–11 (cit. on p. 94).

(193) Wason, J., Bouda, M., Lee, E. F., McElrone, A. J., Phillips, R. J., Shackel, K. A., Matthews, M. A., and Brodersen, C. (2021). Xylem network connectivity and embolism spread in grapevine (Vitis vinifera L.) *Plant Physiology 186*, 373–387 (cit. on pp. 20, 21, 28).

(194) Wickham, H., and Chang, W. (2019). devtools: Tools to Make Developing R Packages Easier; 2016. *URL https://CRAN. R-project. org/package= devtools. R package version 1*, 381 (cit. on pp. 44, 76).

(195) Yamauchi, T., Pedersen, O., Nakazono, M., and Tsutsumi, N. (2021). Key root traits of Poaceae for adaptation to soil water gradients. *New Phytologist 229*, 3133–3140 (cit. on p. 25).

(196) Yang, J. T., Schneider, H. M., Brown, K. M., and Lynch, J. P. (2019). Genotypic variation and nitrogen stress effects on root anatomy in maize are node specific. *J. Exp. Bot. 70*, 5311–5325 (cit. on pp. 32, 73, 77, 96, 100, 124).

(197) York, L. M., and Lynch, J. P. (2015). Intensive field phenotyping of maize (Zea mays L.) root crowns identifies phenes and phene integration associated with plant growth and nitrogen acquisition. *J. Exp. Bot. 66*, 5493–5505 (cit. on p. 62).

(198) Zarebanadkouki, M., Meunier, F., Couvreur, V., Cesar, J., Javaux, M., and Carminati, A. (2016). Estimation of the hydraulic conductivities of lupine roots by inverse modelling of high-resolution measurements of root water uptake. *Ann. Bot.* (Cit. on pp. 69, 85).

(199) Zhang, X.-Y., Trame, M. N., Lesko, L. J., and Schmidt, S. (2015). Sobol sensitivity analysis: a tool to guide the development and evaluation of systems pharmacology models. *CPT: pharmacometrics & systems pharmacology 4*, 69–79 (cit. on p. 108).

(200) Zhou, X.-R., Schnepf, A., Vanderborght, J., Leitner, D., Lacointe, A., Vereecken, H., and Lobet, G. (2020). CPlantBox, a whole-plant modelling framework for the simulation of water- and carbon-related processes. *in silico Plants 2* (cit. on pp. 122, 188).

(201) Zhu, G. L., and Steudle, E. (1991). Water Transport across Maize Roots : Simultaneous Measurement of Flows at the Cell and Root Level by Double Pressure Probe Technique. *Plant Physiol. 95*, 305–315 (cit. on pp. 46, 74, 97).

(202) Zwieniecki, M. A., Thompson, M. V., and Holbrook, N. M. (2002). Understanding the hydraulics of porous pipes: tradeoffs between water uptake and root length utilization. *J. Plant Growth Regul. 21*, 315–323 (cit. on p. 69).

(203) Žydelis, R., Weihermüller, L., and Herbst, M. (2021). Future climate change will accelerate maize phenological development and increase yield in the Nemoral climate. *Science of The Total Environment 784*, 147175 (cit. on p. 32).